

# Master Thesis



## Statistical Analysis of Atmospheric Models for the Performance of Re-entry Trajectory Simulations at Mars

Statistische Untersuchung von Atmosphärenmodellen zur Anwendung in  
der Simulation von Wiedereintrittsvorgängen auf dem Mars

Submitted by

**Steffen Callsen**

Matriculation Number: 3171029

Master Program: M.Sc. Space Engineering I

First Examiner: Dr. Marco Scharringhausen

Second Examiner: Dr. Jens Grosse

Date of Issue: 11.02.2020

Date of Submission: 15.06.2020

## I. Abstract

Spacecraft entering the atmosphere of Mars encounter a variety of uncertainties on their flight from the entry interface until touchdown. This is why a precise landing point determination is not possible. Instead, statistical methods are applied to narrow the landing area down with a high confidence in an ellipse. Confidence ellipses contain all known uncertainties in order to resemble real life as close as possible. This work aims to isolate the uncertainty impact of the atmosphere on the trajectory and further analyze atmospheric conditions having an influence on the landing position.

Simulating the entry trajectory of the Phoenix spacecraft based on a six-state computation, the uncertainties given in two atmospheric models used in this work – MarsGRAM and MCD – are identified. The baseline statistical technique is the robust Monte Carlo method which biggest disadvantage is the requirement of computing power because it simulates  $N$  trajectories (here: 1000) and cannot utilize efficiency gains. In contrast, linear covariance analysis is challenged to provide similar results with considerably less computing power because it uses a single trajectory based on a nominal flight path. The results show that linear covariance analysis is able to provide satisfactory results all the way until touchdown. In fact, until parachute deployment the resemblance can be classified as excellent.

The influence of the atmosphere and its models on the trajectory is shown in various aspects. Seasonal influences are very pronounced in the northern hemisphere, but even more in the southern hemisphere because of the planetary properties which lead to different length and intensities of the seasons in the northern and southern part of the planet. In general, summer leads to higher densities because of sublimation of carbon dioxide from the pole while in winter carbon dioxide condensates at the pole. A comparison of the model results for the same input parameters show that they have considerable differences in their uncertainties as the size of the confidence ellipses vary significantly.

Furthermore, the impact of geometry and mass is shown by modifying the spacecraft to the Mars Science Laboratory in a case study. Due to its higher mass, it requires a deeper dive into the atmosphere to build up sufficient drag and therefore lands further downwind.

## II. Eidesstattliche Erklärung

Hiermit versichere ich, dass ich die vorliegende Arbeit selbstständig verfasst und keine anderen als die angegebenen Quellen und Hilfsmittel benutzt habe. Die Stellen, die anderen Werken dem Wortlaut oder dem Sinn nach entnommen worden, sind durch Angaben der Herkunft kenntlich gemacht.

Diese Erklärung erstreckt sich auch auf in der Arbeit enthaltene Grafiken, Skizzen, bildliche Darstellungen sowie auf Quellen aus dem Internet. Die Arbeit habe ich in gleicher oder ähnlicher Form auch auszugsweise noch nicht als Bestandteil einer Prüfungs- oder Studienleistung vorgelegt.

Ich versichere, dass die eingereichte elektronische Version der Arbeit vollständig mit der Druckversion übereinstimmt. Ich bin mit der Veröffentlichung der Arbeit einverstanden.

Bremen, den 15.06.2020

---

Steffen Callsen, 3171029

### III. Table of contents

I.	Abstract .....	II
II.	Eidesstattliche Erklärung .....	III
IV.	List of figures .....	VI
V.	List of tables .....	IX
VI.	List of abbreviations and acronyms .....	X
VII.	List of symbols .....	XI
VIII.	List of indices .....	XIII
IX.	List of natural constants.....	XIV
1	Introduction .....	1
1.1	Motivation .....	2
1.2	Scope of work.....	3
2	Mars atmosphere and models .....	4
2.1	Atmospheric properties .....	4
2.2	Atmospheric models.....	9
3	Theory of atmospheric re-entry .....	13
3.1	Re-entry.....	15
3.2	Descent .....	17
3.3	Landing.....	20
4	Simulink model.....	21
4.1	Equations of motion and integration.....	22
4.2	Feedback calculations .....	23
4.3	Parachute trigger .....	24
4.4	Lander separation and trigger .....	25
4.5	Interpolation parameters.....	25
4.6	(Static) input parameters.....	28
4.7	Thrust controller.....	30
4.8	Stop condition.....	31
4.9	Validation.....	31



---

5	Stochastic methods.....	36
5.1	Introduction to stochastics.....	36
5.2	Monte Carlo method.....	39
5.3	Linear Covariance Analysis.....	40
6	Monte Carlo analysis.....	47
6.1	MarsGRAM.....	47
6.2	MCD.....	51
7	Comparison of LCA and MC.....	53
7.1	MarsGRAM without vertical perturbations.....	53
7.2	MarsGRAM with vertical perturbations.....	58
7.3	MCD.....	60
7.4	Components of the LCA.....	62
7.5	Choice of integration method.....	66
8	Analysis of atmospheric models.....	69
8.1	Modelling year.....	69
8.2	Seasonal influence.....	71
8.3	Landing on the southern hemisphere.....	76
8.4	Case study: Mars Science Laboratory.....	78
9	Evaluation.....	81
10	Conclusion.....	83
11	Bibliography.....	85
12	Appendices.....	89
12.1	Generation of atmospheric model point/grid data.....	89
12.2	Detailed interpolation calculation.....	94
12.3	LCA Partial derivative matrix $F_x$ .....	98

## IV. List of figures

figure 1-1: Phoenix confidence ellipse with initial target and actual landing position .....	1
figure 1-2: Vertical profile of MarsGRAM and MCD data at the Phoenix landing site.....	2
figure 2-1: Mars Climate Database (MCD) density profile at Phoenix landing.....	5
figure 2-2: MCD density profile $\frac{1}{2}$ Mars year after the Phoenix landing .....	5
figure 2-3: Vertical temperature profile of the atmosphere from spacecraft measurements.	6
figure 2-4: General wind circulation on Mars.....	7
figure 2-5: MCD eastward winds at the Phoenix landing.....	8
figure 2-6: MCD eastward winds $\frac{1}{2}$ Mars year after the Phoenix landing .....	8
figure 2-7: Change of Mars' appearance during a global dust storm.....	9
figure 2-8: Mars MOLA map.....	10
figure 2-9: Example of a data grid.....	11
figure 2-10: Mars MOLA map with data grid space.....	11
figure 3-1: Spherical coordinate system for six-state simulation .....	14
figure 3-2: Computed comparison of different inertial flight-path angles for Mars descent of the Phoenix spacecraft .....	15
figure 3-3: Phoenix entry capsule geometry .....	16
figure 3-4: Drag and lift coefficient in relation to the Mach number .....	16
figure 3-5: Disk-gap band parachute basic design layout .....	18
figure 3-6: DGB-parachute drag coefficient in relation to the Mach number .....	18
figure 4-1: Block diagram of the simulation with different subsystems.....	21
figure 4-2: Processed drag coefficient data.....	26
figure 4-3: Data grid box .....	27
figure 4-4: Tri-linear interpolation procedure of a data grid box.....	28
figure 4-5: Mass-time relation .....	29
figure 4-6: Thrust-time relation during the landing phase of the spacecraft .....	30
figure 4-7: Longitude-latitude comparison of Phoenix data with MarsGRAM and MCD.	32

figure 4-8: Velocity-altitude comparison of Phoenix data with MarsGRAM and MCD....	33
figure 4-9: Time-velocity comparison of Phoenix data with MarsGRAM and MCD .....	34
figure 4-10: Time-acceleration comparison of Phoenix data with MarsGRAM and MCD	34
figure 4-11: Density-altitude comparison of Phoenix data with MarsGRAM and MCD...	35
figure 5-1: Standard normal distribution .....	37
figure 5-2: 1, 2 and 3-sigma confidence ellipses (black) and their eigenvectors .....	39
figure 6-1: Monte Carlo analysis MarsGRAM without vertical perturbations.....	49
figure 6-2: Monte Carlo analysis MarsGRAM with vertical perturbations.....	50
figure 6-3: Landing points of 1000 Monte Carlo runs of the Phoenix spacecraft using MarsGRAM .....	51
figure 6-4: Monte Carlo analysis MCD without vertical perturbations .....	52
figure 7-1: MarsGRAM without vertical perturbations LCA results superimposed with Monte Carlo runs .....	54
figure 7-2: Surface landing points of LCA and MC.....	56
figure 7-3: Points on the trajectory of LCA and MC at parachute deployment (215 seconds) .....	57
figure 7-4: Points on the trajectory of LCA and MC at lander separation (388 seconds).	57
figure 7-5: MarsGRAM with vertical perturbations LCA results superimposed with Monte Carlo runs.....	58
figure 7-6: Surface landing points of MarsGRAM LCA and MC with vertical perturbations .....	59
figure 7-7: Points on the trajectory of MarsGRAM LCA and MC with vertical perturbations at 215 seconds .....	60
figure 7-8: MCD without vertical perturbations LCA results superimposed with Monte Carlo runs.....	61
figure 7-9: Surface landing points of MCD LCA and MC without vertical perturbations	62
figure 7-10: LCA components MarsGRAM with vertical wind perturbations .....	63
figure 7-11: LCA components MarsGRAM without vertical wind perturbations .....	64
figure 7-12: LCA components MCD without vertical wind perturbations.....	65

figure 7-13: Comparison of ODE solvers for MarsGRAM Phoenix landing without vertical perturbations .....	67
figure 7-14: Comparison of ODE solvers for MCD Phoenix landing without vertical perturbations .....	68
figure 8-1: Surface landing points and 3-sigma landing ellipses of different MarsGRAM modelling years .....	70
figure 8-2: Surface landing points and 3-sigma landing ellipses of different MCD modelling years .....	71
figure 8-3: Surface landing points and 3-sigma ellipses of different dates for a year on Mars with MarsGRAM .....	72
figure 8-4: Surface landing points and 3-sigma ellipses of different dates for a year on Mars with MCD .....	73
figure 8-5: Comparison of surface landing points and ellipses for nominal Phoenix landing using the MarsGRAM and MCD databases .....	74
figure 8-6: Comparison of surface landing points and ellipses for the Phoenix landing + $\frac{1}{4}$ year using the MarsGRAM and MCD databases .....	74
figure 8-7: Comparison of surface landing points and ellipses for the Phoenix landing + $\frac{1}{2}$ year using the MarsGRAM and MCD databases .....	75
figure 8-8: Comparison of surface landing points and ellipses for the Phoenix landing + $\frac{3}{4}$ year using the MarsGRAM and MCD databases .....	75
figure 8-9: Comparison of surface landing points and ellipses for the Phoenix landing + 1 year using the MarsGRAM and MCD databases .....	76
figure 8-10: Velocity-altitude comparison of nominal Phoenix landing and mirrored on the southern hemisphere .....	77
figure 8-11: Surface landing points and 3-sigma ellipses of different dates for a year on Mars with MarsGRAM on the southern hemisphere .....	78
figure 8-12: Comparison of Monte Carlo surface landing points and ellipses for the Phoenix and the MSL landing .....	80
figure 8-13: Various diagrams comparing Phoenix landing to MSL landing .....	80
figure 12-1: Interpolation box example 1 .....	97
figure 12-2: Interpolation box example 2 .....	97

## V. List of tables

table 3-1: Explanation of spacecraft states .....	14
table 4-1: Initial conditions at entry.....	31
table 8-1: Adjusted MSL properties in comparison to Phoenix .....	79
table 12-1: MarsGRAM parameter handles .....	90

## VI. List of abbreviations and acronyms

Abbreviation/ Acronym	Meaning
AGL	Above Ground Level
AMR	Above MOLA Radius
AoA	Angle of Attack
CNES	Centre National d'Etudes Spatiales
DGB	Disk-Gap-Band
EDL	Entry, Descent and Landing
EoM	Equations of Motion
ESA	European Space Agency
FPA	Flight-Path Angle
LCA	Linear Covariance Analysis
LS	Solar longitude
MarsGRAM	Mars Global Reference Atmospheric Model
MC	Monte Carlo
MCD	Mars Climate Database
MGS	Mars Global Surveyor
MOLA	Mars Orbiter Laser Altimeter
MSL	Mars Science Laboratory
NaN	Not a Number
NASA	National Aeronautics and Space Administration
ODE	Ordinary Differential Equation
PI	Proportional-Integral
RK4	Fourth order Runge-Kutta
VAA	Velocity Azimuth Angle

## VII. List of symbols

Symbol	Meaning	Unit
$\alpha$	Angle of attack	rad or deg
$\beta$	Thrust angle	rad or deg
$\gamma$	Flight path angle	rad or deg
$\delta$	Deviations/Dispersions	-
$\theta$	Longitude	rad or deg
$\kappa$	Ratio of specific heats	-
$\rho$	Density	kg/m <sup>3</sup>
$\sigma$	Bank angle	rad or deg
$\sigma(X)$	Standard deviation	-
$\varphi$	Latitude	rad or deg
$\chi$	Chi-Square probability	-
$\Psi$	Velocity azimuth angle	rad or deg
$\omega$	Vector of zero-mean white-noise process	-
$\Omega$	Probability Space	-
$0$	Matrix of zeros	-
$a$	Semi-major axis	-
$A$	Reference area	m <sup>2</sup>
$b$	Semi-minor axis	-
$c$	Speed of sound	m/s
$c_p$	Specific heat capacity at constant pressure	J/(kg*K)
$c_v$	Specific heat capacity at constant volume	J/(kg*K)
$C$	Coefficient	-
$C(X)$	Covariance matrix	-
$\text{Cov}(X,Y)$	Covariance	-
$D$	Dispersion matrix	-

$E(X)$	Expected value	-
$F_x$	Partial derivative matrix	-
$g$	Acceleration due to gravity	$m/s^2$
$h$	Step size	s
$h$	Altitude	m
$I$	Identity matrix	-
$I_{SP}$	Specific impulse	s
$k$	RK4 points	-
$m$	Mass	kg
$M$	Molar mass	kg/mole
$Ma$	Mach number	-
$p$	Uncertainty parameter	-
$P(X)$	Probability	-
$P_{x,0}$	Covariance matrix of the initial true state	-
$r$	Radius	m
$S$	Variance vector	-
$t$	Time	s
$T$	Temperature	K
$T$	Thrust	N
$\hat{u}$	Command vector	-
$v$	Velocity	$m/s$
$V(X)$	Variance	-
$x$	True state vector	-
$\bar{x}$	Nominal state vector	-
$X$	Augmented state vector	-
$X, Y$	Random variable	-
$\tilde{y}$	Continuous inertial measurement	-



## VIII. List of indices

Index	Meaning
0	Initial condition
9x9	Simulation without vertical wind perturbations
10x10	Simulation with vertical wind perturbations
$\eta$	Inertial instrument measurement noise
$\rho$	Density
areoid	In reference to the areoid
D	Drag
east	Eastwards direction
i	Inertial
L	Lift
n	Running index
north	Northwards direction
N	Nominal
P	Parachute
SC	Spacecraft
SD	Standard deviation
terrain	In reference to the surface terrain
vert	Vertical direction
w	Wind

## IX. List of natural constants

Constants	Symbol	Value and Unit
Standard acceleration of free fall on Earth	$g_0$	9.80665 m/s <sup>2</sup>
Standard gravitational parameter Mars	GM	4.282837522*10 <sup>13</sup> m <sup>3</sup> /s <sup>2</sup>
Universal gas constant	$R_0$	8.314452618 J/(mole*K)

# 1 Introduction

The start of the exploration and investigation of Mars' atmosphere can be dated back to the late eighteenth century, when William Herschel first published his observations in 'Philosophical Transactions of the Royal Society' [1]. However, it was not until the first spacecraft fly-by in 1965, which was part of the Mariner 4 mission, that the data provided the evidence for the theoretical approach of the atmosphere's constituents and pressure. Since then, the analysis and detailed specification of the atmosphere has been an ongoing endeavor. While measurements from space provide an approximate analysis of the atmosphere, the degree of detail is higher for lander missions which cross through all layers of the atmosphere - although, fewer than a dozen landers have successfully touched down on Mars' surface. Consequently, the data density for the atmosphere is still low, especially when compared to Earth where continuous weather observations provide detailed analyses of its properties.

Due to uncertainties in the re-entry, the landing point of a mission cannot be determined precisely. Instead, a confidence ellipse containing a high percentage of all possibilities is created (see figure 1-1). These confidence ellipses contain uncertainties of the atmosphere and other factors, for instance, aerodynamic properties, the configuration (e.g. angle of attack) or the initial entry conditions.

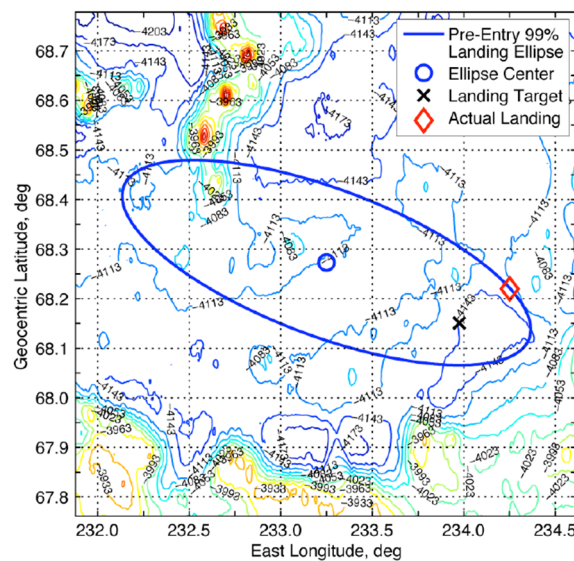


figure 1-1: Phoenix confidence ellipse with target and actual landing position. [2, p. 3]

## 1.1 Motivation

Given the few missions providing detailed data of the atmospheric composition, computer models are subject to uncertainty. The models MarsGRAM and MCD, which are the basis of this work, are described in chapter 2. As the atmospheric uncertainties alone are not specified separately in the confidence ellipses, this study will analyze the share of the atmosphere in the uncertainties. A first impression case study is carried out to investigate the approximate extent of disparities between the two models. The case study is performed as a vertical profile of the parameters density and wind (eastward, northward and vertical) at the Phoenix landing site and approximate entry time (23:30:00 UTC on 25<sup>th</sup> of May 2008; 68.219° N, 234.248° E [2]).

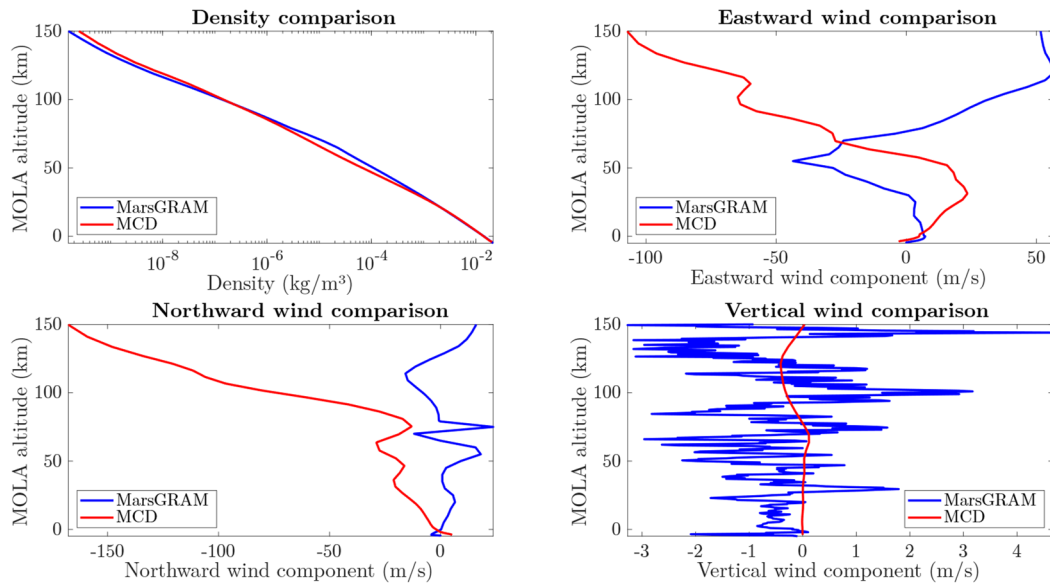


figure 1-2: Vertical profile of MarsGRAM and MCD data at the Phoenix landing site.

figure 1-2 shows that the output data of the atmospheric models are different. The density data are relatively identical in the lower forty kilometers but deviate higher up. Because of the logarithmic scale, even small deviations in the graph indicate significant differences. The vertical wind data of both models have approximately the same mean values, but MCD has a steady altitude profile while MarsGRAM has high local variances. Deviations in the horizontal winds indicate significant differences in the models – both in magnitude of wind speed and direction. As an outcome of this initial case study, it is expected that the simulation results between the models will have a high variability as well.

## 1.2 Scope of work

Uncertainties in the atmospheric models and the differences between them are analyzed by simulating an atmospheric re-entry. A simulation is created based on the Phoenix lander, which landed on Mars in 2008. It contains all necessary mathematical operations to compute the trajectory of the spacecraft from the entry point through parachute deployment until touchdown.

The atmospheric models are attached to the simulation and can be altered according to uncertainties in the parameters. In order to investigate the impact, Monte Carlo and linear covariance analyses are performed which result in parameter deviations and confidence ellipses of the landing points.

Furthermore, the atmospheric models themselves are investigated by analyzing internal modelling changes, like observation years or seasonal impact, given the orbit properties of the planet. Additionally, the Phoenix landing is mirrored to the southern hemisphere to investigate the respective influence on the landing position. In the end, the impact of the geometry and mass is inspected by changing the spacecraft to the larger Mars Science Laboratory.

## 2 Mars atmosphere and models

Spacecraft entering the atmosphere of Mars and Earth both utilize the atmosphere as their main decelerator. However, the properties of both planets' atmosphere vary widely, which leads to disparities in the performance of atmospheric entries. To address this issue, the following chapter contains a general description of Mars' atmosphere. Since the representation of the atmosphere in a simulation is achieved with numerical models, it will be followed by an outline of the respective atmospheric models.

### 2.1 Atmospheric properties

While the conditions on Mars vary as they do on Earth (depending on the season, time of day, weather etc.), the surface pressure on Mars is on average only about 0.6 percent (6.1 mbar) of Earth's standard pressure (1.01325 bar). Consequently, the density is also considerably lower than on Earth which leads to major differences in the way a re-entry is performed at Mars (see chapter 3). [3]

The rotation axis of Mars is tilted by about 25.2 degrees, which is similar to Earth, leading to high seasonal variations of the atmospheric properties. Due to the lack of a standardized calendar, these seasons are tracked with the solar longitude  $L_s$  which tracks the 360-degree movement around the sun (vernal equinox:  $L_s = 0^\circ$ , northern summer solstice:  $L_s = 90^\circ$ , northern winter solstice:  $L_s = 270^\circ$ ). Additionally, the orbit of Mars has an eccentricity which is about 5.5 times higher than the near-circular orbit of Earth. Coincidentally, aphelion and perihelion of Mars are close to the summer/winter solstices: Aphelion is at  $L_s = 70^\circ$  and perihelion is correspondingly at  $L_s = 250^\circ$ . This property of Mars' orbit leads to different lengths and intensities of the seasons. Summer in the northern hemisphere is fairly long but only warm due to the low velocity around aphelion (long time) and the increase in distance from the Sun (less heat) In contrast, summers in the southern hemisphere are shorter (higher velocity) but more intense (lower distance) while winters are cold and long. The mismatch in temperatures leads to density differences which can be seen in figure 2-1 and figure 2-2. [3] [4]

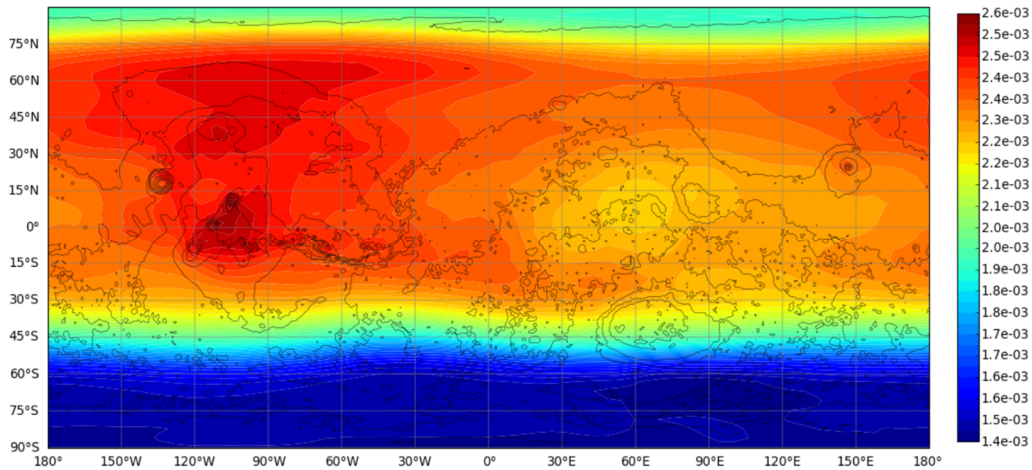


figure 2-1: Mars Climate Database (MCD) density profile at Phoenix landing ( $L_s = 76.6^\circ$ ), 20 km AMR (above MOLA radius). Temperate summer in the northern hemisphere,  $L_s$  between aphelion and northern summer solstice.

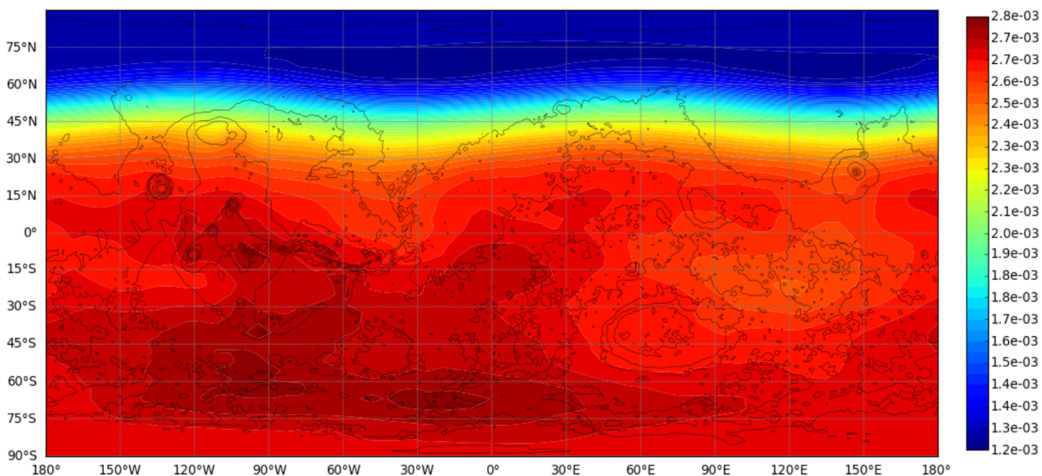


figure 2-2: MCD density profile  $\frac{1}{2}$  Mars year after the Phoenix landing ( $L_s = 258.9^\circ$ ), 20 km AMR. Hot summer in the southern hemisphere,  $L_s$  between perihelion and southern summer solstice.

Due to a higher distance to the Sun and the low-density atmosphere, the surface temperatures are lower than on Earth with a mean of about 200 K. Furthermore, the absence of surface water and the high orbit eccentricity lead to high temperature variations on a daily and seasonal level (150 – 300 K). [3]

The atmosphere on the surface is primarily composed of carbon dioxide ( $\approx 95.3$  percent), nitrogen ( $\approx 2.7$  percent) and Argon ( $\approx 1.6$  percent) followed by small amounts of oxygen, carbon monoxide and other trace gases. A small greenhouse effect is induced by the atmosphere which increases the temperatures slightly by about 5 K. In contrast, the greenhouse effect on Earth accounts for a

temperature increase of approximately 33 K. One particular effect observed at Mars is an anti-greenhouse effect during dust storms. Usually, dust particles only represent a small proportion of the atmosphere, but in the event of a dust storm they are picked up from the ground which leads to a significant increase of dust particles in the atmosphere. The dust particles absorb the incoming solar radiation and decrease the surface temperature by a few degrees Kelvin. [3]

In the altitudes of interest up to 150 kilometers, the atmosphere of Mars is distinguished into different layers due to the temperature profile and composition (see figure 2-3). The troposphere with minor weather activities like water-ice clouds extends up to 60 kilometers at which point it merges into the mesosphere. Due to the lack of ozone, Mars does not have a stratosphere. The temperatures in the mesosphere stay relatively constant after the near-steady reduction in the troposphere. Above 120 kilometers, the mesosphere changes into the thermosphere where the temperatures are rising again due to “absorption of radiation in the far and extreme ultra-violet ranges”. [3]

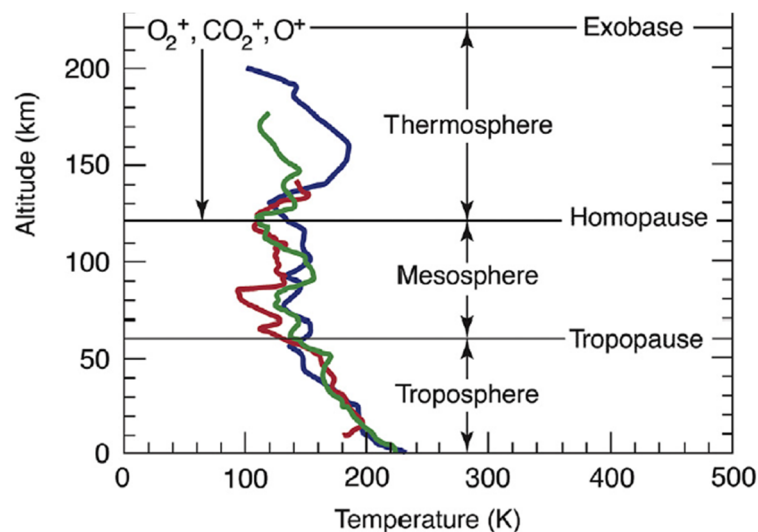


figure 2-3: Vertical temperature profile of the atmosphere from spacecraft measurements, adapted from [3, p. 169].

Blue: Viking 1. Green: Viking 2. Red: Pathfinder.

While the atmosphere of Mars only has one percent of Earth’s density, it still possesses complex wind systems (see figure 2-4) with substantial wind speeds. These systems have to be separated into different categories on where and when they form. As the data of these phenomena is very limited and solely based on successful



lander missions and measurements from space, these explanations merely describe the current state of scientific knowledge.

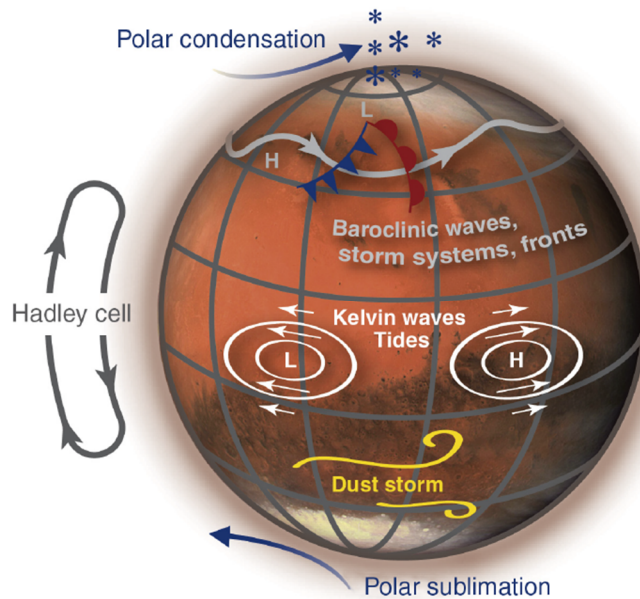


figure 2-4: General wind circulation on Mars. [3, p. 171]

### High latitudes

During winter at high latitudes, systems of high and low pressure were measured by the two Viking landers which resemble the same system patterns observed on Earth. In these areas, the surface wind speeds are averaging about 10-20 m/s with a predominant eastward direction (westerlies). In contrast, during summer the winds are primarily headed in a westwards direction (easterly). These effects can be viewed in figure 2-5 and figure 2-6. Vertical circulation of the air is predominantly apparent as a Ferrel circulation cell in high latitudes. Furthermore, there is a polar circulation cell at the poles. At very high latitudes, the effect of the poles has to be taken into account. Due to the high temperature differences between summer and winter, significant amounts of carbon dioxide condense at the poles during winter and sublime during summer. Therefore, an additional flow either to or away from the poles is present. The condensation and sublimation of carbon dioxide at the poles is one of the primary reasons for the considerable density differences between summer and winter. [3] [5]

## Tropics

In the tropics, easterly winds are dominant during the whole Mars year. Additionally, a phenomenon called Hadley circulation takes place in the lower and mid latitudes. Convection leads to the rise of air in the summer hemisphere and a sinking of air in the winter hemisphere. Consequently, a surface and high-altitude wind (in opposite directions) along the meridians is created. Furthermore, during the equinoxes, two separate cells to the north and the south are created which have a joint convergence zone in the tropics. [3]

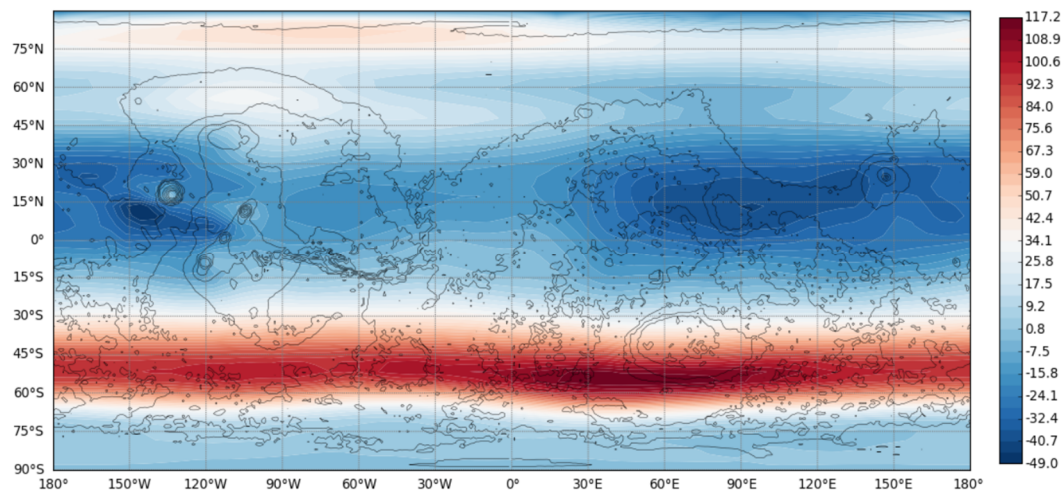


figure 2-5: MCD eastward winds at the Phoenix landing ( $L_s = 76.6^\circ$ ), 20 km AMR. High westerlies in the southern hemisphere, low easterlies in the northern hemisphere. Easterlies in the tropics.

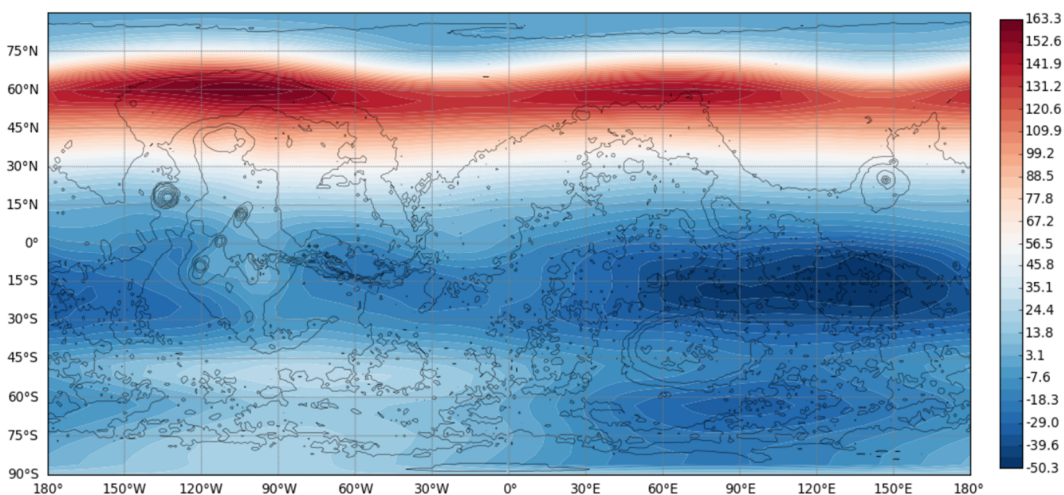


figure 2-6: MCD eastward winds  $\frac{1}{2}$  Mars year after the Phoenix landing ( $L_s = 258.9^\circ$ ), 20 km AMR. High westerlies in the northern hemisphere, low easterlies in the southern hemisphere. Easterlies in the tropics.

### Dust storms

Due to the low density, the winds are powerful enough to raise very fine dust from the surface and, given sufficient strength, create a dust storm. Dust storms occur on a local scale (dust devils) but can enlarge to a global scale (see figure 2-7). They tend to occur at a solar longitude of about 260 degrees which is just after perihelion. Measurements from the Viking 1 lander indicate that surface winds exceed 30 m/s during a dust storm event. [3] [4]

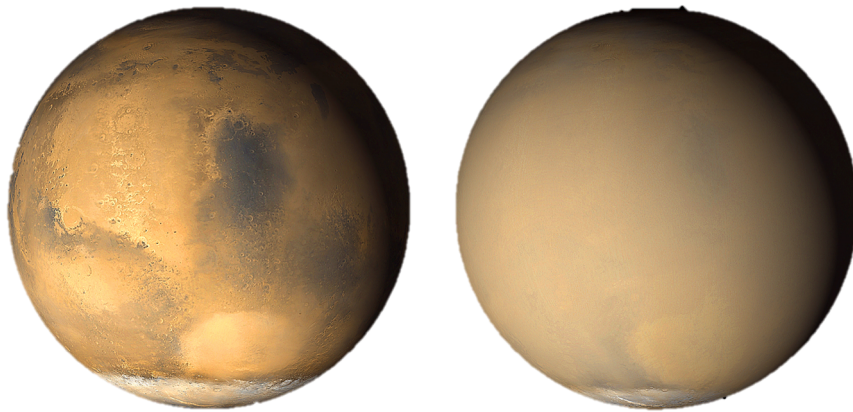


figure 2-7: Change of Mars' appearance during a global dust storm.  
Left: Late June 2001 with a local dust storm near the south pole.  
Right: July 2001 global dust storm. [6]

## 2.2 Atmospheric models

Atmospheric modelling of the atmosphere of Mars can be traced back to as early as 1969 when Leovy and Mintz converted the state-of-the-art general circulation model of Earth to Mars. While it was possible to forecast condensation of CO<sub>2</sub> in the atmosphere and mid-latitude weather systems on a large scale, it was relatively inaccurate when compared to today's numeric simulations. Over the past decades, a lot of effort has been put into improving the models and making them available to scientists around the world. Two atmospheric models are investigated in this study to analyze the differences proposed by them. Each of the models is developed/funded and used by one of the major Western space agencies – NASA (National Aeronautics and Space Administration) and ESA (European Space Agency). Both models utilize the MOLA (Mars Orbiter Laser Altimeter) areoid as their main altitude reference and can therefore be attached to the same simulation. [7]



The areoid is the geoid model of Mars and defines the reference zero-altitude around the planet for the altitude reference system MOLA. Altitude values are expressed in ‘above MOLA radius’ (AMR). As Mars does not have liquid oceans like Earth, the reference surface is not at sea level but instead a plane of equal potential. Due to this definition, a portion of the topography of Mars has negative MOLA altitudes (see figure 2-8). As an example, the Phoenix lander touched down at a MOLA altitude of approximately -4100 m [2]. [8]

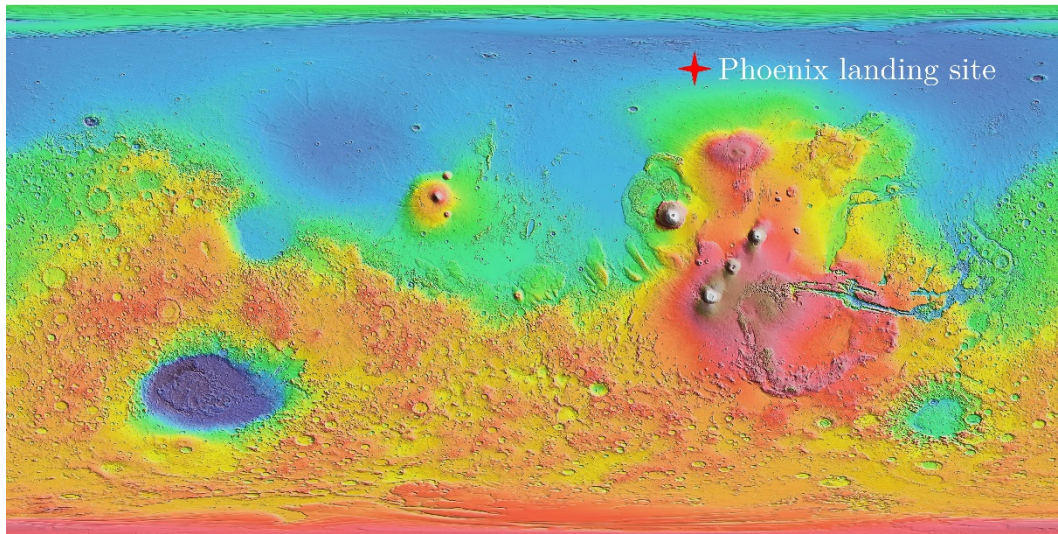


figure 2-8: Mars MOLA map, adapted from [9].

Blue and green indicate negative altitudes. Yellow indicates approximately zero altitude. Red, brown and white indicate positive altitudes.

### 2.2.1 Mars Global Reference Atmospheric Model 2010 (MarsGRAM)

MarsGRAM is developed by NASA’s Marshall Space Flight Center (Huntsville, Alabama) and is part of a series of models which also include Earth, Venus, Neptune and Titan. It is the primary NASA database for the calculation of atmospheric re-entry and aerobrake maneuvers. Apart from atmospheric properties like density, wind, temperature and their respective perturbations, it is also possible to generate topography data which is provided relative to the MOLA areoid. [10]

For each scenario, a grid of data is created (see figure 2-9). As the values tend to change more in the vertical direction than they do in the horizontal direction (e.g. density decreases exponentially), it is chosen to increase the data points in the altitude spectrum and decrease it in the longitudinal/latitudinal frame (increase the spacing).

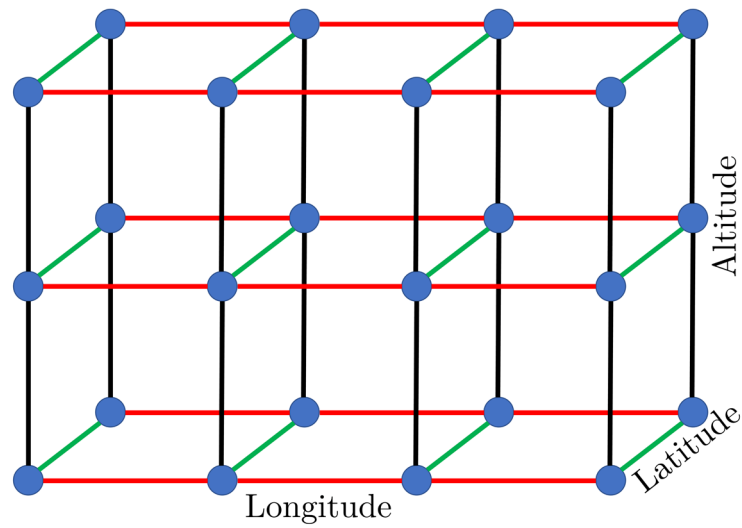


figure 2-9: Example of a data grid.

Blue points: Data. Red: Longitude. Green: Latitude. Black: Altitude.

MarsGRAM Phoenix landing example (see figure 2-10):

Longitude:  $190^{\circ} - 240^{\circ}$  with  $2^{\circ}$  spacing

Latitude:  $65^{\circ} - 73^{\circ}$  with  $2^{\circ}$  spacing

Altitude: -5 km to 143 km MOLA with 0.5 km spacing

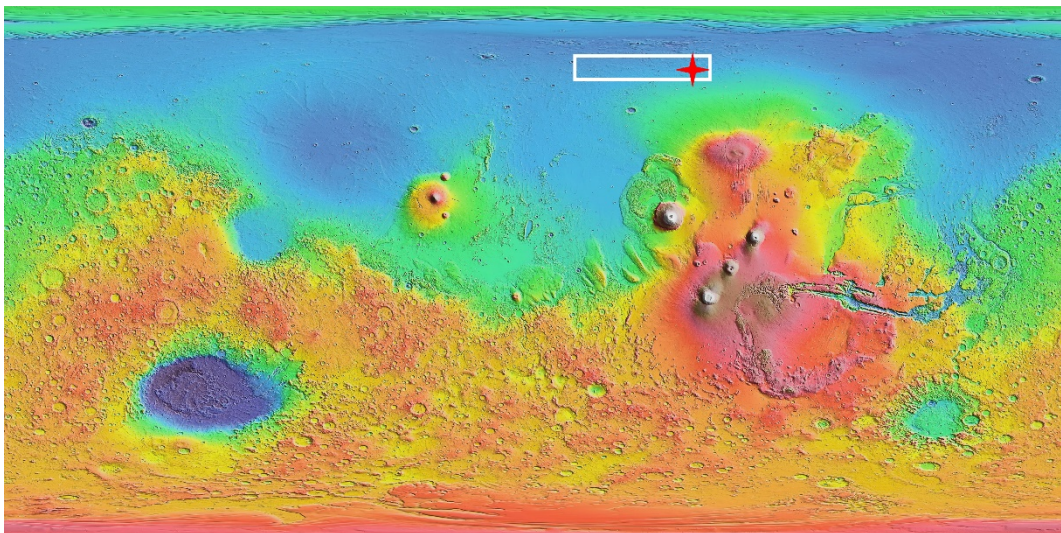


figure 2-10: Mars MOLA map with data grid space, adapted from [9].

Red cross indicates original Phoenix landing location.

MarsGRAM provides a comprehensive dataset with many different parameters. A guide on how to generate a dataset can be found in annex 12.1.1. The parameters required for the simulation are the following:

- Density and uncertainty thereof
- Temperature
- Molar mass
- Horizontal winds and uncertainty thereof
- Vertical winds and uncertainty thereof
- Areoid radius
- Altitude of local terrain above/below MOLA
- Local acceleration of gravity

### 2.2.2 Mars Climate Database v5.3 (MCD)

The Mars Climate Database is a European database primarily funded by ESA and CNES (Centre National d'Etudes Spatiales) and is developed by the following institutions [11]:

- Laboratoire de Météorologie (Paris, France)
- Department of Atmospheric, Oceanic and Planetary Physics (Oxford University, United Kingdom)
- Department of Physics and Astronomy (Open University, United Kingdom)
- Instituto de Astrofísica de Andalucía (Granada, Spain)

The access to the database is performed through the web interface [12] because a direct installation of the database on a Windows environment proved to be rather complex. Unfortunately, the web interface does not provide full access to the database as it is not capable of outputting the following data points:

- Vertical wind perturbations
- Areoid radius
- Altitude of local terrain above/below MOLA
- Local acceleration of gravity
- Molar mass

To achieve the same grid density as for MarsGRAM, annex 12.1.2 displays how to manually gather the data from the web interface of MCD.

### 3 Theory of atmospheric re-entry

Even though it appears to be a common occurrence nowadays, landing a spacecraft on another planet is still a technologically challenging task to achieve and a considerable number of missions fail. When approaching a planet with an atmosphere, the most critical phase of the flight starts once the upper part of the atmosphere is encountered and significant aerodynamic forces begin to act on the spacecraft. The mission phase between entry of the atmosphere and touchdown on the surface is called EDL – or Entry, Descent and Landing which will be described in the sections below and focus on a re-entry performed at Mars.

In general, the function of the EDL can be described as reducing the velocity of the spacecraft from entry velocity to (nearly) zero at the surface while assuring that the spacecraft survives the encountered conditions. To model the spacecraft movement as close to reality as possible, a six-state simulation is chosen – three states for position and three for velocity. This enables three-dimensional movement of a point mass within the given environment. In contrast, a three-state model solely simulates the movement in a 2D-plane. As the atmospheric influences like wind act in a 3D-environment, the three-state simulation is found to not be sufficient for this work.

As the spacecraft moves in relation to a planet, which is almost shaped like a sphere, a spherical coordinate system is used to simulate the dynamics of the system. In a spherical coordinate system, the six states are radius  $r$ , longitude  $\theta$ , latitude  $\varphi$ , velocity  $v$ , flight-path angle  $\gamma$  and velocity azimuth angle  $\psi$  and are further explained in table 3-1.

All position coordinates are given with respect to the center of the assumed spherical planet (planetocentric) as the atmospheric models provide data in this way. A graphic explanation of the coordinate system is shown in figure 3-1.

table 3-1: Explanation of spacecraft states

State	Explanation
Radius $r$	Distance from the planet's center to the point mass
Longitude $\theta$	Angle from the prime meridian to the line 'point mass – center of the planet'
Latitude $\phi$	Angle from the equator to the line 'point mass – center of the planet'
Velocity $v$	Magnitude of the velocity vector
Flight-path angle $\gamma$	Angle between the velocity vector and the local horizontal, negative towards the ground
Velocity azimuth angle $\psi$	Angle between the velocity vector and the local meridian, rotating eastwards

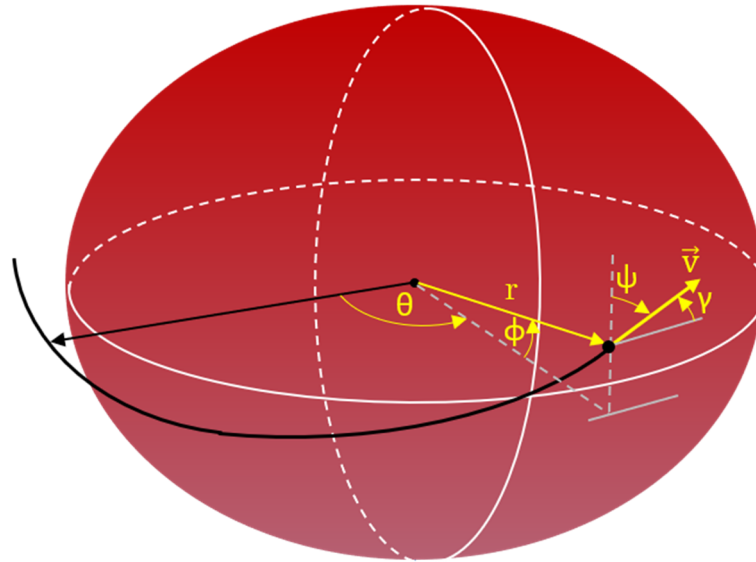


figure 3-1: Spherical coordinate system for six-state simulation, adapted from [13, p. 22].



### 3.1 Re-entry

During the re-entry phase, the spacecraft loses most of its speed by atmospheric drag. The spacecraft enters the atmosphere of Mars with a velocity of multiple kilometers per second. Historically, entry velocities ranged from about 4.7 to 7.3 km/s. These velocities create a substantial amount of drag once the atmosphere is sufficiently dense. Due to the significantly lower density in comparison with Earth, these conditions are met at lower altitudes. Consequently, to guarantee sufficient drag, the spacecraft has to dive deep into the atmosphere by entering it with a higher flight-path angle ( $\gamma \approx 11^\circ$ - $17^\circ$ ) than compared to entry-profiles on Earth ( $\gamma \approx 5^\circ$ - $7^\circ$ ). If the flight-path angle is too low, the spacecraft will ‘skip’ off the atmosphere (see figure 3-2) like a stone on the surface of a lake if thrown with the correct speed and flight-path angle. If the angle is too high, the deceleration and/or the thermal loads will exceed the spacecraft’s limits and destroy it. [14]

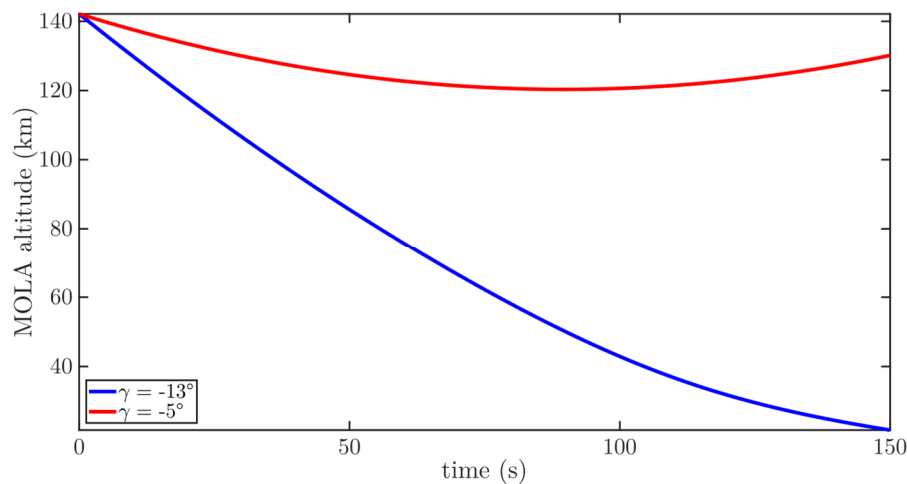


figure 3-2: Computed comparison of different inertial flight-path angles for Mars descent of the Phoenix spacecraft.

If the flight-path angle is too low, the spacecraft ‘skips’ off the atmosphere.

Blue:  $\gamma = -13^\circ$ . Red:  $\gamma = -5^\circ$ .

During re-entry, the atmospheric drag leads to substantial heating of the spacecraft which, if not protected, would lead to destruction. Therefore, a spacecraft has to be equipped with a thermal protection system that discards the thermal energy accordingly. The Phoenix spacecraft utilizes a 70-degree sphere-cone aeroshell (see figure 3-3) with a  $5.5155 \text{ m}^2$  [2] reference area which possesses good drag properties in the hypersonic regime and has been used on every Mars lander to date. [14]

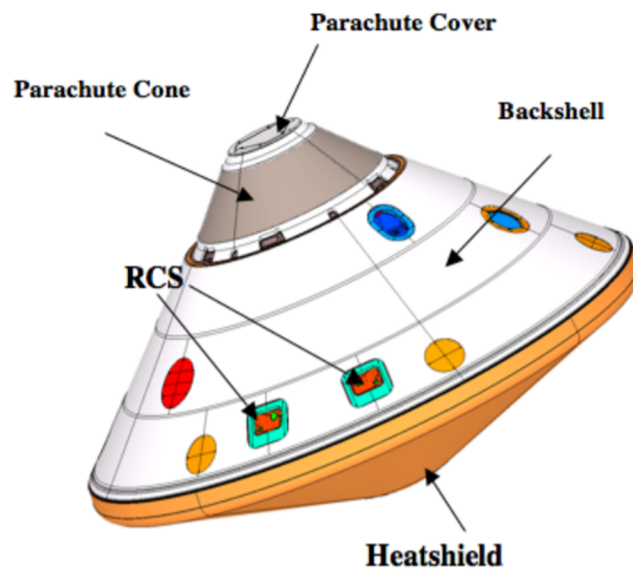


figure 3-3: Phoenix entry capsule geometry with heat shield, backshell and parachute cone plus cover. [15, p. 4]

The aerodynamic properties of the Phoenix spacecraft have been analyzed thoroughly in preparation for launch. The drag and lift coefficients ( $C_D$  and  $C_L$ ) depending on the angle of attack and the Mach number can be seen in figure 3-4.

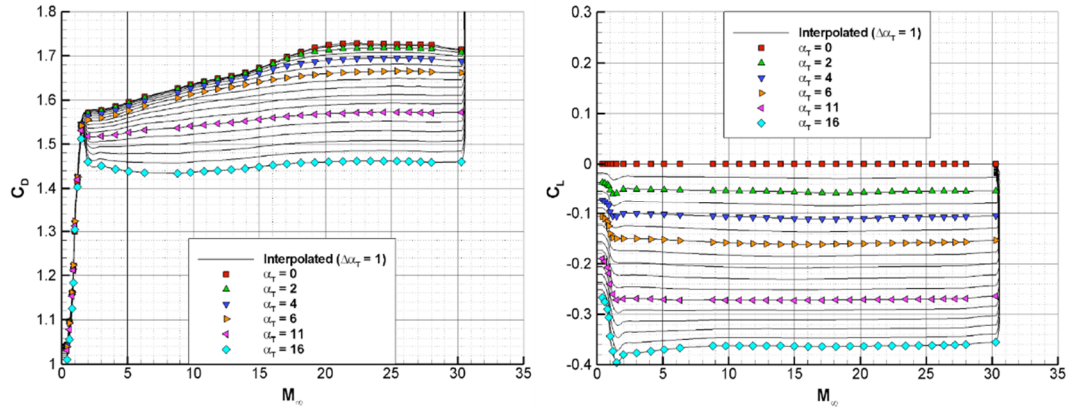


figure 3-4: Drag and lift coefficient in relation to the Mach number. [16, p. 11]  
Different graphs due to changing angle of attacks.

The motion of the spacecraft (SC) during re-entry is determined by six ordinary differential equations (ODE) according to the six-state simulation. For simplification, a stationary planetary atmosphere is assumed. The terms highlighted in bold show the appended parts to include wind within the simulation. Wind is included in the Up-East-North frame ( $v_{w,vert}$ ,  $v_{w,east}$  and  $v_{w,north}$ ) and is therefore attached to the ODEs of radius, longitude and latitude. [17]

$$\begin{aligned}
\dot{r} &= \dot{v} \cdot \sin(\gamma) + \mathbf{v}_{\mathbf{w},\text{vert}} \\
\dot{\theta} &= \frac{v \cdot \cos(\gamma) \cdot \sin(\psi) + \mathbf{v}_{\mathbf{w},\text{east}}}{r \cdot \cos(\phi)} \\
\dot{\phi} &= \frac{v \cdot \cos(\gamma) \cdot \sin(\psi) + \mathbf{v}_{\mathbf{w},\text{north}}}{r} \\
\dot{v} &= -\frac{\rho \cdot v^2 \cdot C_{D,SC} \cdot A_{SC}}{2 \cdot m} - g \cdot \sin(\gamma) \\
\dot{\gamma} &= \frac{\rho \cdot C_L \cdot v \cdot A_{SC} \cdot \cos(\sigma)}{2 \cdot m} - \cos(\gamma) \cdot \left( \frac{g}{v} - \frac{v}{r} \right) \\
\dot{\psi} &= \frac{\rho \cdot C_L \cdot v \cdot A_{SC} \cdot \sin(\sigma)}{2 \cdot m \cdot \cos(\gamma)} - \frac{v \cdot \cos(\gamma) \cdot \tan(\phi) \cdot \sin(\psi)}{r}
\end{aligned}$$

with: Density  $\rho$ , Reference area  $A$ , mass  $m$ , acceleration due to gravity  $g$  and bank angle  $\sigma$ .

In comparison, a three-state solution would be represented by the following equations of motion (EoM):

$$\begin{aligned}
\dot{r} &= v \cdot \sin(\gamma) \\
\dot{v} &= -\frac{\rho \cdot v^2 \cdot C_{D,SC} \cdot A_{SC}}{2 \cdot m} - g \cdot \sin(\gamma) \\
\dot{\gamma} &= \frac{\rho \cdot C_L \cdot v \cdot A_{SC}}{2 \cdot m} - \cos(\gamma) \cdot \left( \frac{g}{v} - \frac{v}{r} \right)
\end{aligned}$$

### 3.2 Descent

As all Mars landers since Viking 1, the Phoenix spacecraft utilizes a disk-gap-band (DGB) parachute which is deployed in the supersonic flow regime. DGB parachutes were originally envisioned in the 1960s for high-altitude sounding rockets primarily used for weather applications. They were then further developed by NASA for what would become the Viking lander program. A variety of sizes were designed and later successfully tested at sub- and supersonic speeds, for example within wind tunnels and small rockets launched from high-altitude balloons. [18]

The name ‘disk-gap-band’ suggests the basic layout of the parachute. It consists of ‘a flat circular disk and an orthogonal cylindrical band that are separated by a gap between the two’ [18] (see figure 3-5). While the disk is responsible for most of the drag creation, the combination of gap and band improve the stability by letting

the air exit the disk canopy and creating a fixed separation point of the outside flow. The aerodynamic properties of the Phoenix parachute are shown below. [18]

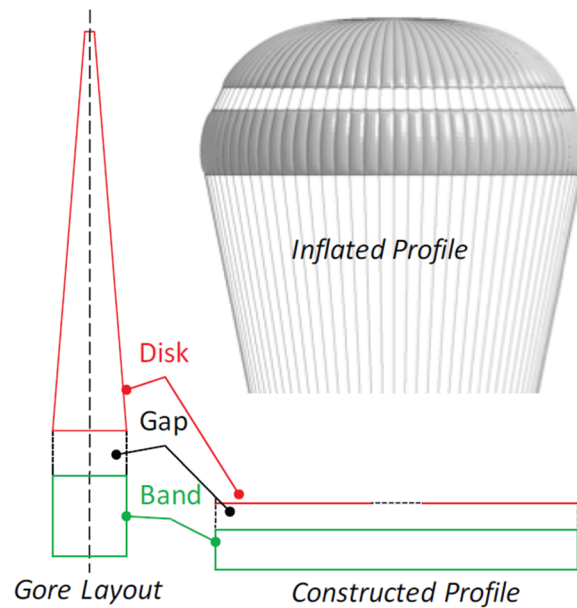


figure 3-5: Disk-gap band parachute basic design layout.

Left: Gore segments, which are stitched together to form the parachute.

Bottom: Constructed profile. Top: Inflated profile [18, p. 2].

The parachute used on the Phoenix landing system has a diameter of 11.73 m [19] resulting in a reference area of 108.065 m<sup>2</sup>. The drag coefficient of this parachute depends on the Mach number and is displayed in figure 3-6.

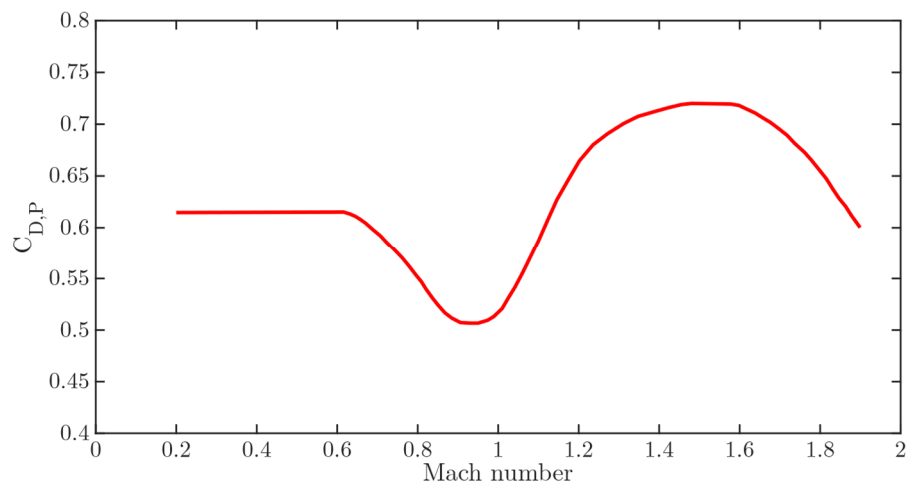


figure 3-6: DGB-parachute drag coefficient in relation to the Mach number, adapted from [20].

To implement the additional drag component of the parachute (P), the equations of motions have to be changed accordingly. The parachute only creates drag and no lift. The appended part is highlighted in bold.

$$\begin{aligned}\dot{r} &= v \cdot \sin(\gamma) + v_{w,vert} \\ \dot{\theta} &= \frac{v \cdot \cos(\gamma) \cdot \sin(\psi) + v_{w,east}}{r \cdot \cos(\phi)} \\ \dot{\phi} &= \frac{v \cdot \cos(\gamma) \cdot \sin(\psi) + v_{w,north}}{r} \\ \dot{v} &= -\frac{\rho \cdot v^2 \cdot (C_{D,SC} \cdot A_{SC} + \mathbf{C}_{D,P} \cdot \mathbf{A}_P)}{2 \cdot m} - g \cdot \sin(\gamma) \\ \dot{\gamma} &= \frac{\rho \cdot C_L \cdot v \cdot A_{SC} \cdot \cos(\sigma)}{2 \cdot m} - \cos(\gamma) \cdot \left(\frac{g}{v} - \frac{v}{r}\right) \\ \dot{\psi} &= \frac{\rho \cdot C_L \cdot v \cdot A_{SC} \cdot \sin(\sigma)}{2 \cdot m \cdot \cos(\gamma)} - \frac{v \cdot \cos(\gamma) \cdot \tan(\phi) \cdot \sin(\psi)}{r}\end{aligned}$$

During the parachute phase, the spacecraft will release the heatshield and thereby expose the lander to the surrounding environment. The on-board radar will boot up and start to measure the distance to the ground. Once the measured distance to the planet crosses a predefined value of 940 m above ground level, the lander is released from the backshell and the landing sequence is initiated.

### 3.3 Landing

In the final seconds of the flight phase, the spacecraft has to reduce its speed from 50-60 m/s to an acceptable landing speed of about 1-3 m/s. Therefore, the Phoenix spacecraft contains a lander module with 293 N monopropellant hydrazine thrusters to decelerate and stabilize the spacecraft. Twelve of these thrusters are pulse-fired to land the spacecraft in a controlled manner. The on-board computer first aims to achieve a constant velocity of about 8 m/s at an altitude of 50 meters [2]. Afterwards, the velocity is reduced to tolerable landing speeds. [21]

Equations of motion solely for the landing:

$$\begin{aligned}\dot{r} &= v \cdot \sin(\gamma) + v_{w,vert} \\ \dot{\theta} &= \frac{v \cdot \cos(\gamma) \cdot \sin(\psi) + v_{w,east}}{r \cdot \cos(\phi)} \\ \dot{\phi} &= \frac{v \cdot \cos(\gamma) \cdot \sin(\psi) + v_{w,north}}{r} \\ \dot{v} &= -\frac{\rho \cdot v^2 \cdot C_{D,SC} \cdot A_{SC}}{2 \cdot m} - g \cdot \sin(\gamma) - \frac{\mathbf{T} \cdot \cos(\beta)}{m} \\ \dot{\gamma} &= \frac{\rho \cdot C_L \cdot v \cdot A_{SC} \cdot \cos(\sigma)}{2 \cdot m} - \cos(\gamma) \cdot \left(\frac{g}{v} - \frac{v}{r}\right) + \frac{\mathbf{T} \cdot \sin(\beta)}{m \cdot v} \\ \dot{\psi} &= \frac{\rho \cdot C_L \cdot v \cdot A_{SC} \cdot \sin(\sigma)}{2 \cdot m \cdot \cos(\gamma)} - \frac{v \cdot \cos(\gamma) \cdot \tan(\phi) \cdot \sin(\psi)}{r}\end{aligned}$$

with: Thrust  $T$  and thrust angle  $\beta$

During the landing phase, the thruster firing leads to a continuous reduction in mass which has to be taken into account when calculating the EoMs:

$$\dot{m} = -\frac{T}{I_{SP} \cdot g_0}$$

with:

$$I_{SP} = 230 \text{ s}$$

Thruster specific impulse [22]

$$g_0 = 9.80665 \text{ m/s}^2$$

Standard acceleration due to gravity (Earth) [23]

## 4 Simulink model

The principal simulation of the motion is performed within MATLAB/Simulink. In the sections below, the influential parameters are described with the key functionality shown in figure 4-1. In general, the motion of the spacecraft is based on a six-state calculation (three for position, three for velocity) which makes it possible to calculate the motion of a point mass in a 3D-environment. ODEs are used to calculate the six states at each time step (red). The ODEs require inputs based on interpolation, constants and controls (black, grey and brown). These are partly based on feedback calculations (green) and event triggers (light blue and purple). Finally, certain visualizations (dark blue) are created within the simulation. The simulation will be stopped as soon as the stop condition (orange) is reached. Each part of the simulation will be explained in the sections below.

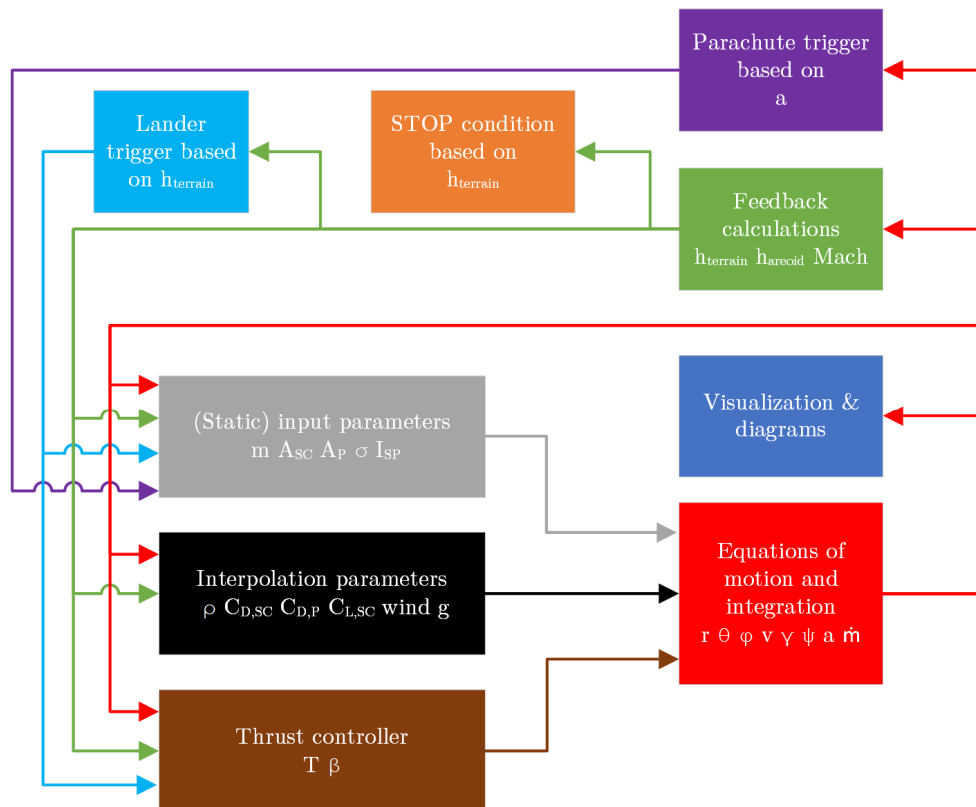


figure 4-1: Block diagram of the simulation with different subsystems.

Grey: (Static) input parameters. Black: Interpolation parameters. Brown: Thrust controller. Red: Equations of motion and integration. Green: Feedback calculations. Light blue and purple: Event triggers. Blue: Visualizations. Orange: Stop condition.

## 4.1 Equations of motion and integration

The equations of motion, which were introduced in the previous chapter, have to be embedded into the simulation. These ODEs are implemented in this subsystem and are integrated with respect to the current time step. The model is built in a way that the same equations of motion are used for the whole simulation. Parameters which are not used at certain points in time are built as a step function: They are held at zero for the times in which they are not used. This applies to parachute area and engine thrust. The basic equations of motion are shown below:

$$\begin{aligned}\dot{r} &= v \cdot \sin(\gamma) + v_{w,vert} \\ \dot{\theta} &= \frac{v \cdot \cos(\gamma) \cdot \sin(\psi) + v_{w,east}}{r \cdot \cos(\phi)} \\ \dot{\phi} &= \frac{v \cdot \cos(\gamma) \cdot \sin(\psi) + v_{w,north}}{r} \\ \dot{v} &= -\frac{\rho \cdot v^2 \cdot (C_{D,SC} \cdot A_{SC} + C_{D,P} \cdot A_P)}{2 \cdot m} - g \cdot \sin(\gamma) - \frac{T \cdot \cos(\beta)}{m} \\ \dot{\gamma} &= \frac{\rho \cdot C_L \cdot v \cdot A_{SC} \cdot \cos(\sigma)}{2 \cdot m} - \cos(\gamma) \cdot \left(\frac{g}{v} - \frac{v}{r}\right) + \frac{T \cdot \sin(\beta)}{m \cdot v} \\ \dot{\psi} &= \frac{\rho \cdot C_L \cdot v \cdot A_{SC} \cdot \sin(\sigma)}{2 \cdot m \cdot \cos(\gamma)} - \frac{v \cdot \cos(\gamma) \cdot \tan(\phi) \cdot \sin(\psi)}{r} \\ \dot{m} &= -\frac{T}{I_{SP} \cdot g_0}\end{aligned}$$

Apart from the integrated values of the equations of motions, further calculations require the spacecraft acceleration  $a = \dot{v}$  which is taken out of the EoMs.



## 4.2 Feedback calculations

These calculations are based on the integrated state parameters from the main equations of motion and are input parameters for multiple calculations downstream which is why they are placed before the parameter computations.

### Altitude over MOLA areoid

Both MarsGRAM and MCD tabular data are based on the MOLA areoid reference altitudes. The areoid radius data of Mars is gathered from MarsGRAM and compared to the current radius. It is not possible to acquire the same data within the web application of MCD which is why MarsGRAM is used for both simulation frames.

$$h_{\text{areoid}} = r - r_{\text{areoid}}$$

### Altitude over terrain

The altitude over the surface is calculated to determine the initiation of the terminal descent and the final guidance. Once again, the radius of the terrain data is always taken from the MarsGRAM simulation as the MCD web interface does not provide detailed terrain data.

In this aspect, a major difference between the databases comes up. While MarsGRAM calculates properties (e.g. density) with no consideration of the actual terrain and therefore also computes values ‘below the surface’, MCD outputs ‘Not a Number’ (NaN) if the location point is considered to be below the actual terrain leading to a simulation cut-off/failure as soon as NaN-values are detected. During the simulations, an altitude resolution of 500 meters is used and therefore the terrain representation within MCD is limited to 500-meter steps. As the landing position dispersion is greatly reduced in the final seconds of landing, a higher simulation cut-off at 600 meters above ground level (AGL) is accepted to be within reasonable bounds for the MCD database.

$$h_{\text{terrain}} = r - r_{\text{terrain}}$$

### Mach number

The Mach number is vital for the calculation of airflow characteristics. The properties and behavior of objects change with the Mach number. For this simulation, the aerodynamic coefficients described in chapter 3 are linked to the Mach number. The Mach number itself links the object speed  $v$  to the speed of sound  $c$ .

$$\text{Ma} = \frac{v}{c} \text{ [dimensionless]}$$

The speed of sound is calculated based on the temperature and chemical composition of the surrounding atmosphere:

$$c = \sqrt{\kappa \cdot R_0 \cdot \frac{T}{M}} \left[ \frac{\text{m}}{\text{s}} \right]$$

with:

$\kappa = c_p/c_v = 1.33$	Ratio of specific heats on Mars [24]
$R_0 = 8.314452618 \text{ [J/(mole*K)]}$	Universal gas constant [25]
$T \text{ [K]}$	Temperature – based on MarsGRAM/MCD
$M \text{ [kg/mole]}$	Molar mass – based on MarsGRAM

### 4.3 Parachute trigger

Triggering the parachute was done based on two parameters in the Phoenix mission: acceleration or velocity. While the acceleration is measured by the on-board accelerometer, the velocity is propagated by the on-board computer based on the entry state which results in a considerable level of uncertainty due to the integration. This uncertainty problem was reconstructed in the Mars 2001 lander mission failure, which only used a velocity trigger. The acceleration trigger was implemented to reduce the dynamic pressure uncertainty at deployment. Furthermore, the trigger is set up in a way that release due to acceleration is very likely. Because of the trigger setting being beneficial for the acceleration threshold and because of the circumstance that no source for the specific velocity value could be found, the trigger will solely be based on acceleration. [19]

Parachute trigger event: Acceleration  $< 7.42 \text{ m/s}^2$  [2]

## 4.4 Lander separation and trigger

The altitude detection is performed with an onboard radar which is turned on after heatshield separation. As the simulation is not capable of simulating a radar measurement, the trigger is simply based on crossing a calculated altitude over terrain value of 940 m. [2]

Lander separation trigger event:  $h_{\text{terrain}} < 940 \text{ m AGL}$  [2]

## 4.5 Interpolation parameters

Based on the data gathered from the atmospheric models MarsGRAM and MCD as well as other diagrams, numerous parameters have to be interpolated. They are described in the following. For all parameters, linear interpolation is used.

### 4.5.1 Vehicle data

One of the primary goals during the hypersonic phase is to create sufficient drag to decelerate the vehicle to a safe parachute deployment velocity. Therefore, it is necessary to describe these aerodynamic properties with coefficients. Additionally, the parachute itself is creating drag to further decelerate the spacecraft. For this simulation, these parameters include the drag coefficients for the spacecraft and the parachute and the lift coefficient for the spacecraft.

#### Spacecraft drag coefficient

The values displayed in figure 3-4 are imported into MATLAB and interpolated on a 3D-grid. As an example, the drag coefficient values are displayed in figure 3-6. The x- and y-axis represent uniform grid values and not the direct Mach number and angle of attack directly.

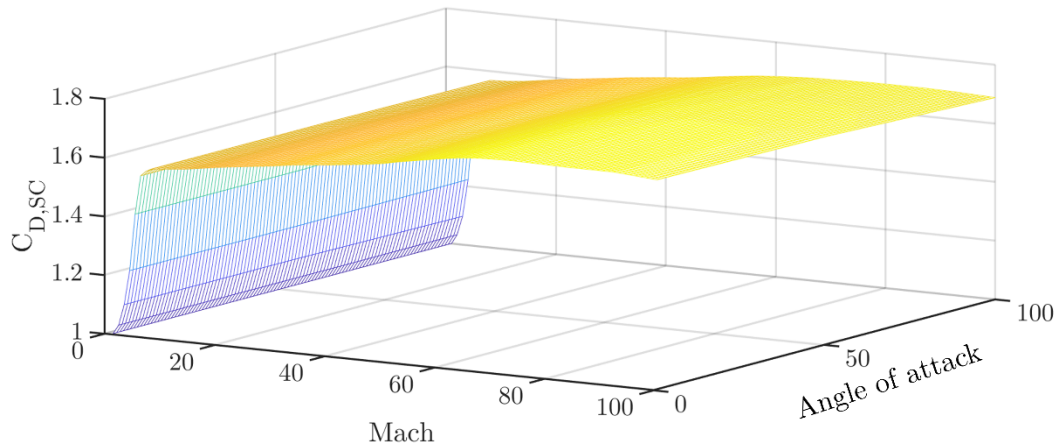


figure 4-2: Processed drag coefficient data.

The Mach and AoA axis display the data on a uniform grid with 100 data points each.

### Parachute drag coefficient

The parachute drag coefficient data displayed in figure 3-6 is only dependent on the Mach number and can thus be used by implementing a 2D-lookup table with linear interpolation. The Mach number is the input and the drag coefficient is the output.

#### 4.5.2 Atmospheric and planet data

Data derived from the atmospheric models has to be interpolated based on the created 3D-grid of the atmospheric models. Within the simulation, the following parameters are interpolated in this way:

- Density
- Density perturbations
- Wind (vertical, eastward and northward)
- Wind perturbations (vertical, eastward and northward)
- Temperature
- Molar mass
- Acceleration due to gravity

Density and wind (and their perturbations) are used within the equations of motion. Hence, they are key parameters. The temperature and molar mass are used for the calculation of the Mach number in the feedback loop.

Acceleration due to gravity is a parameter which is dependent on the distance from the planet but also the planet itself. While a simple calculation based on the

standard gravitational parameter GM and radius r would be possible, MarsGRAM can output g based on the shape of the areoid resulting in a better depiction of reality.

The output of the data by MarsGRAM and MCD is in tabulated format. These tables are imported into MATLAB as a 3D-array. It is necessary to interpolate the data to achieve the desired data accuracy. Due to the three-dimensional grid data, the interpolation has to be performed within a box of 8 surrounding values (see figure 4-3) which will be explained below (tri-linear interpolation). In this example, the density is used as the parameter which is interpolated.

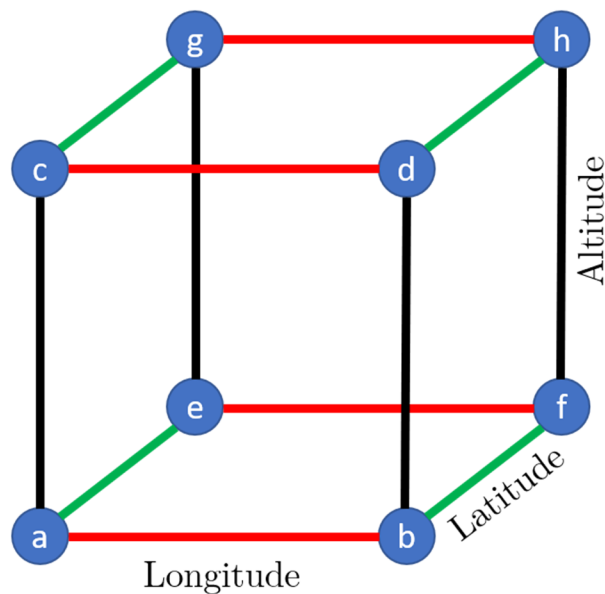


figure 4-3: Data grid box.

Blue: Data point. Red: Longitude. Green: Latitude. Black: Altitude.

Each corner point of the box contains a density value from the database. Firstly, the densities in the lower longitude lines are interpolated to the detailed longitude values ( $\rho_{\text{I}}$  and  $\rho_{\text{II}}$ ). Secondly, they are further interpolated to the specific latitude value ( $\rho_{\text{III}}$ ). Thirdly, this calculation is repeated for the upper plane (resulting in  $\rho_{\text{VI}}$ ). Finally,  $\rho_{\text{III}}$  and  $\rho_{\text{VI}}$  are interpolated to the final value  $\rho_{\text{VII}}$ . The exact method is described below (see figure 4-4 as reference). Additionally, a detailed description with an example containing real model data can be found in annex 12.2.

1. Interpolate a and b to  $\rho_I$
2. Interpolate e and f to  $\rho_{II}$
3. Interpolate  $\rho_I$  and  $\rho_{II}$  to  $\rho_{III}$
4. Interpolate c and d to  $\rho_{IV}$
5. Interpolate g and h to  $\rho_V$
6. Interpolate  $\rho_{IV}$  and  $\rho_V$  to  $\rho_{VI}$
7. Interpolate  $\rho_{III}$  and  $\rho_{VI}$  to  $\rho_{VII}$

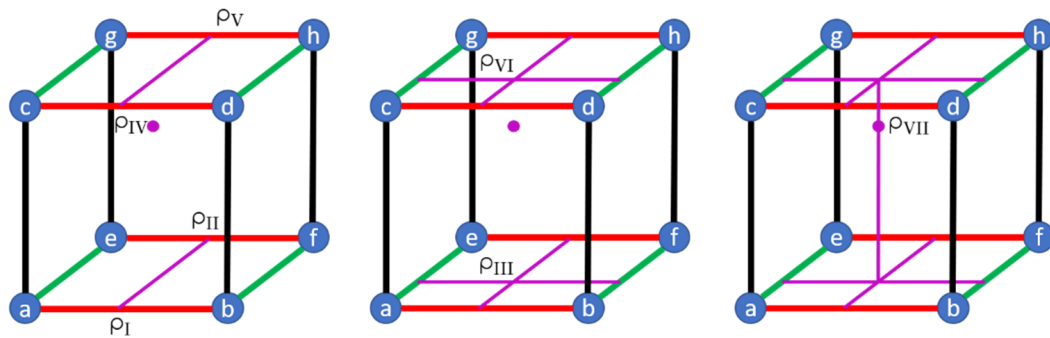


figure 4-4: Tri-linear interpolation procedure of a data grid box from left to right.

Blue: Data point. Red: Longitude. Green: Latitude. Black: Altitude.

Purple: Interpolation lines.

## 4.6 (Static) input parameters

The input parameter values include the mass, the reference area of the parachute and the spacecraft, the bank angle and the specific impulse of the landing thrusters. While most of them are constant, the mass and the parachute area change over time.

### Mass

Parts of the spacecraft are shed or jettisoned during the entry, descent and landing procedure and the thrusters require propellant. Consequently, it is necessary to define the mass value accordingly as it is impacting the motion of the spacecraft directly.

Initially, the Phoenix spacecraft has a mass of 582 kg at atmospheric entry (after cruise stage separation). Due to lack of data, the reduction of heatshield mass because of ablation during re-entry is not taken into account. 15 seconds after parachute deployment, the heatshield is discarded which reduces the mass by 62 kg. Initializing the terminal descent phase, the lander separates from the backshell

(110 kg, including the parachute) and the thrusters are fired up less than one second later. During terminal descent, the thrusters are continuously turned on and throttled to the required values (see section 4.7 for thrust regulation) in the simulation. In contrast, the real Phoenix lander used pulsed thrusters instead of throttled thrusters. However, this change is made to simplify the simulation. A typical timeline of the mass can be seen in figure 4-5. [21]

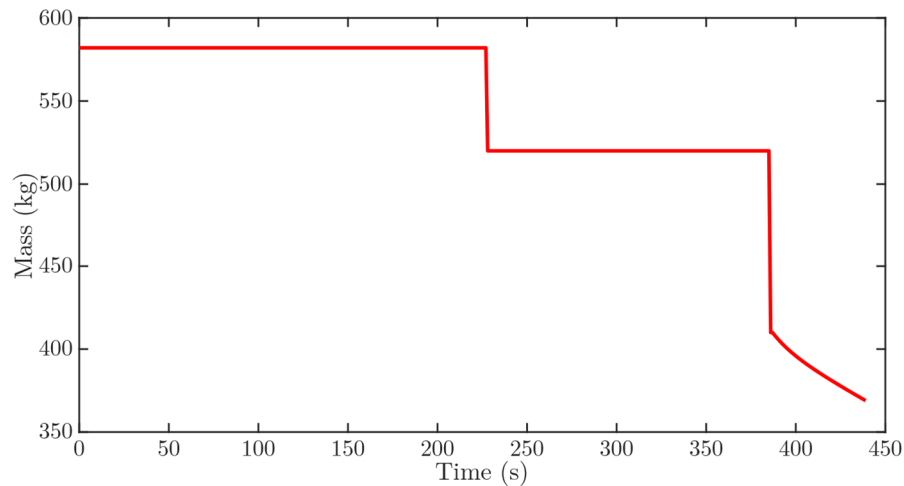


figure 4-5: Mass-time relation.

First event: Heatshield separation. Second event: Backshell separation.

Last section: Thruster operation.

### Other

More variables are set as follows:

$A_{SC} = 5.5155 \text{ m}^2$	Spacecraft reference area, see section 3.1
$A_P = 108.065 \text{ m}^2$	Parachute reference area, see section 3.2
$\sigma = 180^\circ = 3.14159 \text{ rad}$	Bank angle [2]
$\alpha = 0^\circ = 0 \text{ rad}$	Angle of attack
$I_{SP} = 230 \text{ s}$	Specific impulse, see section 3.3
$g_0 = 9.80665 \text{ m/s}^2$	Standard acceleration due to gravity, see section 3.3

## 4.7 Thrust controller

The terminal descent phase is challenging as the propulsion system has to ensure to decelerate the spacecraft to a vertical velocity of 1 – 3.4 m/s at touchdown. Therefore, the terminal descent is separated into two phases by one distinct event: Achieving a constant velocity of 8 m/s at an altitude of about 50 m above the surface. Upon reaching constant velocity, the spacecraft determines the thrust profile required until touchdown.

The thrust controller subsystem is activated when the lander separation altitude of 940 m AGL is crossed. The thrust control within the simulation is achieved with a PI-controller with a target velocity of 8 m/s. However, a new target of the landing velocity of 1-3.4 m/s is not placed. Tests show that variations in the atmospheric data can lead to an off-nominal controller reaction which results in vertical velocities in upwards directions. Therefore, a final velocity of 8 m/s is found to be sufficient for the level of detail given in the simulation. Furthermore, the flight-path angle during terminal descent is close to 90 degrees, so the main investigation point of landing site dispersion is hardly impacted by this. Additionally, the controller output has a saturation limit of the maximum thrust of the twelve thrusters ( $12 \times 293 \text{ N} = 3516 \text{ N}$ ). A thrust profile can be seen in figure 4-6.

The controller parameters are found through a trial-and-error method for the nominal trajectory which achieve a flight profile that reaches a constant velocity between 50 and 100 meters: Proportional (P) 70 and Integral (I) 3.2.

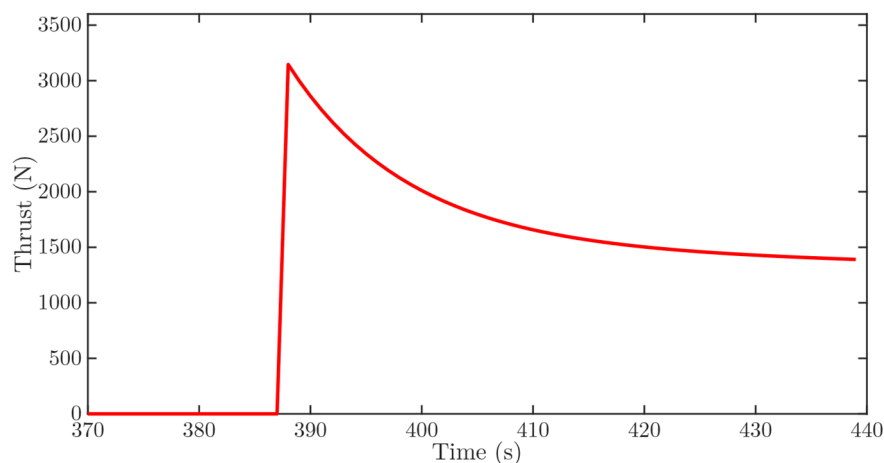


figure 4-6: Thrust-time relation during the landing phase of the spacecraft.  
The thrust decreases with the real velocity.



## 4.8 Stop condition

To avoid continuing the simulation until the maximum runtime is achieved, a stop-condition is placed based on the altitude above the terrain. The threshold value is zero meters for MarsGRAM and, as mentioned in section 4.2, 600 meters for MCD.

## 4.9 Validation

In order to validate the simulation, the results have to be compared to real data of the Phoenix lander. Phoenix entered the atmosphere of Mars on 25<sup>th</sup> of May 2008 at 23:30:57 Earth UTC time and touched down on the surface seven minutes and 22 seconds later. Within this timeframe, the spacecraft withstood high decelerations and high temperatures, successfully released and inflated its parachute, and finally separated from the backshell and landed on the surface with the aid of hydrazine thrusters. The section below shows a comparison between the real data and the created simulation. As the simulation is based on a point mass and does not consider uncertainties, a fair level of dispersion is found to be accepted. table 4-1 shows the entry conditions of the spacecraft. [26]

table 4-1: Initial conditions at entry. [26]

Parameter	Symbol	Unit	Value
Radius	$r$	m	3.522297379878062e+6
Longitude	$\theta$	deg	197.6893345424510
Latitude	$\phi$	deg	69.363798394042846
Velocity (inertial)	$v_i$	m/s	5600.273271498325
Flight-path angle (inertial)	$\gamma_i$	deg	-13.014149720113631
Azimuth (inertial)	$\psi_i$	deg	77.701926824525046

Due to its landing position in the high latitude regime, the entry position is equally situated in the near vicinity. Entering the atmosphere at the pre-defined interface of a 3522.2 km radius and a position of 69.4° N 197.7° E, it follows the path displayed in figure 4-7 (blue). For comparison, the simulation results for MarsGRAM (red) and MCD (green) are shown as well. Because of the fact that the simulation is based on a point-mass and does not consider uncertainties on the entire spacecraft (e.g. aerodynamics), the results are considered to be reasonably accurate and therefore validated.

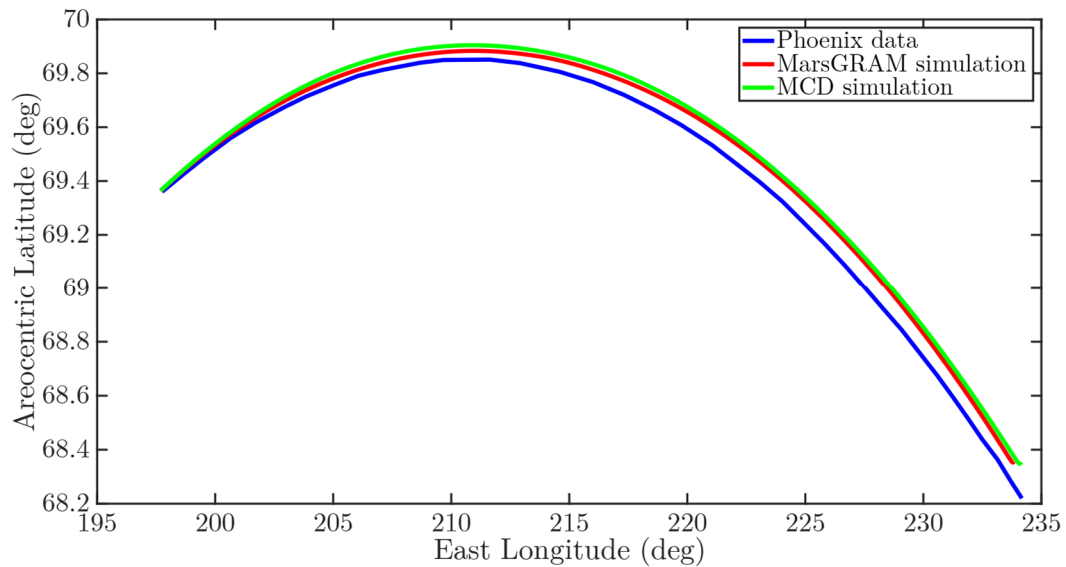


figure 4-7: Longitude-latitude comparison of Phoenix data with MarsGRAM and MCD.  
Blue: Phoenix data [26]. Red: MarsGRAM. Green: MCD.

In figure 4-8, the velocity is displayed in relation to the altitude above ground. For both the real data and the simulations, the deceleration phase begins at approximately 60-70 kilometers. In the MarsGRAM simulation, the velocity is reduced first, followed by MCD and finally the real data. The simulations overestimate the density at these altitudes in comparison to the environment encountered on the landing day. However, the results of the simulation do not vary significantly.

Below a velocity of 2000 m/s, the discrepancies decrease, and the three trajectories are close together. While both simulations deploy the parachute at approximately the same time, the Phoenix data diverts considerably. In figure 4-9, the course of the real Phoenix graph shows the velocity deviation from the simulations after about 150 seconds and also a 10 second delay for the parachute deployment.

This can be traced back to two factors. First of all, the simulations do not account for a non-zero angle of attack (AoA). As this work analysis the differences in the atmospheric models, it is of no consequence whether the spacecraft is flown with an angle of attack or not. The prediction for the real flight was that the AoA would remain below 0.5 degrees during the high deceleration phase except for short stages of static instability. Trajectory reconstruction and the landing point at the edge of the predicted landing ellipse reveal that the Phoenix spacecraft entered with an average AoA of approximately three degrees. Consequently, it flew on a lifted trajectory which resulted in a drawn-out altitude reduction. [2]

Due to the lifted trajectory, the decrease in deceleration after the peak is also slower (see figure 4-10). Consequently, the acceleration threshold for the parachute release is triggered later than expected (6.4 seconds during the real flight [2]). Apart from the release delay, the diagram curves for the acceleration coincide well. The peak deceleration of the Phoenix lander is halfway between the simulated predictions of MarsGRAM and MCD. The constant deviation in the last 170 seconds can be traced back to the acceleration due to gravity which is detected by the real sensor.

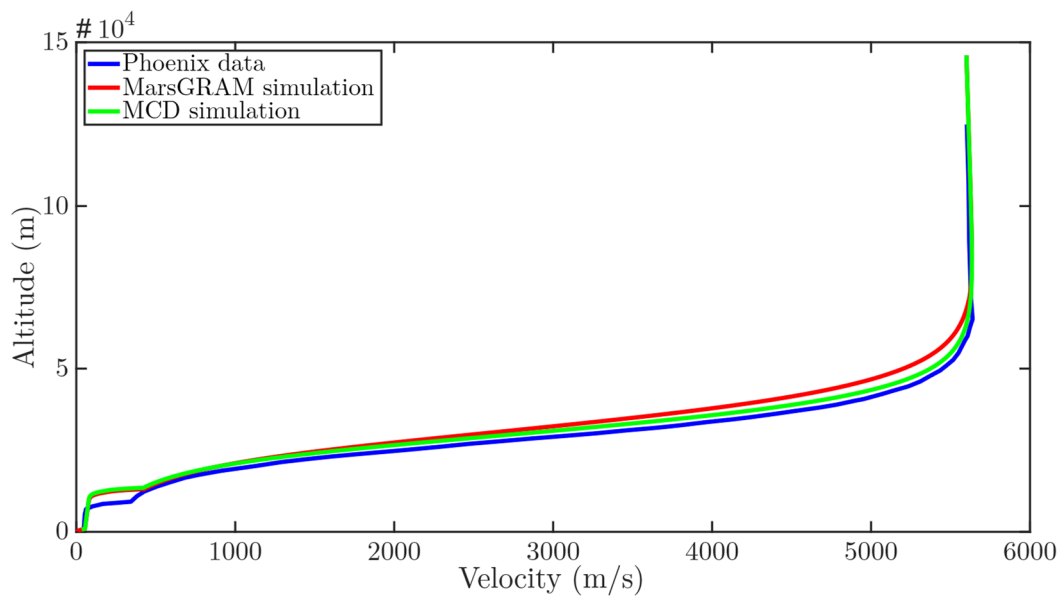


figure 4-8: Velocity-altitude comparison of Phoenix data with MarsGRAM and MCD.  
Blue: Phoenix data [20]. Red: MarsGRAM. Green: MCD.

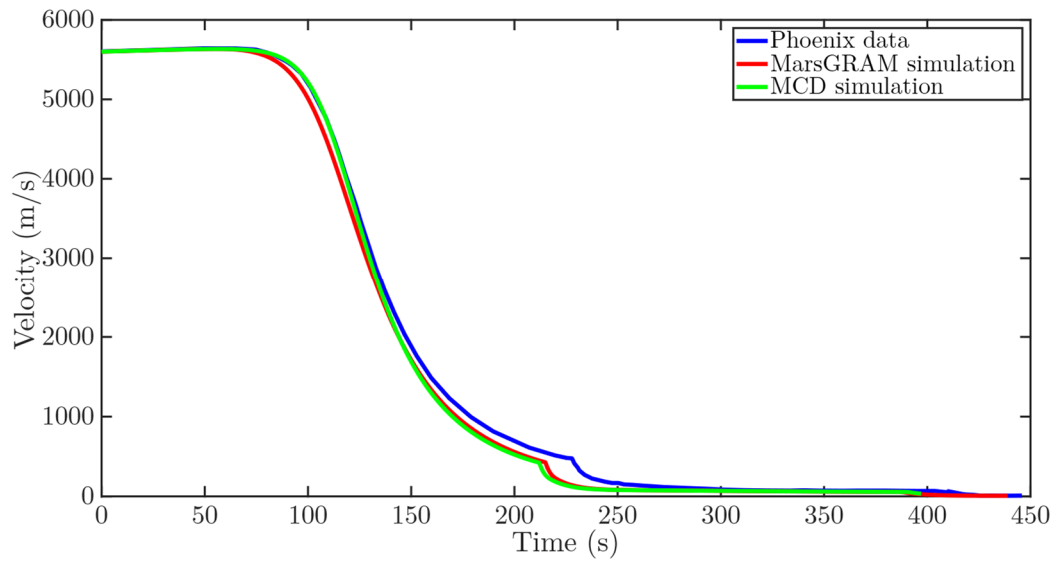


figure 4-9: Time-velocity comparison of Phoenix data with MarsGRAM and MCD.  
Blue: Phoenix data [26]. Red: MarsGRAM. Green: MCD.

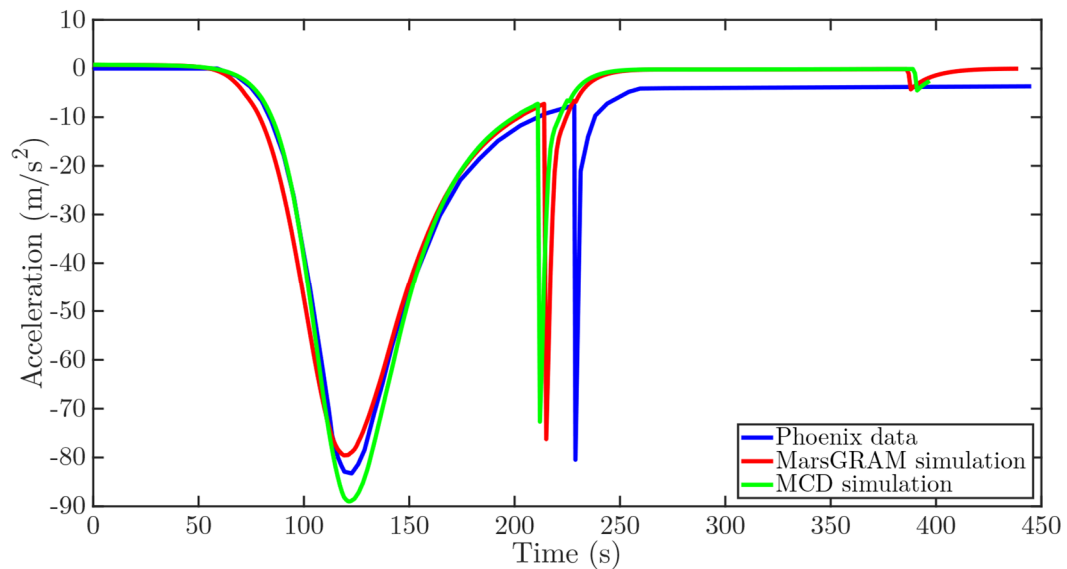


figure 4-10: Time-acceleration comparison of Phoenix data with MarsGRAM and MCD.  
Blue: Phoenix data [26]. Red: MarsGRAM. Green: MCD.

The atmospheric density in relation to the altitude is shown in figure 4-11 in a semi-logarithmic diagram. While the simulation densities are directly gathered from the atmospheric models, the real data is based on a trajectory reconstruction using the accelerometer data. Because of the resolution of the sensor, the data is only useable below 80 kilometers at which point the atmosphere is sufficiently dense. Above 50 kilometers, the Phoenix data correlate well with the MCD database. Due to the logarithmic scale, the MarsGRAM data diverts considerably and is the reason for the deceleration in the higher altitudes analyzed in figure 4-8.

Nevertheless, below 50 kilometers, the correlation between the three graphs improves significantly until they can be considered equal at approximately 35 kilometers above the ground. In conclusion, the established simulation has a good correlation with real-life data from the entry interface until touchdown.

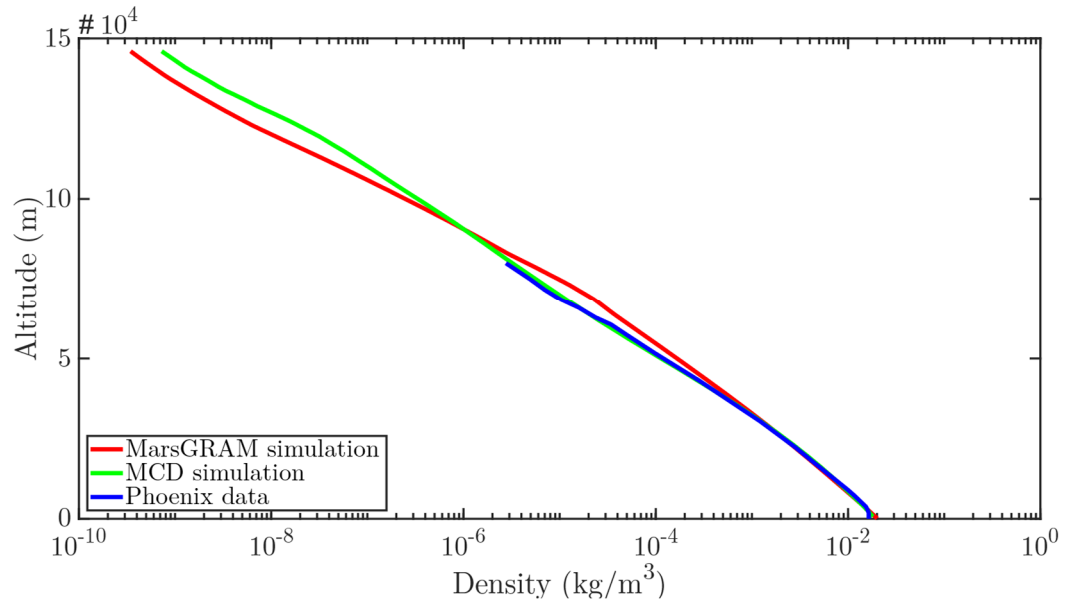


figure 4-11: Density-altitude comparison of Phoenix data with MarsGRAM and MCD.  
Blue: Phoenix data [26]. Red: MarsGRAM. Green: MCD.

## 5 Stochastic methods

Analyzing the performance of re-entry trajectory based on stochastic methods is an important part of the pre-flight analysis. It can determine expected and/or unexpected deviations from the nominal trajectory and therefore increase the likelihood of a safe and successful mission. The sections below introduce the required stochastic terms and the principal methods used – Monte Carlo and linear covariance analysis.

### 5.1 Introduction to stochastics

Before a statistical analysis is performed, a few terms and the corresponding nomenclature has to be introduced. In general, stochastics is the superordinate term for two mathematical fields: Probability theory and statistics. Both fields are part of this work which is why the necessary terms will be described below. Because of the utilization of the atmospheric databases as the uncertainty terms, the term ‘luck’ is not an explicit part of this analysis. Instead, the models output distributions of the data and the impact on the final result has to be analyzed. The explanations are based on ‘Elementare Stochastik’ by Ehrhard Behrends [27].

**Random variable:** Within a given probability space  $\Omega$ , a random variable  $X$  defines the outcome of a mapping by a function. A specific probability applies to each outcome.

**Probability:** The likelihood  $P(x)$  that a specific outcome occurs.

**Expected value:** The expected value  $E(X)$  is the average value a discrete random variable  $X$  is expected to obtain.

$$E(X) = \sum_{i \in \Omega} x_i \cdot P(x_i)$$

**Variance:** As the outcome will only be an average of the expected value, the dispersion from the expected value – the variance  $V(X)$  – has to be defined.

$$V(X) = E\left(\left(X - E(X)\right)^2\right)$$

**Standard deviation:** The square root of the variance is the standard deviation  $\sigma$ .

$$\sigma(X) = \sqrt{V(X)}$$

**Normal distribution:** If a probability space can be defined by density functions, the normal distribution is a symmetrical distribution around the expected value. The standard deviation can be used to define the probability that an outcome occurs in a certain range around the expected value:

$\pm 1 \sigma \rightarrow 68.27$  percent of all values

$\pm 2 \sigma \rightarrow 95.45$  percent of all values

$\pm 3 \sigma \rightarrow 99.73$  percent of all values

In engineering, the three-sigma value is a commonly used threshold in terms of accepted technical boundaries. As an example, the landing ellipse of a re-entry vehicle is defined as 3-sigma landing ellipse leading to a 99.73 percent probability that the lander will touchdown within the given range.

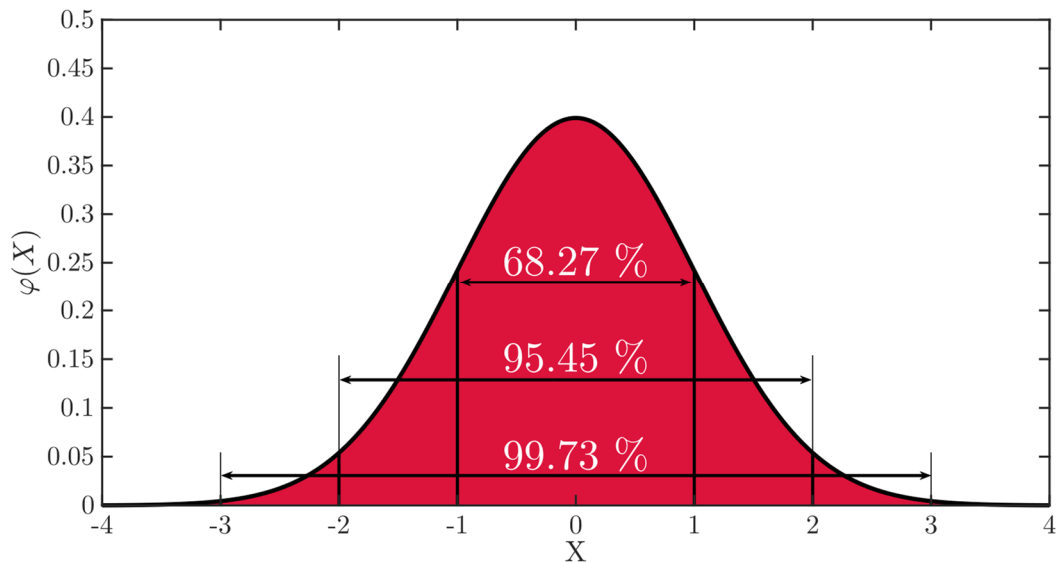


figure 5-1: Standard normal distribution.

$$E(X) = 0, \sigma(X) = 1$$

**Covariance:** If there are two random variables  $X$  and  $Y$ , the covariance describes the change of the variable  $Y$  depending on the variable  $X$  (co-vary). For example, if  $X$  rises, the covariance can describe whether  $Y$  also rises, whether it does not change at all or whether it declines.

$$\text{Cov}(X, Y) = E\left(\left(X - E(X)\right) \cdot \left(Y - E(Y)\right)\right)$$

**Covariance matrix:** If there are multiple random variables, the covariance matrix describes the covariances between each random variable.

$$C(X) = \begin{pmatrix} \text{Cov}(X_1, X_1) & \text{Cov}(X_1, X_2) & \dots & \text{Cov}(X_1, X_n) \\ \text{Cov}(X_2, X_1) & \text{Cov}(X_2, X_2) & \dots & \text{Cov}(X_2, X_n) \\ \vdots & \vdots & \ddots & \vdots \\ \text{Cov}(X_n, X_1) & \text{Cov}(X_n, X_2) & \dots & \text{Cov}(X_n, X_n) \end{pmatrix}$$

As the Covariance of a variable  $X_n$  with itself is the variance, the diagonal of the covariance matrix shows all the variances and therefore squares of the standard deviation. Additionally, the covariance is symmetrical along the main diagonal as  $\text{Cov}(X_1, X_2) = \text{Cov}(X_2, X_1)$ .

**Confidence ellipse:** The Monte Carlo simulation can be plotted into a distribution of landing points around the nominal trajectory. In order to assess the distribution, confidence ellipses are created based on the 1, 2 and 3-sigma values (e.g. 2-sigma ellipse contains 95.45 percent of all landing points). These are important as comparative data for other simulation runs. The confidence ellipses are based on an iso-contour of the Gaussian distribution and explained in the following based on a nominal example of a MarsGRAM simulation. At first, the 2x2 covariance matrix of the dataset is created: [28]

$$C = \begin{pmatrix} 0.0241 & -0.0028 \\ -0.0028 & 0.0007 \end{pmatrix}$$

Then, the eigenvectors and eigenvalues of the covariance matrix are found (see figure 5-2). The eigenvalues define the spread in the direction of the eigenvectors. Due to the elliptical shape, the rotation angle of the ellipse is defined as the angle between the x-axis and the largest eigenvector.

If a two-dimensional Gaussian distribution is assumed, a Chi-Square distribution with two degrees of freedom can be fitted to the sum of the squared data points. With the square root of the Chi-Square probability  $\chi$  calculated from the given confidence value (e.g.  $\chi = 2.4860$  for 95.45 percent or 2-sigma), the confidence and consequently the size of the ellipse can be calculated. The semi-major and semi-minor axis are calculated as follows.

$$a = \chi * \sqrt{\max(\text{Eigenval})}$$

$$b = \chi * \sqrt{\min(\text{Eigenval})}$$



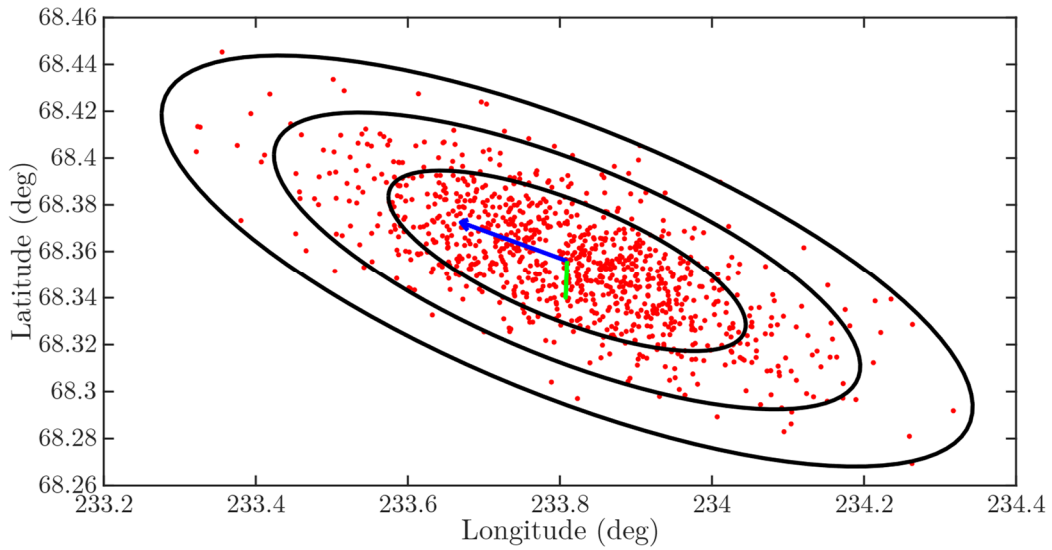


figure 5-2: 1, 2 and 3-sigma confidence ellipses (black) and their eigenvectors.  
 Red: Landing data of nominal Phoenix landing with MarsGRAM.  
 Blue: Largest eigenvector. Green: Smallest eigenvector.

## 5.2 Monte Carlo method

In general, the Monte Carlo method is used when a calculation (for instance a re-entry problem) is subject to uncertainties. Thus, a precise mathematical outcome (like  $1 + 1 = 2$ ) cannot be given. These uncertainties are based on the limit of humanity's ability to understand and measure physical quantities. Due to the atmospheric analysis in this work, the elements of uncertainty are density as well as horizontal and vertical wind velocities. However, uncertainty parameters are not limited to these and could include, but are not limited to, aerodynamics, sensor data and actuator plus control performance.

As mentioned in section 2.2.2, the web version of the MCD database is not able to output vertical wind perturbations. Consequently, a fair comparison between MarsGRAM and MCD shall not include this parameter. Going forward, the vertical wind perturbations are only included within an internal comparison of the MarsGRAM database to quantify the difference of the vertical wind perturbations. Models and equations are subscripted by  $(10 \times 10)$  to indicate the presence of vertical wind perturbations and  $(9 \times 9)$  to indicate the absence of said parameter.

Because of the vast number of influential factors, the accurate prediction of the atmospheric condition is complex and not possible with today's technology as it would be necessary to measure the state of every cubic meter of air in the

atmosphere. Due to a high number of weather stations and satellites and additionally personnel effort, it is possible to predict high- to low-level weather phenomena on Earth with a moderate to high accuracy. However, the weather information available for Mars is solely based on successful missions in which the landers flew through the atmosphere and were able to provide data through reconstruction and measurements from space. Therefore, the available data for Mars is subject to a high level of uncertainty.

The setup of a Monte Carlo simulation is straight forward in its approach. At first, a nominal trajectory is computed with average parameter values. Afterwards, the simulation is repeated  $N$  times (here: 1000) with randomized uncertainty parameters and the dispersions from the nominal trajectory can be analyzed. For the randomized parameters, a random number generator function based on a normal distribution (expected value: 0, standard deviation: 1) is used as this is the expected distribution of the provided data.

### 5.3 Linear Covariance Analysis

Utilizing Monte Carlo analysis for trajectory prediction and uncertainty dispersions is a solid method that will, given the correct inputs, lead to satisfying results. However, a major disadvantage of Monte Carlo is the required computing effort. Therefore, alternative computations are desired which lead to equally fitting results at a greatly reduced runtime. One such alternative is Linear Covariance Analysis (LCA) in its form detailed by David Geller. In the following, a description of the tool is given based on the paper ‘Development and Validation of Linear Covariance Analysis Tool for Atmospheric Entry’ by David Geller et al. [17].

In general, LCA uses a linearization of the modelling equations along a previously determined nominal trajectory to identify the dispersions. While the dispersions are small, this is a valid approach as the linearized equations are still valid. Within the linear model, the primary function is a covariance propagation equation in which the model deviations and the truth equations (equations of motions) are handled. A detailed description will be discussed in the sections below.

The described LCA tool is based on a guided entry trajectory. The change of aerodynamic lift by commanding the bank angle and the angle of attack is used to control the trajectory based on a given nominal path. The nominal path would be

computed with an optimal control problem. In contrast, the entry of the Phoenix spacecraft is not controlled. Therefore, the tool has to be adapted from a closed-loop (guided) to an open-loop (unguided) system. This leads to an order of magnitude in complexity reduction. The following description of the method displays the complete method including the guided system and explains where simplifications can be made.

### 5.3.1 Covariance methods

#### Nonlinear modelling

Before linearization, the nonlinear model has to be built up in its most general form. In a first instance,  $\mathbf{x}$  represents the states of the spacecraft  $\rightarrow \mathbf{x} = [\mathbf{r}, \theta, \phi, \mathbf{v}, \gamma, \psi]^T$ . The full truth model is depicted in section 5.3.2.

True state vector:

$$\dot{\mathbf{x}} = \mathbf{f}(\mathbf{x}, \hat{\mathbf{u}}, \mathbf{t}) + \mathcal{B} \cdot \omega$$

with command vector  $\hat{\mathbf{u}}$  (the hat operator indicates command), vector of zero-mean white-noise process  $\omega$  and scale factor  $\mathcal{B}$ .

Because there is no command in a non-guided system and additionally this re-entry simulation for Mars will solely investigate atmospheric uncertainties, which are simulated parametrically, random noise processes will also be neglected.

$$\dot{\mathbf{x}} = \mathbf{f}(\mathbf{x}, \mathbf{t})$$

#### Linear modelling

The following equations are a linearization of the nonlinear model along the previously determined nominal trajectory, which is described in  $\bar{\mathbf{x}}(\mathbf{t})$ .

Time evolution of the true state dispersions:

$$\delta \mathbf{x}(\mathbf{t}) = \mathbf{x}(\mathbf{t}) - \bar{\mathbf{x}}(\mathbf{t})$$

State propagation equations:

$$\delta \dot{\mathbf{x}} = \mathbf{F}_{\mathbf{x}} \cdot \delta \mathbf{x} + \mathbf{F}_{\hat{\mathbf{u}}} \cdot \hat{\mathbf{G}}_{\hat{\mathbf{x}}} \cdot \hat{\mathbf{x}} + \mathcal{B} \cdot \omega$$

With: partial derivate matrices  $\mathbf{F}_{\mathbf{x}}$  and  $\mathbf{F}_{\hat{\mathbf{u}}}$  (see below), commanding algorithms  $\hat{\mathbf{G}}$

It is reduced to:

$$\delta \dot{\mathbf{x}} = \mathbf{F}_{\mathbf{x}} \cdot \delta \mathbf{x}$$

$F_x$  (and  $F_{\hat{u}}$ ) are partial derivative matrix of the state vector along the nominal trajectory. As an example, the derivatives of a three-state system  $x = [r, v, \gamma]^T$  are shown (3x3). Because of the truth models depicted in section 5.3.2,  $F_x$  is more complex (10x10 or 9x9) and therefore added to the annex (see annex 12.3)

$$F_x = \frac{\partial f}{\partial x} \Big|_{\bar{x}} = \begin{bmatrix} \frac{\partial \dot{r}}{\partial r} & \frac{\partial \dot{r}}{\partial v} & \frac{\partial \dot{r}}{\partial \gamma} \\ \frac{\partial \dot{v}}{\partial r} & \frac{\partial \dot{v}}{\partial v} & \frac{\partial \dot{v}}{\partial \gamma} \\ \frac{\partial \dot{\gamma}}{\partial r} & \frac{\partial \dot{\gamma}}{\partial v} & \frac{\partial \dot{\gamma}}{\partial \gamma} \end{bmatrix} \Big|_{\bar{x}}$$

$$= \begin{bmatrix} 0 & \sin(\gamma) & v \cdot \cos(\gamma) \\ 0 & -\frac{A_{SC} \cdot C_{D,SC} \cdot \rho \cdot v}{m} & -g \cdot \cos(\gamma) \\ -\frac{v \cdot \cos(\gamma)}{r^2} & \cos(\gamma) \cdot \left(\frac{g}{v^2} + \frac{1}{r}\right) + \frac{A_{SC} \cdot C_L \cdot \rho}{2 \cdot m} & \sin(\gamma) \cdot \left(\frac{g}{v} - \frac{v}{r}\right) \end{bmatrix} \Big|_{\bar{x}}$$

### Augmented linear system

The linearized equations are augmented to be able to compute the true state dispersions.

Augmented state vector:

$$X = \begin{bmatrix} \delta x \\ \delta \hat{x} \end{bmatrix}$$

Because there is no guided system, it is reduced to:

$$X = [\delta x]$$

Augmented state propagation equations:

$$\dot{X} = \mathcal{F} \cdot X + \mathcal{G} \cdot \eta + \mathcal{W} \cdot \omega$$

with:

$$\mathcal{F} = \begin{pmatrix} F_x & F_{\hat{u}} \hat{G}_{\hat{x}} \\ \hat{F}_{\tilde{y}} C_x & \hat{F}_{\hat{x}} + \hat{F}_{\tilde{y}} C_{\hat{u}} \hat{G}_{\hat{x}} \end{pmatrix}$$

$$\mathcal{G} = \begin{pmatrix} 0_{n \times 1} \\ \hat{F}_{\tilde{y}} \end{pmatrix}$$

$$\mathcal{W} = \begin{pmatrix} \mathcal{B} \\ 0_{\hat{n} \times n_{\omega}} \end{pmatrix}$$

0 indicates a matrix of zeros,  $\tilde{y}$  continuous inertial measurements and  $C_x$  the covariance of the augmented state vector.

This is reduced to:

$$\dot{X} = \mathcal{F} \cdot X$$

with:

$$\mathcal{F} = (\mathcal{F}_x)$$

Due to the following connections in the expected values,

$$E[x(t)] = E[\bar{x}(t)]$$

$$E[\delta x(t)] = E[x - \bar{x}] = 0$$

the expected value or mean of the augmented state vector is:

$$E[X] = 0$$

This leads to the conclusion that the true dispersions computed by the LCA are symmetric. The following propagation equations (1<sup>st</sup>) are valid for the covariance of the augmented system (2<sup>nd</sup>):

$$\dot{C}_X = \mathcal{F} \cdot C_X + C_X \cdot \mathcal{F}^T + \mathcal{G} \cdot \mathcal{S}_\eta \cdot \mathcal{G}^T + \mathcal{W} \cdot \mathcal{S}_\omega \cdot \mathcal{W}^T$$

$$C_X = E[X(t)X^T(t)]$$

with variance of the inertial instrument measurement noise  $\mathcal{S}_\eta$  and variance of the unmodeled accelerations  $\mathcal{S}_\omega$ .

Because of the simplifications, this is reduced to:

$$\dot{C}_X = \mathcal{F} \cdot C_X + C_X \cdot \mathcal{F}^T$$

The propagation equation is solved numerically either with a fixed-step fourth order Runge-Kutta or a variable step solver (e.g. ODE45, ODE23 or ODE15). ODE45 is the standard solver within the MATLAB/Simulink suite, is based on an algorithm by Dormand and Prince and is delivering good results for most problems. However, ODE23 and ODE15 will also be analyzed in order to quantify the differences between them. They choose the step size based on the functions at hand. In contrast, the step size needs to be chosen beforehand for Runge-Kutta 4 (RK4). RK4 is based on the following functions [29]:

$$y_{n+1} = y_n + \frac{1}{6}h \cdot (k_1 + 2 \cdot k_2 + 2 \cdot k_3 + k_4)$$

with:

$$\begin{aligned} k_1 &= f(t_n, y_n) \\ k_2 &= f\left(t_n + \frac{1}{2}h, y_n + \frac{1}{2}h \cdot k_1\right) \\ k_3 &= f\left(t_n + \frac{1}{2}h, y_n + \frac{1}{2}h \cdot k_2\right) \\ k_4 &= f(t_n + h, y_n + h \cdot k_3) \end{aligned}$$

### Performance evaluation

Without a closed-loop system, only the true state dispersions are of interest. These are calculated by analyzing the variances which are in the diagonal of the covariance matrix. In the guided system, they are calculated as follows:

$$D_{\text{true}} = E[\delta x(t)\delta x^T(t)] = (I_{n \times n} \mathbf{0}_{n \times \hat{n}})C_X(I_{n \times n} \mathbf{0}_{n \times \hat{n}})^T$$

This is reduced to:

$$D_{\text{true}} = E[\delta x(t)\delta x^T(t)] = (I_{n \times n})C_X$$

In order to identify the true dispersions, the standard deviation must be derived from the variance by extracting the square root. The three-sigma values are attained by multiplying the single sigma values by three.

$$D_{\text{true},\sigma} = \begin{pmatrix} \sigma_r & 0 & \cdots & 0 \\ 0 & \sigma_\theta & \cdots & 0 \\ \vdots & \vdots & \ddots & \vdots \\ 0 & 0 & 0 & \sigma_\psi \end{pmatrix}$$

### 5.3.2 Truth models

Within the LCA, the influential parameters are the true states based on the equations of motion  $x_{\text{EoM}}$  and the uncertainty values  $p$ . These have to be defined in the true state vector:

$$x = (x_{\text{EoM}}, p)^T$$

Based on the given re-entry problem, the states for the vehicle are shown below. The equations of motions, which are used to calculate these values, are displayed in chapter 3.

$$x_{\text{EoM}} = (r, \theta, \phi, v, \gamma, \psi)^T$$

In general, the uncertainty parameters can be varied widely and are only limited to the ability to model them mathematically. For a re-entry vehicle, exemplary

parameters are atmospheric (e.g. wind and density), aerodynamic coefficients (lift and drag), sensor data and more. However, as this work analyzes the influence of the atmospheric uncertainties, it will solely focus on density and wind. According to the used spherical coordinate system (see chapter 3), the wind data is separated into eastward, northward and vertical direction (10x10 represents the parameters including vertical wind perturbations, 9x9 without  $\rightarrow$  based on the size of  $F_x$ ):

$$\begin{aligned} \mathbf{p} &= (\mathbf{p}_\rho, \mathbf{p}_{w,east}, \mathbf{p}_{w,north}, \mathbf{p}_{w,vert})_{(10 \times 10)}^T \\ &= (\mathbf{p}_\rho, \mathbf{p}_{w,east}, \mathbf{p}_{w,north})_{(9 \times 9)}^T \end{aligned}$$

These parameters are all assumed to not be time-dependent, leading to a derivative of zero. Consequently, the assumed density and wind speeds are either globally overestimated or underestimated in a simulation. While this might not reflect reality perfectly because the parameters are not necessarily over-/underestimated in the whole data grid, it is chosen for a consistent test area within the simulation. Because of the symmetry of the LCA, it is not necessary to calculate the results of both an over-estimated and under-estimated world.

$$\mathbf{p}_\rho = \rho_N + \rho_{SD}$$

$$\mathbf{p}_{w,east} = \mathbf{v}_{w,east,N} + \mathbf{v}_{w,east,SD}$$

$$\mathbf{p}_{w,north} = \mathbf{v}_{w,north,N} + \mathbf{v}_{w,north,SD}$$

$$\mathbf{p}_{w,vert} = \mathbf{v}_{w,vert,N} + \mathbf{v}_{w,vert,SD}$$

Due to the introduction of uncertainty parameters, the equations of motion change as follows (10x10):

$$\begin{aligned} \dot{r} &= v \cdot \sin(\gamma) + (\mathbf{v}_{w,vert,N} + \mathbf{v}_{w,vert,SD}) \\ \dot{\theta} &= \frac{v \cdot \cos(\gamma) \cdot \sin(\psi) + (\mathbf{v}_{w,east,N} + \mathbf{v}_{w,east,SD})}{r \cdot \cos(\phi)} \\ \dot{\phi} &= \frac{v \cdot \cos(\gamma) \cdot \sin(\psi) + (\mathbf{v}_{w,north,N} + \mathbf{v}_{w,north,SD})}{r} \\ \dot{v} &= -\frac{(\rho_N + \rho_{SD}) \cdot v^2 \cdot (C_{D,SC} \cdot A_{SC} + C_{D,P} \cdot A_P)}{2 \cdot m} - g \cdot \sin(\gamma) - \frac{T \cdot \cos(\beta)}{m} \\ \dot{\gamma} &= \frac{(\rho_N + \rho_{SD}) \cdot C_L \cdot v \cdot A_{SC} \cdot \cos(\sigma)}{2 \cdot m} - \cos(\gamma) \cdot \left( \frac{g}{v} - \frac{v}{r} \right) + \frac{T \cdot \sin(\beta)}{m \cdot v} \\ \dot{\psi} &= \frac{(\rho_N + \rho_{SD}) \cdot C_L \cdot v \cdot A_{SC} \cdot \sin(\sigma)}{2 \cdot m \cdot \cos(\gamma)} - \frac{v \cdot \cos(\gamma) \cdot \tan(\phi) \cdot \sin(\psi)}{r} \end{aligned}$$

### 5.3.3 Initial conditions

The analysis tool has to be fed with an initial condition of the uncertainties. At the initial state, the uncertainties are implemented into the covariance matrix  $P_{x,0}$ .

$$C_X(t_0) = \begin{bmatrix} E[\delta x_0 \delta x_0^T] & 0_{n \times \hat{n}} \\ 0_{\hat{n} \times n} & E[\delta \hat{x}_0 \delta \hat{x}_0^T] \end{bmatrix}$$

Which is reduced to:

$$C_X(t_0) = [E[\delta x_0 \delta x_0^T]] = [P_{x,0}]$$

Assuming no correlation between the initial uncertainties, the covariance matrix  $P_{x,0}$  is only filled with values in the main diagonal and therefore with variances of the uncertainties. Because of the uncertainties only being placed upon the atmospheric parameters, the six state parameters have a variance value of zero. In contrast, the variances of the atmospheric parameters are equal to the squared standard deviations. These deviations are imported from the nominal trajectory and updated through each time step of the LCA.

$$P_{x,0}(\text{diag}) = \begin{pmatrix} 0 \\ 0 \\ 0 \\ 0 \\ 0 \\ 0 \\ \sigma_\rho^2 \\ \sigma_{w,\text{east}}^2 \\ \sigma_{w,\text{north}}^2 \\ \sigma_{w,\text{vert}}^2 \end{pmatrix}_{(10 \times 10)} = \begin{pmatrix} 0 \\ 0 \\ 0 \\ 0 \\ 0 \\ 0 \\ \sigma_\rho^2 \\ \sigma_{w,\text{east}}^2 \\ \sigma_{w,\text{north}}^2 \end{pmatrix}_{(9 \times 9)}$$



## 6 Monte Carlo analysis

The results of the Monte Carlo analysis of the Phoenix using the MarsGRAM and MCD databases are detailed below. It begins with a general description of the different cases depicted and is followed by a comparison of them.

### 6.1 MarsGRAM

The MarsGRAM section is separated into ‘with’ and ‘without’ vertical perturbations to quantify and qualify the effect of this parameter being present or absent.

#### Without vertical perturbations

In figure 6-1, the results of the Monte Carlo analysis for the nominal Phoenix landing case using the MarsGRAM database are shown. The diagrams display the dispersions of the six spacecraft states from the nominal trajectory – radius  $r$ , longitude  $\theta$ , latitude  $\varphi$ , velocity  $v$ , flight-path angle  $\gamma$  (FPA) and velocity azimuth angle  $\psi$  (VAA). In this case, the nominal trajectory is represented by the zero line and has a flight length of about 440 seconds. While some of the other Monte Carlo flight runs exceed this flight time, the diagrams are cut off at the nominal trajectory flight time to evaluate the outcomes up to this point. One distinct milestone in the flight is the parachute deployment at about 215 seconds into the flight.

The dispersion of the radius and velocity coincides with the increase in density and therefore also with aerodynamic drag over the course of the flight. In the first 80 seconds of the flight, the density and the uncertainty thereof is low. Between this point in time and the parachute deployment, the variances in aerodynamic drag lead to increasing dispersions up to about  $\pm 750$  meters at about 150 seconds before a slight reduction until parachute deployment. This concurs with the velocity dispersion which has its peak at about 110 seconds. A reduction in velocity leads to a steeper flight-path angle and consequently a higher decrease in altitude sometime after the velocity reduction. The flight-path angle increases on a curve until about 150 seconds which is when the majority of velocity dispersion is vanished, and all MC runs are at similar velocities again. Consequently, the flight-path angle dispersions increase almost linearly after this point.

The parachute deployment is a determining point in the flight path. Due to the release trigger being sensitive to a certain deceleration limit, the Monte Carlo runs do not deploy the parachute simultaneously. This can be seen in the diagrams for radius, velocity and flight-path angle. At 215 seconds, there is a sudden leap in the radius and velocity dispersions. The abrupt decrease in velocity because of the parachute leads to a reduction in vertical velocity. Consequently, MC runs, which have not had a parachute deployment, lose more altitude because of the higher velocity magnitude (or vice versa) – although the flight-path angle is shallower.

If the parachute is already released, the flight-path angle will increase. This is why the peak flight-path angle dispersions happen about 20 seconds after the deployment on the nominal trajectory. While some runs are still in the aerodynamic entry phase, the nominal trajectory has already had parachute deployment and consequently a rise in the flight-path angle (or vice versa).

The radius dispersions are roughly constant during the parachute phase at up to  $\pm 900$  meters and decrease only after backshell release and thruster initiation at about 388 seconds. This outcome is expected as all MC runs follow a similar flight pattern in this phase.

In contrast, the longitude, latitude and velocity azimuth angle dispersions can mainly be traced back to the influence of wind. In the beginning of the flight, both longitude and latitude are subject to small dispersions due to wind. These small dispersions are also evident in the VAA and result in a different path for the rest of the flight. The primary increase in these states result from the velocity dispersion as the velocity is the main coefficient in all their equations of motions. The inflection point of all the curves overlaps with the peak in velocity dispersion. After this point, the rise in deviations decreases until they stay constant after parachute deployment. At this point in the flight, the velocity is so low that no major course correction can be expected as long as high wind velocities do not move the spacecraft into a certain direction

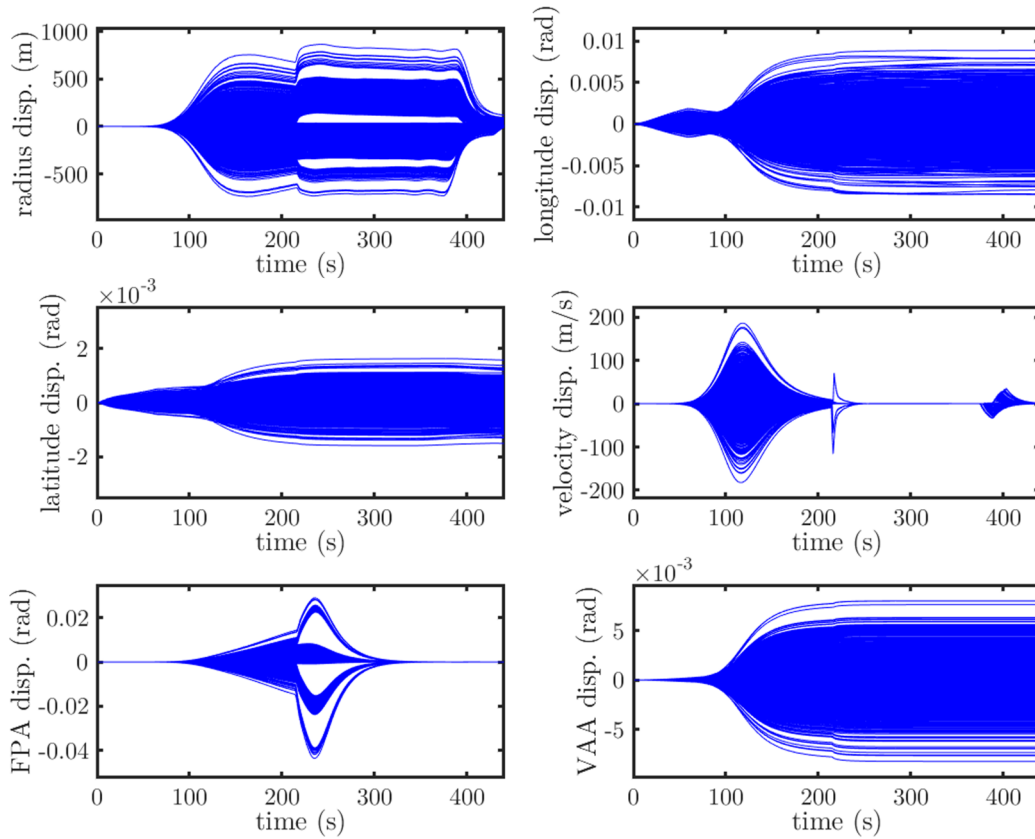


figure 6-1: Monte Carlo analysis MarsGRAM without vertical perturbations.  
Dispersion of spacecraft states from nominal trajectory.

### With vertical perturbations

In order to identify the differences evolving from evicting the vertical perturbations, a Monte Carlo run with activated vertical wind perturbations is shown in figure 6-2. In general, the results are quite similar with a few distinct differences.

First of all, the highest positive and negative dispersions are about ten to twenty percent higher in comparison with the MC run without vertical perturbations except for the flight-path angle. The flight-path angle dispersion peaks at about  $\pm 0.06$  rad in comparison to  $+0.03$  and  $-0.04$  rad.

Another key difference is the radius dispersion in the first 100 seconds. Because of vertical perturbations, the dispersion does not stay close to zero in the beginning but increases immediately after flight initiation.

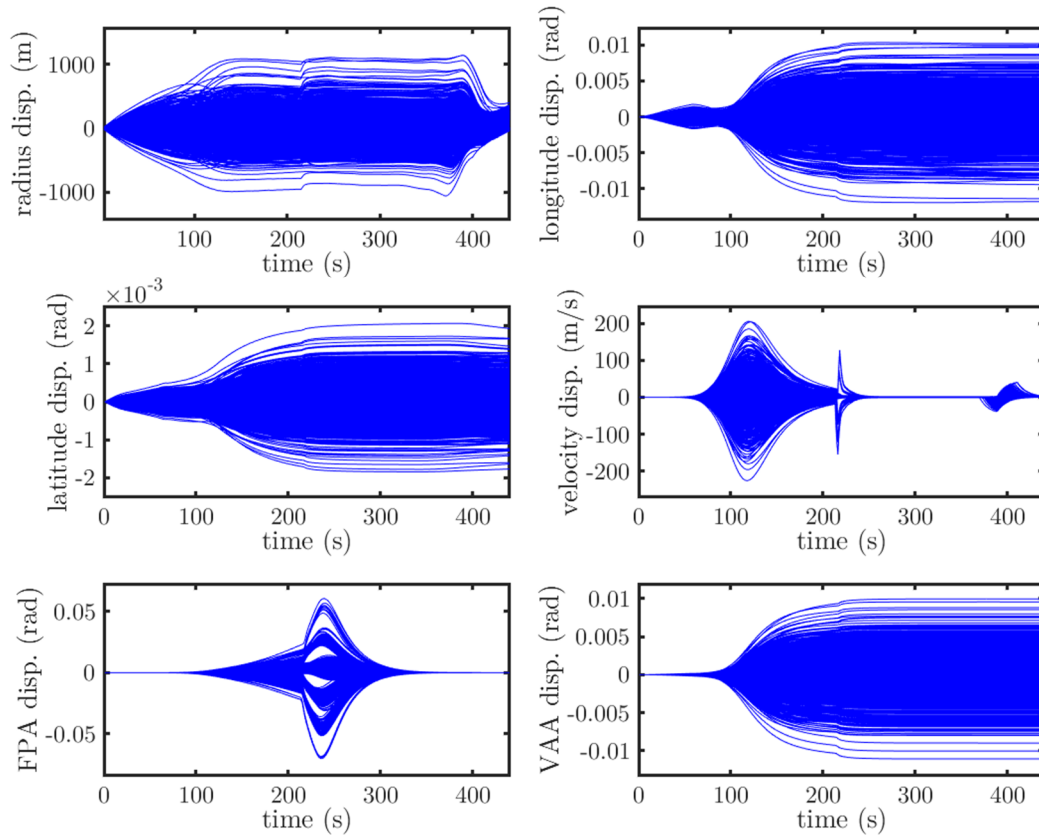


figure 6-2: Monte Carlo analysis MarsGRAM with vertical perturbations.  
Dispersion of spacecraft states from nominal trajectory.

### Landing point evaluation

While a thorough evaluation of the landing points including three sigma landing ellipses will be part of chapter 8, the difference between a Phoenix landing including vertical perturbations and not including them using the MarsGRAM database will be shown in this section. This is done in order to assess the differences going forward.

In figure 6-3, the landing points of a Monte Carlo run using the MarsGRAM database with and without vertical perturbations are shown. Additionally, the confidence ellipses with 1, 2 and 3-sigma values are plotted in the respective colors of the data points. The perturbations of the vertical wind solely influence the landing ellipse in the direction of the semi-major axis. This result is in line with the expectations as a vertical wind does not have an impact on the lateral trajectory.

While the vertical perturbations do have an impact on the outcome of the Monte Carlo analysis, the results can be applied to simulations without vertical perturbations by increasing the size of the semi-major axis of the confidence ellipses.

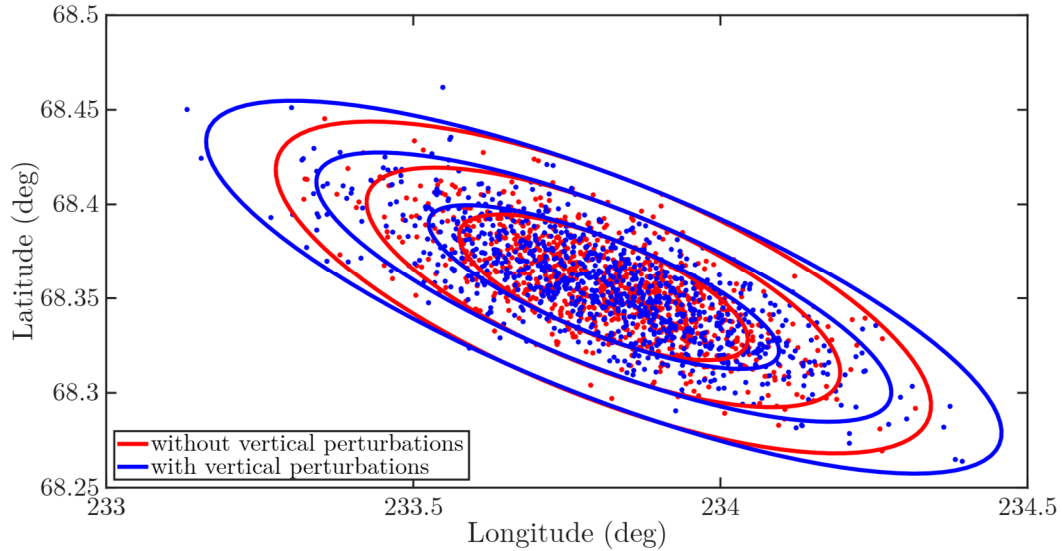


figure 6-3: Landing points of 1000 Monte Carlo runs of the Phoenix spacecraft using MarsGRAM with (blue) and without (red) vertical perturbations. 1, 2 and 3-sigma confidence ellipses for both datasets.

## 6.2 MCD

In general, the Monte Carlo results of the MCD database look similar to the results of MarsGRAM (see figure 6-4). However, the data does possess distinct differences which will be described below. As the web version of MCD is not capable of exporting vertical wind perturbations, this section solely focuses on the simulation without vertical wind perturbations.

The radius and velocity dispersions are about half of MarsGRAM's which can be attributed to lower standard deviations of the density as the primary factor for these states. Due to the cut-off altitude of 600 meters for the MCD database, the flight time is lower at only 398 seconds and the radius dispersion does not decrease as much in the last part of the flight as it was the case for MarsGRAM.

The deviations of flight-path and velocity azimuth angle are similar in shape. The magnitudes of the values for the VAA are about half of MarsGRAM's. Because of the lower velocity dispersions, the VAA dispersions are also lower.

From the beginning of the flight until parachute deployment, the course of the latitude and longitude dispersions are similar to MarsGRAM at a magnitude of about 50 percent. However, after parachute deployment, the latitude and longitude dispersions increase considerably. The wind in the lower altitude regime has to be significantly higher in the MCD simulation than in the MarsGRAM simulation.

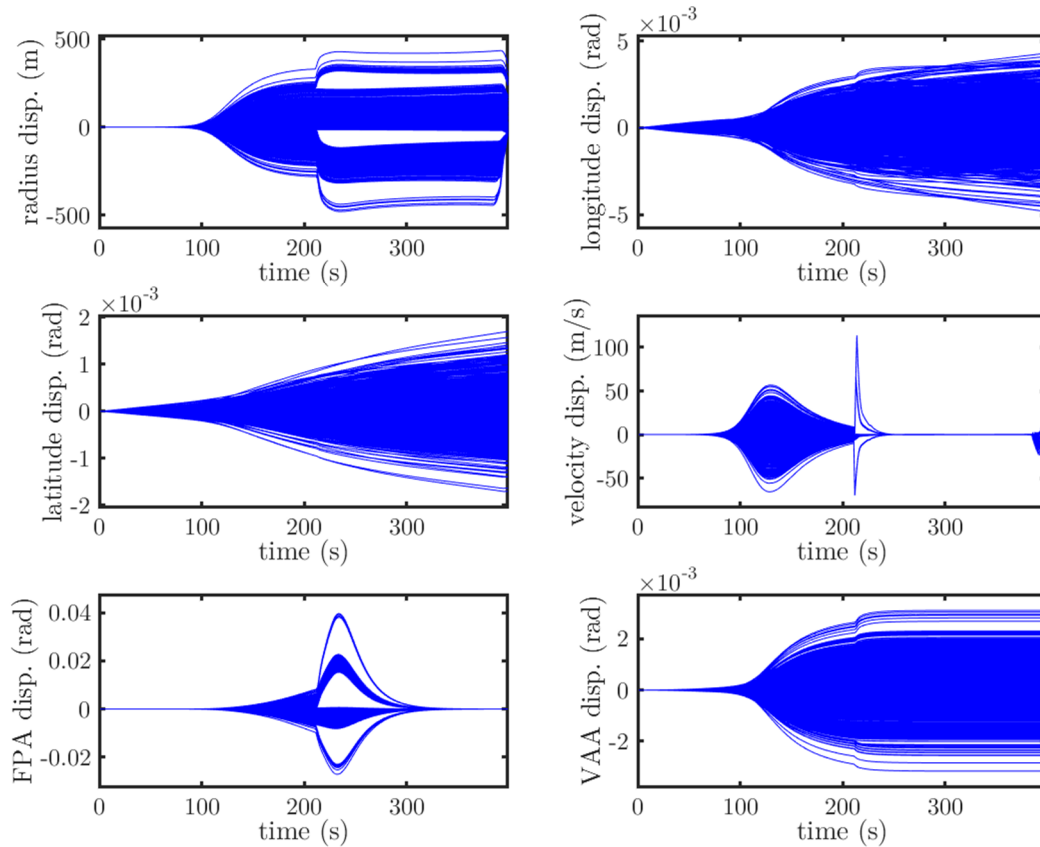


figure 6-4: Monte Carlo analysis MCD without vertical perturbations.  
Dispersion of spacecraft states from nominal trajectory.

## 7 Comparison of LCA and MC

Ultimately, the Linear Covariance Analysis shall be used to replace or at least complement the computation intensive Monte Carlo analysis. Therefore, the results have to be verified in order to be used independently from the MC analysis. The verification is performed by comparing the three-sigma LCA results to the Monte Carlo analysis. A successful outcome would indicate that the LCA is able to depict the three sigma boundaries of the Monte Carlo analysis approximately.

The following sections assess the results of the LCA from various perspectives. At first, the outcomes of the nominal Phoenix Landing for both MarsGRAM and MCD will be studied. Afterwards, the LCA and Monte Carlo analyses are broken down into the separate uncertainty parameters to identify the impact of each one. Finally, the choice of the solver for the differential equations within the LCA is studied. Due to continuity, the nominal Phoenix landing is used for the verification of the linear covariance analysis results.

### 7.1 MarsGRAM without vertical perturbations

In order to apply the same methodology, the results for MarsGRAM are analyzed both for ‘with’ and ‘without’ vertical wind perturbations, commencing with the former. In figure 7-1, the results of the linear covariance analysis are displayed and overlaid with the Monte Carlo simulation runs. While the results will be analyzed in detail below, the general outcome is satisfactory. There are no major discrepancies between both analyses.

The radius dispersion match between LCA and MC is good for the majority of the simulation. Between 100 and 150 seconds, the LCA increase is not as fast as in the outer parts of the MC analysis. Additionally, the LCA is not able to show the decrease in radius dispersion after 380 seconds during the terminal landing sequence when all simulation runs end up at a similar MOLA altitude due to the flat terrain.

While the conformity of the longitude dispersion is satisfactory over the entire simulation, the latitude dispersion of the LCA diverges from the Monte Carlo results in the second half of the simulation. It obtains a maximum diversion of about  $0.5 \times 10^{-3}$  rad (equal to approximately  $0.02865^\circ$ ) in the end.

The matches for velocity, flight-path angle and velocity azimuth angle are in good agreement. The parachute deployment results in a few minor mismatches like the peak in velocity deviation. The LCA solely considers the path of the nominal trajectory and therefore only has knowledge of parachute deployment for a single time step. As analyzed in section 6.1, the simulation deploys the parachute based on an acceleration threshold and can therefore vary. Consequently, the LCA is not capable of displaying the spike in velocity dispersion in the ten seconds after parachute deployment.

Additionally, while the LCA is able to consider the majority of the flight-path angle changes after parachute deployment, it diverges for boundary cases of early parachute deployment.

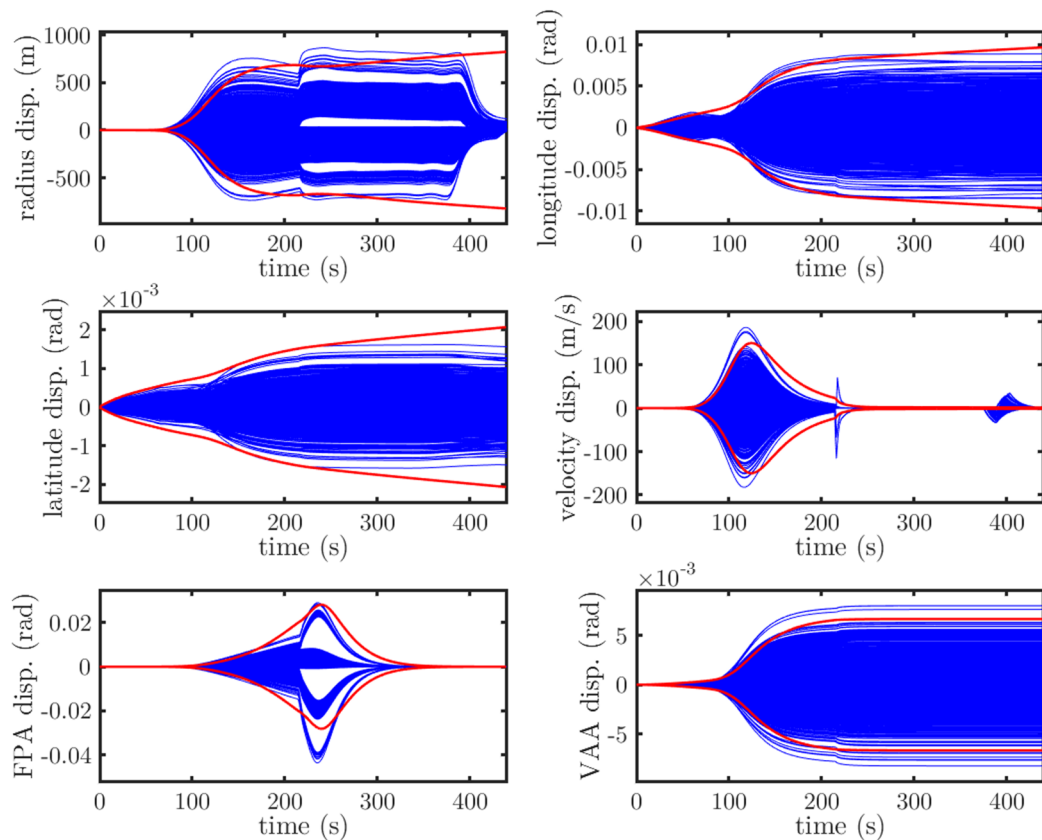


figure 7-1: MarsGRAM without vertical perturbations LCA results superimposed with Monte Carlo runs.

Red: LCA. Blue: MC runs.



An important factor of the analysis is the display of the landing points and the confidence ellipses for one, two and three-sigma. While the initial results of the LCA data shows a noteworthy dispersion of the latitude value, it does not indicate the shape of the confidence ellipse. Therefore, an assessment not only of the variances or standard deviations is required but also of the covariances to identify how they change collectively.

The covariance matrix of the longitude and latitude for this case is as follows:

$$\begin{bmatrix} \sigma_{\theta}^2 & \text{Cov}(\sigma_{\theta}\sigma_{\phi}) \\ \text{Cov}(\sigma_{\theta}\sigma_{\phi}) & \sigma_{\phi}^2 \end{bmatrix} = \begin{bmatrix} 1.037317 * 10^{-5} \text{ rad}^2 & -5.3834 * 10^{-7} \text{ rad}^2 \\ -5.3834 * 10^{-7} \text{ rad}^2 & 4.7922 * 10^{-7} \text{ rad}^2 \end{bmatrix}$$

These values are converted to degrees and can be plotted into one, two and three-sigma confidence ellipses (see figure 7-2).

$$\begin{bmatrix} \sigma_{\theta}^2 & \text{Cov}(\sigma_{\theta}\sigma_{\phi}) \\ \text{Cov}(\sigma_{\theta}\sigma_{\phi}) & \sigma_{\phi}^2 \end{bmatrix} = \begin{bmatrix} 0.03405 \text{ deg}^2 & -1.76736 * 10^{-3} \text{ deg}^2 \\ -1.76735 * 10^{-3} \text{ deg}^2 & 1.573186 * 10^{-3} \text{ deg}^2 \end{bmatrix}$$

The shapes of the confidence ellipses are in line with the expectations. The orientation of the semi-major axis is approximately equal to the Monte Carlo confidence ellipses. Due to the results analyzed beforehand, the differences in the semi-minor axis correspond to the analyzed divergence in the latitudinal direction. The maximum difference between the three-sigma ellipses is approximately 0.03 degrees in the latitude direction and therefore matching the gap in figure 7-1. Because of the unequally scaled axes, the difference is more pronounced in the diagram than the 0.03 degrees value would indicate.

All in all, the results of the linear covariance analysis for the MarsGRAM Phoenix landing without vertical perturbations are suitable at an acceptable level.

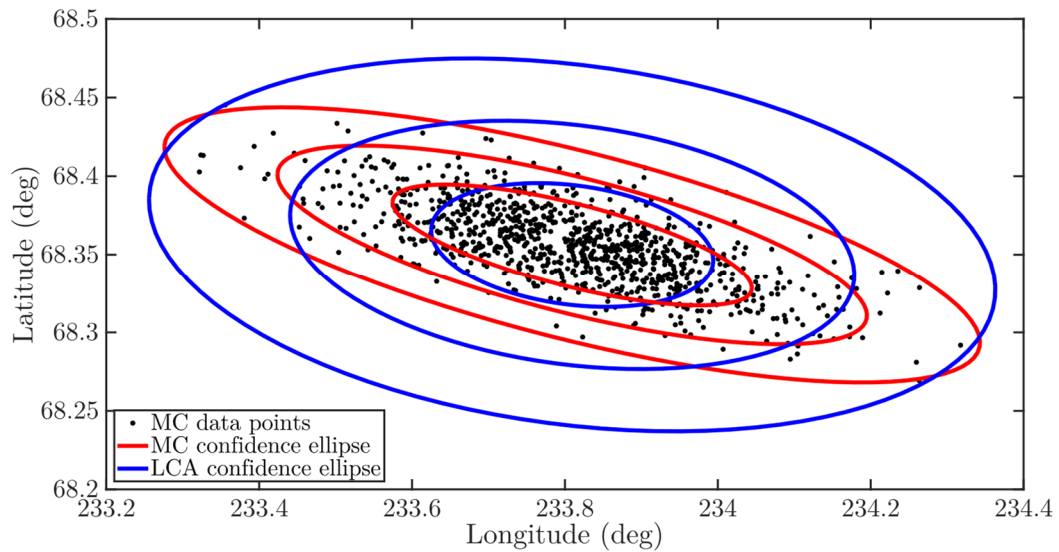


figure 7-2: Surface landing points of LCA and MC.

Black: Monte Carlo data points. Red: 1, 2 and 3-sigma Monte Carlo confidence ellipses.

Blue: 1, 2 and 3-sigma LCA confidence ellipses.

As indicated in figure 7-1, the differences between the dispersions for longitude and latitude increase towards the end of the simulation. Therefore, an examination of the two key time steps parachute deployment (215 seconds) and lander separation (388 seconds) will be performed.

The situation at parachute deployment is shown in figure 7-3 and at lander separation in figure 7-4. The change of the covariance ellipses clearly demonstrates the decrease in inaccuracy for the LCA. After the re-entry phase, the match between LCA and MC is excellent – especially for the 3-sigma ellipses. However, the match accuracy (mainly perpendicular to the semi-major axis) decreases during the parachute descent and during the terminal descent phase.

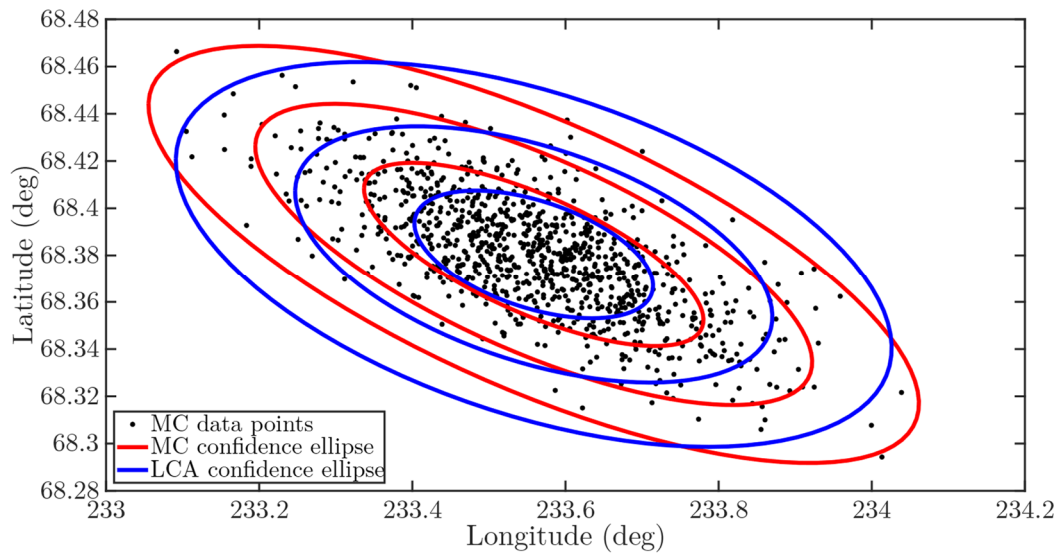


figure 7-3: Points on the trajectory of LCA and MC at parachute deployment (215 seconds).

Black: Monte Carlo data points. Red: 1, 2 and 3-sigma Monte Carlo confidence ellipses.  
Blue: 1, 2 and 3-sigma LCA confidence ellipses.

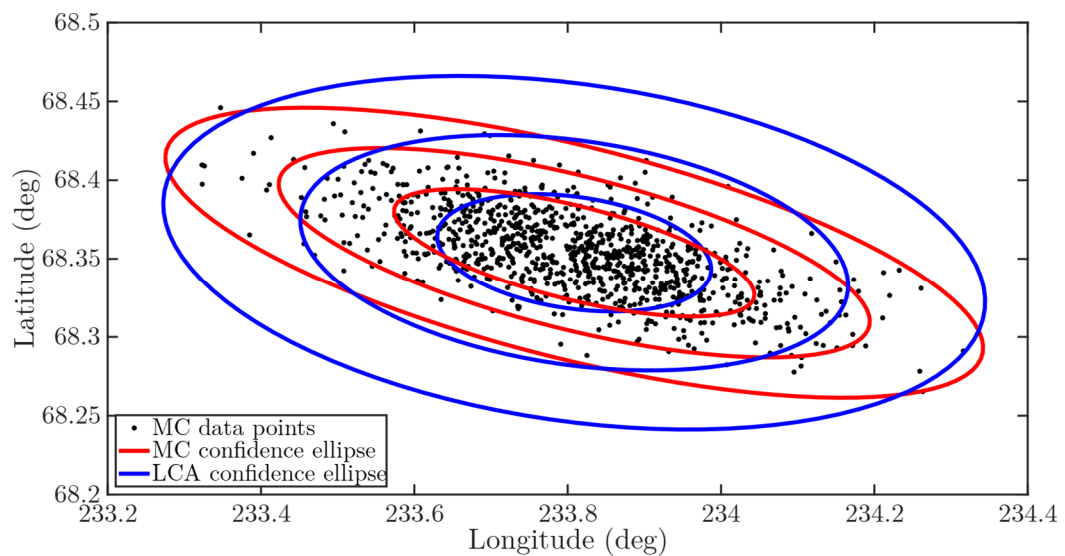


figure 7-4: Points on the trajectory of LCA and MC at lander separation (388 seconds).

Black: Monte Carlo data points. Red: 1, 2 and 3-sigma Monte Carlo confidence ellipses.  
Blue: 1, 2 and 3-sigma LCA confidence ellipses.

## 7.2 MarsGRAM with vertical perturbations

Section 6.1 characterizes the influences on the Monte Carlo simulation depending on the vertical wind perturbations. The MC results with vertical perturbations are overlaid with the respective LCA (see figure 7-5) and analyzed in detail.

In general, the results of this simulation are satisfactory as well, except for a few parts. One decisive difference is the inaccuracy of the radius dispersion which spreads to more than double of the maximum MC runs. In contrast, the LCA is more accurate for the latitude and longitude dispersions in the latter part of the simulation. However, while for example the latitude dispersions stay relatively constant after parachute deployment, the LCA dispersions also go up in this simulation – delivering the same results as in the simulation without vertical wind perturbations. The remaining three spacecraft state dispersions deliver good results given the already discussed circumstances (e.g. parachute opening delay).

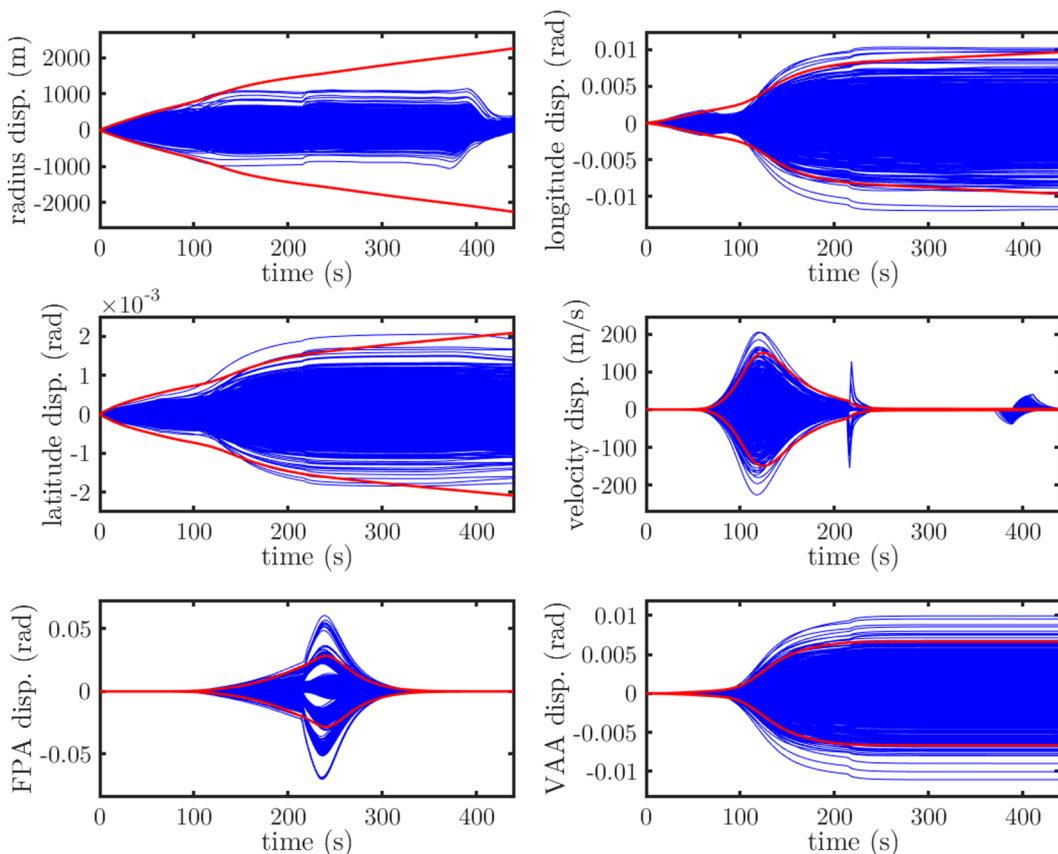


figure 7-5: MarsGRAM with vertical perturbations LCA results superimposed with Monte Carlo runs.

Red: LCA. Blue: MC runs.

In figure 7-6, the covariance confidence ellipses are shown in comparison with the Monte Carlo confidence ellipses. While the maximum and minimum latitude data points are indeed close the respective points in the three-sigma covariance ellipse, the shape is similar to the ellipses without vertical wind perturbations. Consequently, the dispersions are overestimated in the direction of the semi-minor axis.

The data in figure 7-7 shows, that the results of the LCA confidence ellipse are – similar to the simulation without vertical wind perturbations - a much better fit at the end of the re-entry phase. For this reason, the LCA results for the MarsGRAM database are found to be satisfactory for the complete simulation and excellent for the re-entry phase.

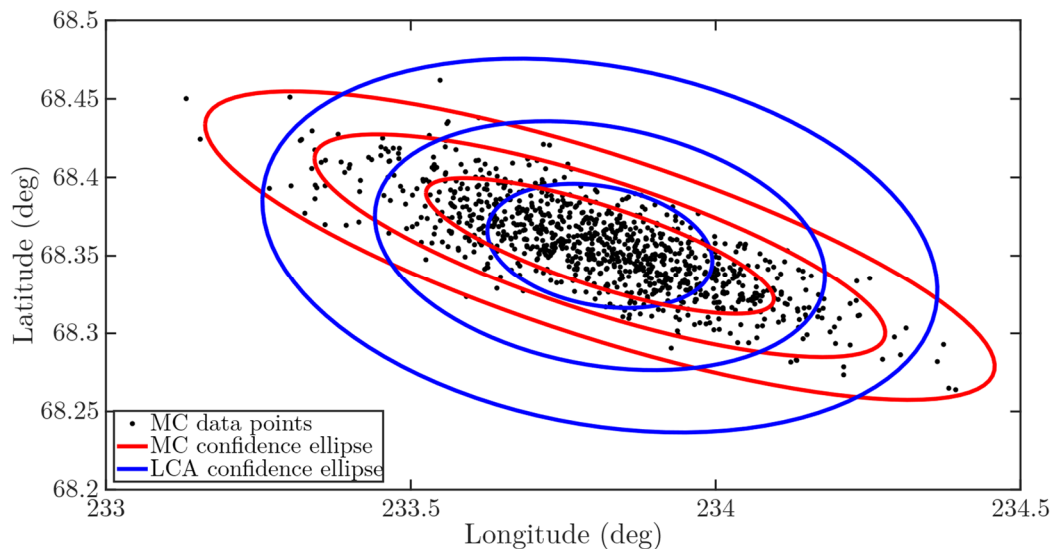


figure 7-6: Surface landing points of MarsGRAM LCA and MC with vertical perturbations.

Black: Monte Carlo data points. Red: 1, 2 and 3-sigma Monte Carlo confidence ellipses.  
Blue: 1, 2 and 3-sigma LCA confidence ellipses.

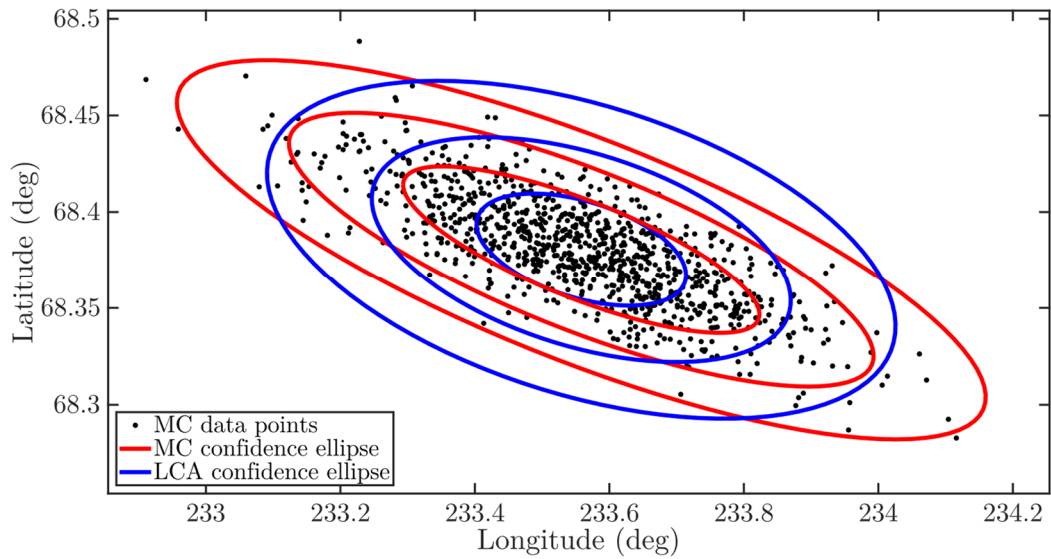


figure 7-7: Points on the trajectory of MarsGRAM LCA and MC with vertical perturbations at 215 seconds.

Black: Monte Carlo data points. Red: 1, 2 and 3-sigma Monte Carlo confidence ellipses.  
Blue: 1, 2 and 3-sigma LCA confidence ellipses.

### 7.3 MCD

As per the analysis in chapter 6, the state dispersions for MCD are unlike MarsGRAM's, mainly in size but also in shape. The LCA results for the MCD database therefore have to be analyzed separately. As mentioned before, the MCD does merely work without the vertical wind perturbations due to the limitations of the web-based client.

First of all, the radius dispersions fit well with the majority of the simulation. Because of the higher cut-off altitude, the decline in deviations at the end is not as clearly visible but can only be suspected from the negative part of the graph. However, the LCA for MCD is likewise not capable of following that path.

While the longitude fit is nearly perfect over the whole course of the simulation, the match for the latitude dispersion is opposite to MarsGRAM. In this case, the LCA does not divert from the Monte Carlo runs but instead underestimates the discrepancies.

The remaining three parameters – velocity, flight-path angle and velocity azimuth angle – are all a good match considering the previously analyzed effects (e.g. parachute deployment time).

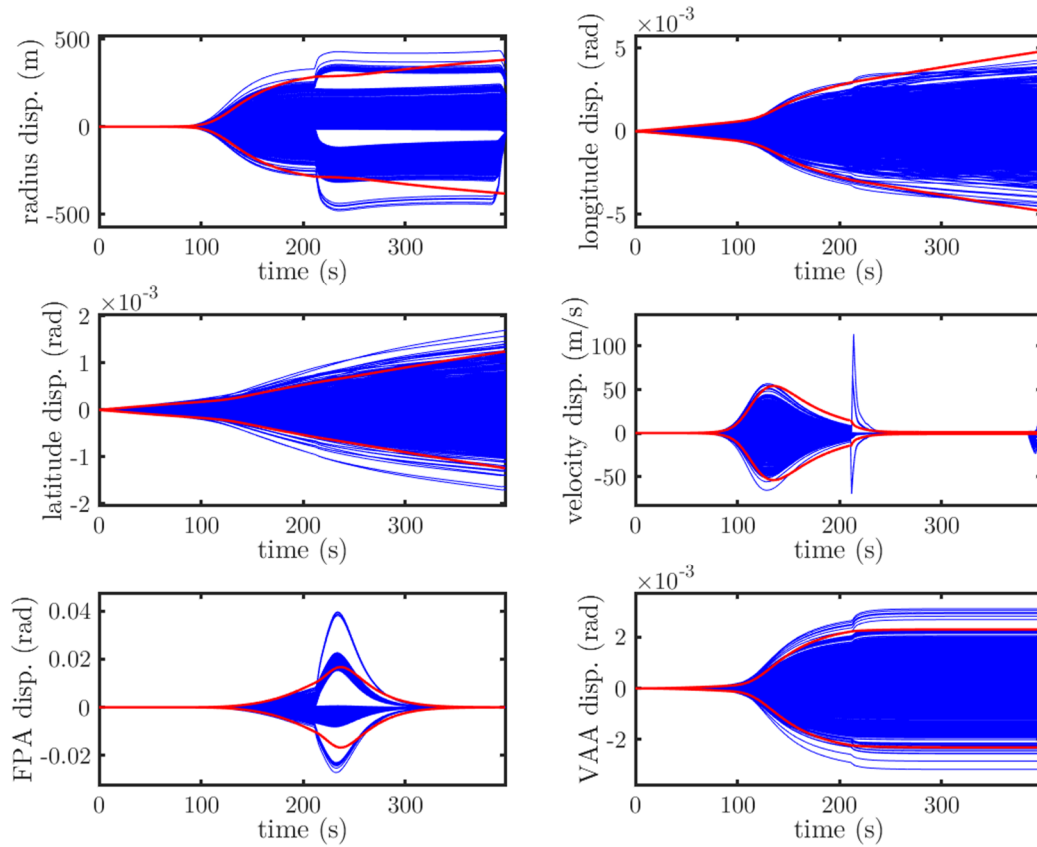


figure 7-8: MCD without vertical perturbations LCA results superimposed with Monte Carlo runs.

Red: LCA. Blue: MC runs.

The display of the confidence ellipses in figure 7-9 show the effects analyzed above. The LCA ellipses are smaller in the direction of the semi-minor axis, whereas the longitudinal fit is nearly perfect.

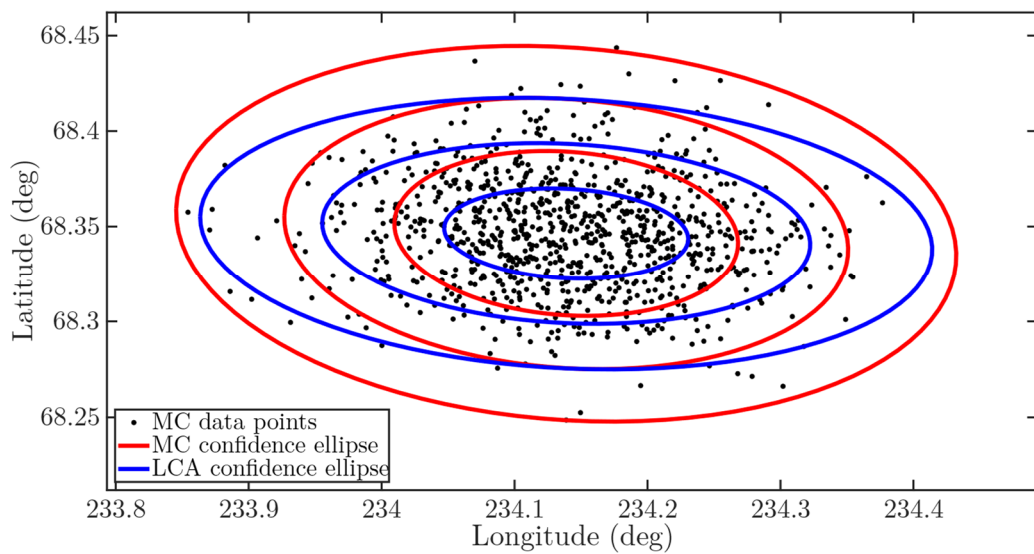


figure 7-9: Surface landing points of MCD LCA and MC without vertical perturbations. Black: Monte Carlo data points. Red: 1, 2 and 3-sigma Monte Carlo confidence ellipses. Blue: 1, 2 and 3-sigma LCA confidence ellipses.

## 7.4 Components of the LCA

Linear covariance analysis is not only capable of computing the expected dispersion from the nominal trajectory, but it is also capable of identifying the influence of the respective parameters. For this reason, the LCA is performed separately with a single uncertainty parameter at a time. Due to the given constraints, the MarsGRAM results will be analyzed both for ‘with’ and ‘without’ vertical wind perturbations and MCD only for ‘without’.

### MarsGRAM with vertical wind perturbations

figure 7-10 shows the LCA components for MarsGRAM with vertical wind perturbations. The causes for the state parameters vary widely and are analyzed in detail.

The radius dispersion is predominantly influenced by the vertical wind perturbations with the second major influence being density. The horizontal winds do not have any influence. While the vertical winds affect the trajectory during the entire simulation, the density dispersion effect is only apparent between 100 and 200 seconds during the high deceleration phase. However, as analyzed in section 7.2, the radius LCA is not a good fit for this simulation because of a big diversion. This can be attributed to the vertical wind perturbations because of this analysis.



The influence on the longitude and latitude is equally shared by density and horizontal wind. As before, the main impact of the density is during the deceleration phase between 100 and 200 seconds. The uncertainty of the velocity, the flight-path and velocity azimuth angle can predominantly be attributed to the density. Only the VAA is slightly impacted by the horizontal wind perturbations.

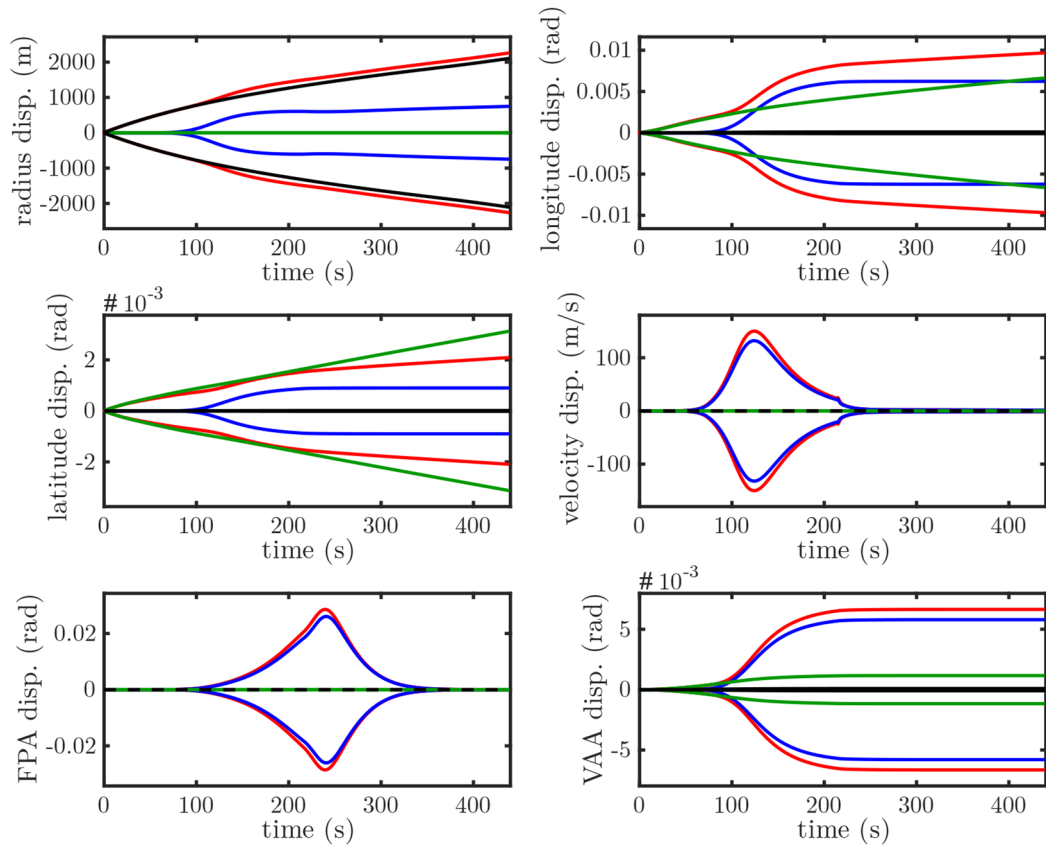


figure 7-10: LCA components MarsGRAM with vertical wind perturbations.

Red: Nominal LCA. Blue: Density LCA. Green: Horizontal wind LCA.

Black: Vertical wind LCA.

### MarsGRAM without vertical wind perturbations

The results for these components are similar (see figure 7-11). The biggest difference can be seen in the radius dispersions. As the vertical wind perturbations are disabled, the only influencing factor is the density uncertainty. This also leads to a significantly better fit to the Monte Carlo simulation (see figure 7-1). The remaining state parameters are similarly influenced by the respective uncertainties.

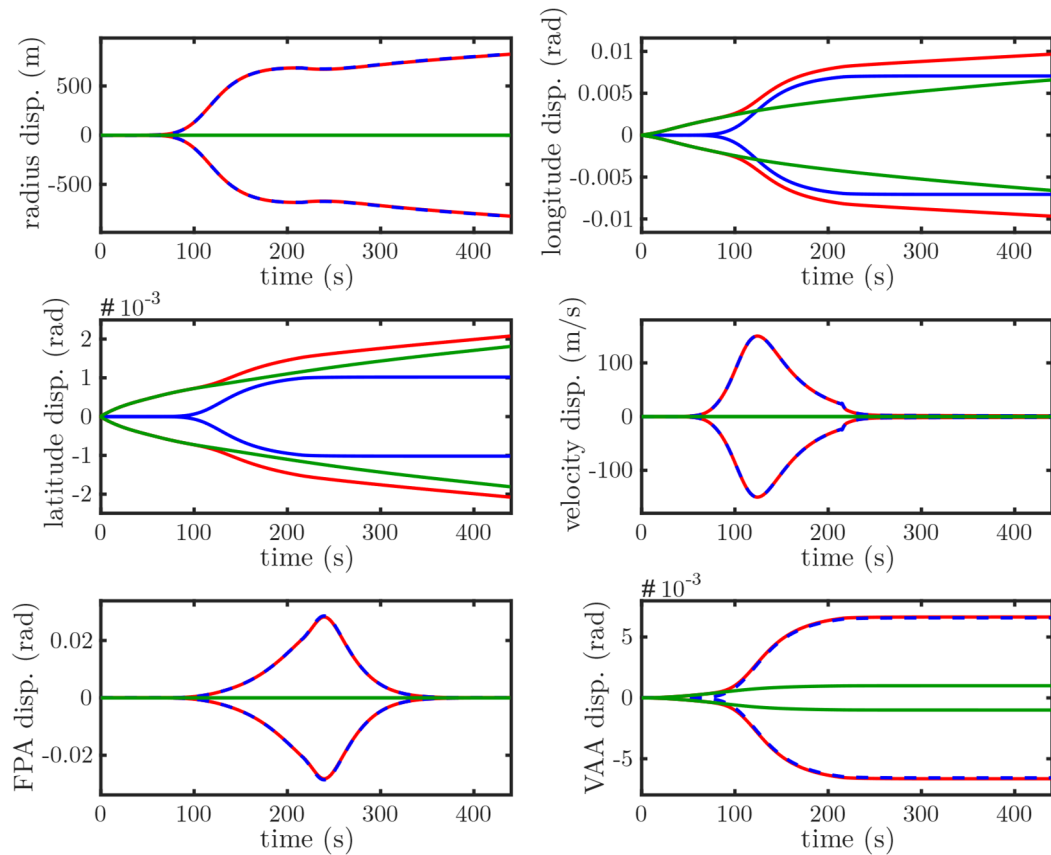


figure 7-11: LCA components MarsGRAM without vertical wind perturbations.  
 Red: Nominal LCA. Blue: Density LCA. Green: Horizontal wind LCA.

### MCD without vertical wind perturbations

For MCD, the results resemble MarsGRAM's without vertical wind perturbations (see figure 7-12). While the radius, velocity, FPA and VAA are predominantly influenced by the density, the longitude and latitude are impacted both by density and horizontal winds.

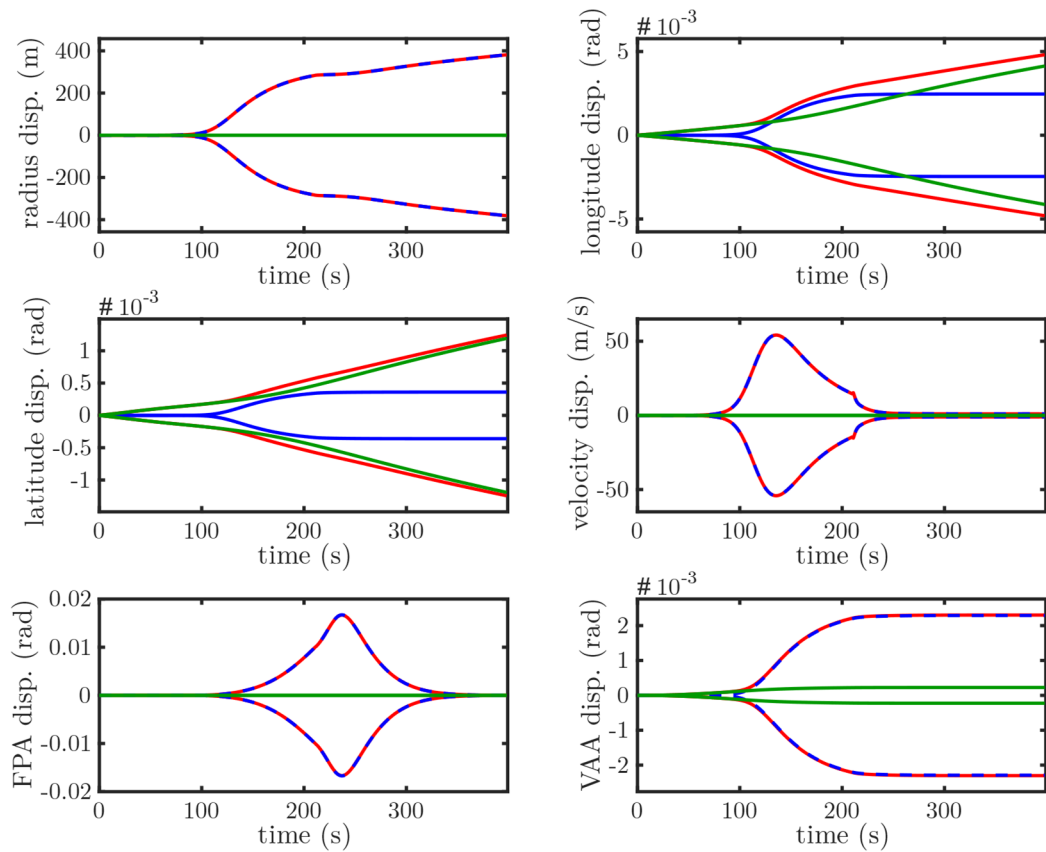


figure 7-12: LCA components MCD without vertical wind perturbations.  
 Red: Nominal LCA. Blue: Density LCA. Green: Horizontal wind LCA.

## 7.5 Choice of integration method

The computation of the linear covariance analysis is based on a differential equation propagation along the nominal trajectory. The matrices in the propagation equations contain many differential equations which have to be solved accordingly. Within the Matlab Simulink environment, it is possible to adjust the differential equation solver. Thus, the impact of changing the solver is investigated below.

A fixed-step or a variable-step solver can be chosen. For the fixed-step solvers, the Runge-Kutta 4 is the standard solver. However, for most problems the accuracy is higher with a variable-step solver. Applicable in this case are ODE45, ODE23 and ODE15. In general, the standard solver is ODE45 which is expected to be the most accurate. In contrast, figure 7-13 and figure 7-14 show that both for MarsGRAM and MCD the highest accuracy is achieved with ODE23 and ODE15, with ODE15 having a slight edge in the latitude dispersion for MarsGRAM. Due to these findings, ODE15 will be the standard solver for all analyses going forward. Although no certain reason can be given, it is presumed that the problem at hand is stiff as ODE15 is generally used for stiff problems.

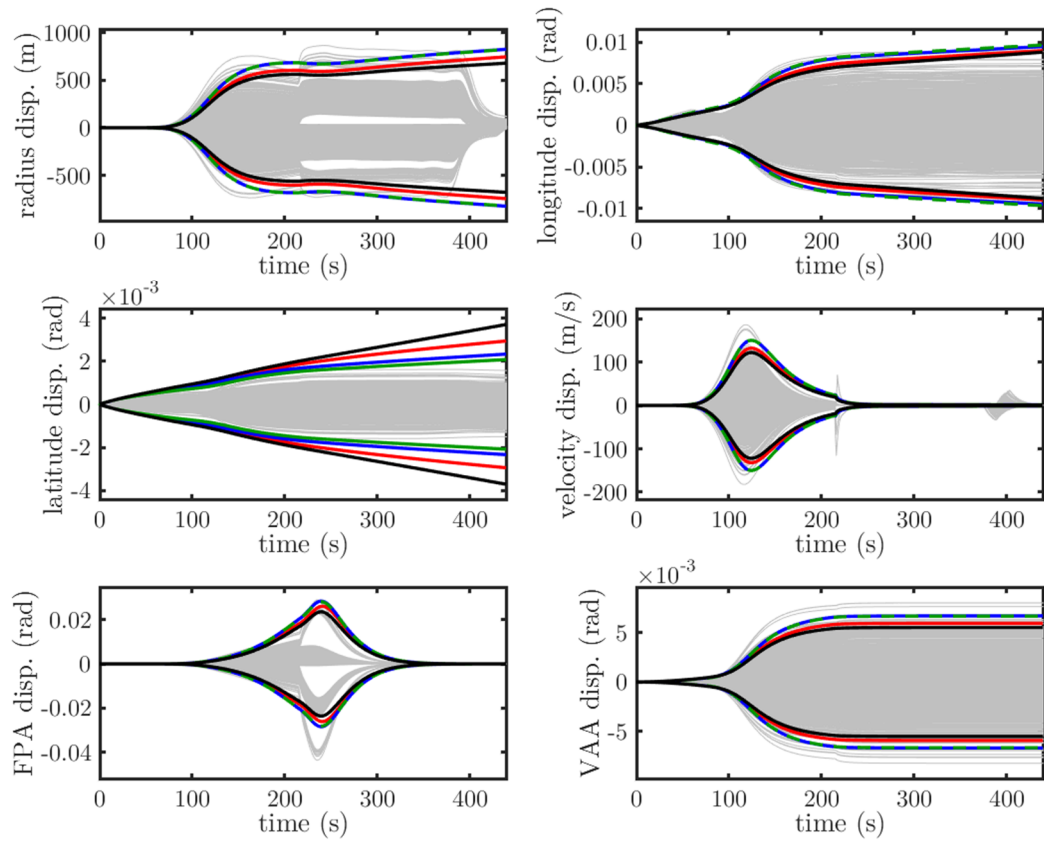


figure 7-13: Comparison of ODE solvers for MarsGRAM Phoenix landing without vertical perturbations.

Grey: Monte Carlo runs. Black: RK4 (1 s). Red: ODE45. Blue: ODE23. Green: ODE15.

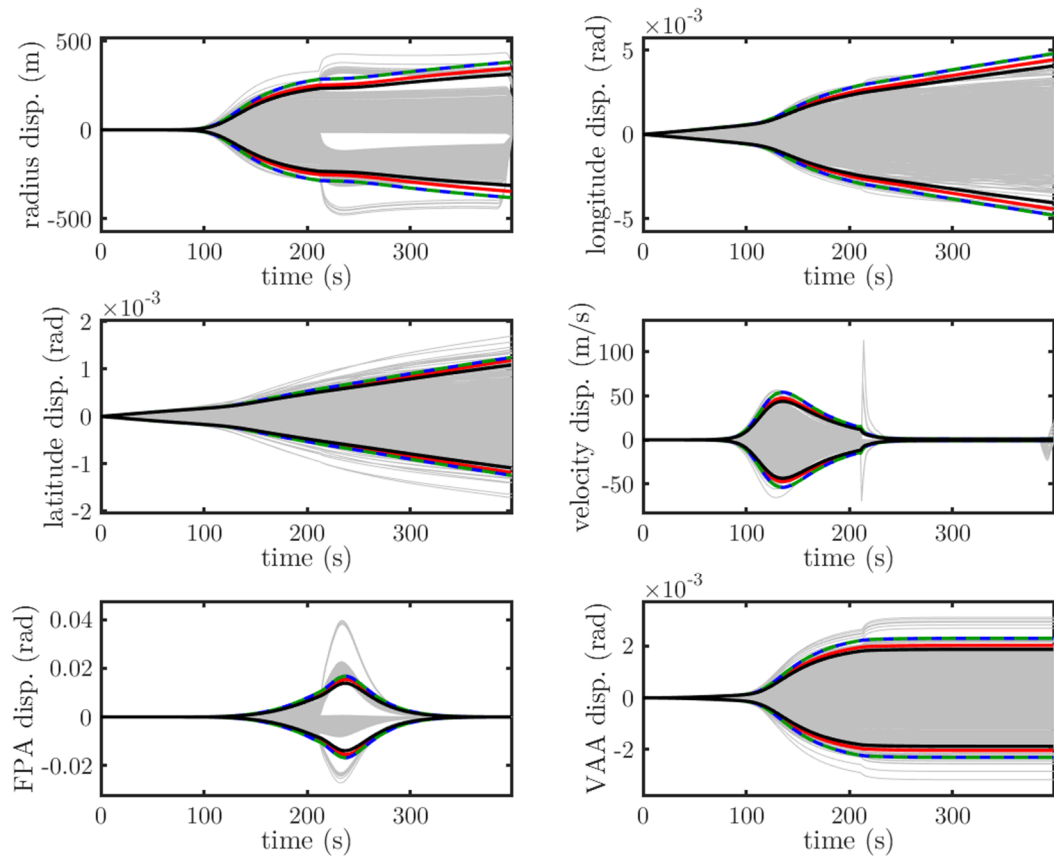


figure 7-14: Comparison of ODE solvers for MCD Phoenix landing without vertical perturbations.

Grey: Monte Carlo runs. Black: RK4 (1 s). Red: ODE45. Blue: ODE23. Green: ODE15.

## 8 Analysis of atmospheric models

After two methodologies for the analysis of trajectory deviations have been established, this chapter studies the impact of the atmosphere itself on the trajectory and their dispersions. Therefore, only the landing points and the three-sigma ellipses of the Monte Carlo method are part of this chapter and vertical wind perturbations are switched off. The analysis includes the modelling year, the seasonal influences and a direct database comparison between MarsGRAM and MCD. Additionally, the impact of mirroring the entry point to the southern hemisphere is inspected. Finally, the spacecraft is changed to the larger Mars Science Laboratory to evaluate the impact of the mass and geometry in identical atmospheric conditions.

### 8.1 Modelling year

Within the databases, it is possible to choose between various modelling years and to customize the model specifically to e.g. increase the dust storm activity. For this study, it is of interest whether the modelling years substantially change the expected landing corridor and the respective landing points.

#### 8.1.1 MarsGRAM

Three MarsGRAM modelling years are analyzed within this study. Firstly, the nominal data are based on a customizable model with average wind, density and dust storm activity. Secondly, the Year-1 model is influenced by and validated against measurements taken between April 1999 and January 2001. Thirdly, the measurements from the Year-2 models are from the February 2001 to December 2002 timeframe. These measurements were conducted with a thermal emission spectrometer by the Mars Global Surveyor (MGS) spacecraft. Density data generated during the aerobrake maneuver of the MGS spacecraft enhance the veracity of the data in the higher atmosphere above 90 kilometers. [10]

The data in figure 8-1 show the landing points of the three modelling years and their associated three-sigma landing ellipses. There are no major differences between the landing ellipses and the overlap between them is significant. However, there is a greater match for Year-1 and Year-2 than there is for the customized average atmosphere. The ellipses for Year-1 and 2 have a longer semi-minor axis.

The most probable explanation for the discrepancies is a stronger horizontal wind (including higher uncertainties) from the west with a slight northern component which pushes the spacecraft landing point further east. Furthermore, a growth in uncertainty leads to a broader spread of the landing points.

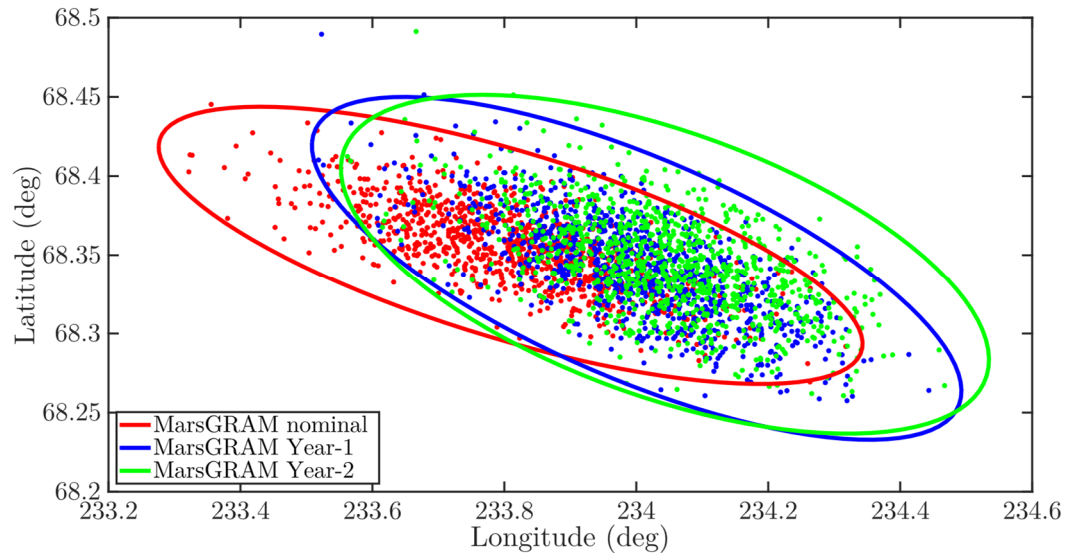


figure 8-1: Surface landing points and 3-sigma landing ellipses of different MarsGRAM modelling years.

Red: MarsGRAM nominal. Blue: MarsGRAM Year-1. Green: MarsGRAM Year-2.

### 8.1.2 MCD

The MCD database includes several modelling scenarios. To begin with, an average, minimum and maximum year regarding climatology and dust storm activity can be chosen. Afterwards, a best fit scenario for the real Mars years 24 to 32 is available. In accordance with the MarsGRAM comparison, three modelling scenarios are chosen. The nominal scenario is the average climatology and solar activity model. As the Phoenix lander touched down during Mars year 29, it is chosen as the second option. Finally, Mars year 31 is picked for crosschecking.

In comparison with the results for MarsGRAM, the data in figure 8-2 shows better conformity. The ellipse shape for the nominal case and Mars year 31 are basically equal. In contrast, the ellipse for Mars year 29 has the same orientation but is smaller. Consequently, the standard-deviation of the data is smaller.



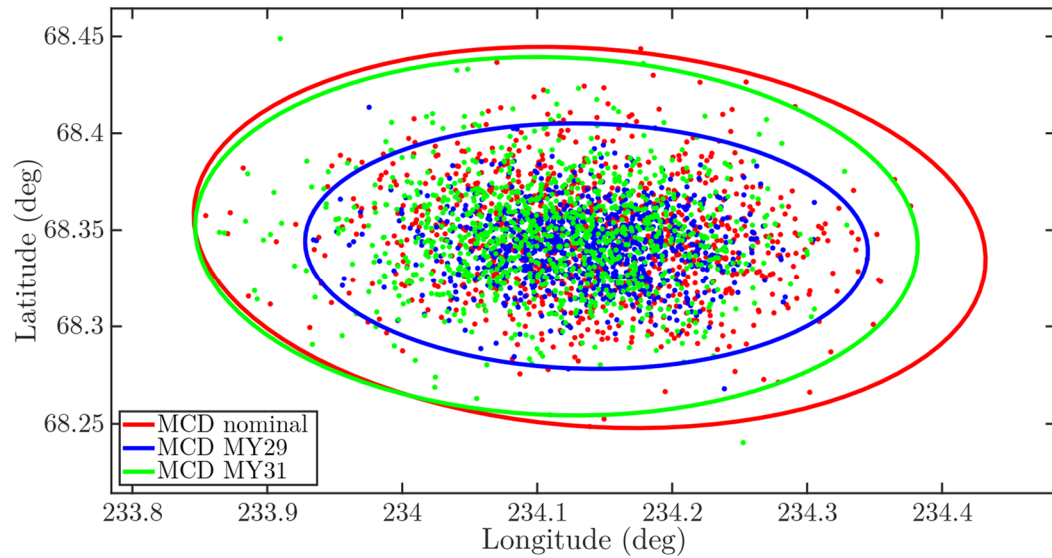


figure 8-2: Surface landing points and 3-sigma landing ellipses of different MCD modelling years.

Red: MCD nominal/average solar. Blue: MCD Mars Year 29. Green: MCD Mars Year 31.

## 8.2 Seasonal influence

The analysis of the atmosphere in section 2.1 shows a high variation in the properties of the atmosphere depending on the time of year. As a consequence, the atmospheric study shall examine the impact on the landing points of the spacecraft. The atmospheric conditions in this section are based on the average atmosphere settings.

### 8.2.1 MarsGRAM

The landing data shown in figure 8-3 display significant differences in the position of the landing points and the shape of the three-sigma ellipses.

A distinct yearly pattern for the landing points is identified which can be attributed to density variations. The nominal Phoenix entry date coincides with late spring. Thus, the high density during the summer months leads to an entry profile with a higher deceleration curve. A quarter of a year later in late summer, the major effects of the long summer in the northern hemisphere have already subsided and the landing ellipse is positioned further to the south-east. The low density during autumn and winter are exposed by the ellipses of one-half and three-quarters of the year which are located the outermost to the south-east. As a countercheck, the 1-year data shows approximate repetition of the pattern.

The second effect identified in the data is the impact of the horizontal wind. The westerly winds as predominant winds in the in-flight direction are higher in autumn and winter, enlarging the effect of the landing point push to the south-east. During summer, easterly winds are prevailing.

In contrast, the crosswind varies without an apparent pattern. As an example, while the cross wind is high for the half-year mark resulting in a broad ellipse, it is not for the three-quarter-year point which has a shallow ellipse. Additionally, the control comparison of the Phoenix landing one Mars year later shows that the crosswinds cannot be determined for a specific solar longitude.

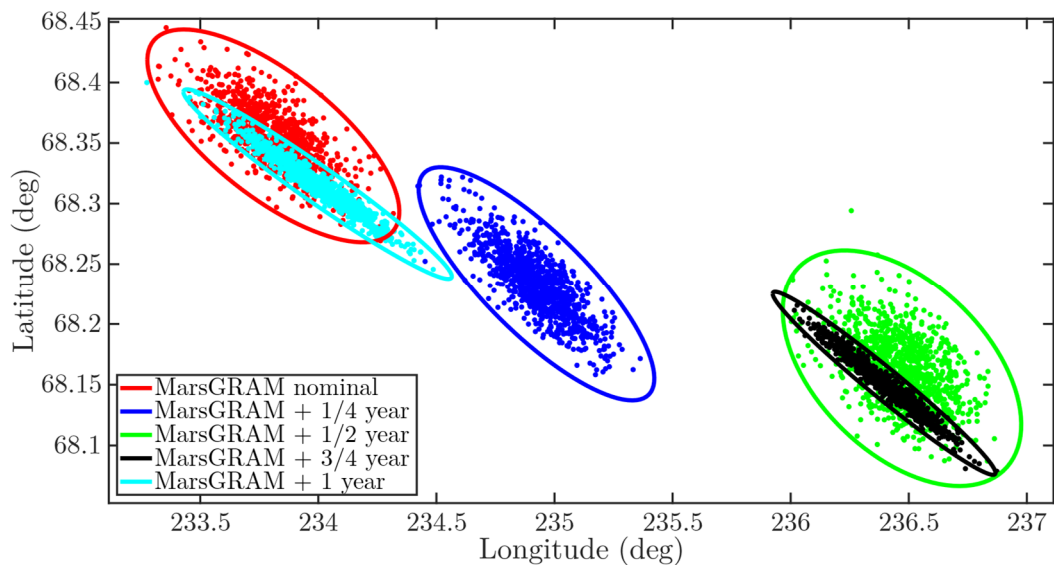


figure 8-3: Surface landing points and 3-sigma ellipses of different dates for a year on Mars with MarsGRAM.

Red: nominal date ( $L_s = 76.6^\circ$ ). Blue:  $+1/4$  year ( $L_s = 157.2^\circ$ ). Green:  $+1/2$  year ( $L_s = 258.9^\circ$ ). Black:  $+3/4$  year ( $L_s = 358.1^\circ$ ). Cyan:  $+1$  year.

### 8.2.2 MCD

Applying the same method to MCD, the results can be found in figure 8-4. In general, the seasonal pattern identified for MarsGRAM is similar for MCD with a few key distinctions. The quarter-year ellipse is closer to the results of the half- and three-quarter-year ellipses. Furthermore, they extend further to the south and the east. The extension to the east is predominantly caused by the increased spread for the landing ellipses which will be further discussed in section 8.2.3.

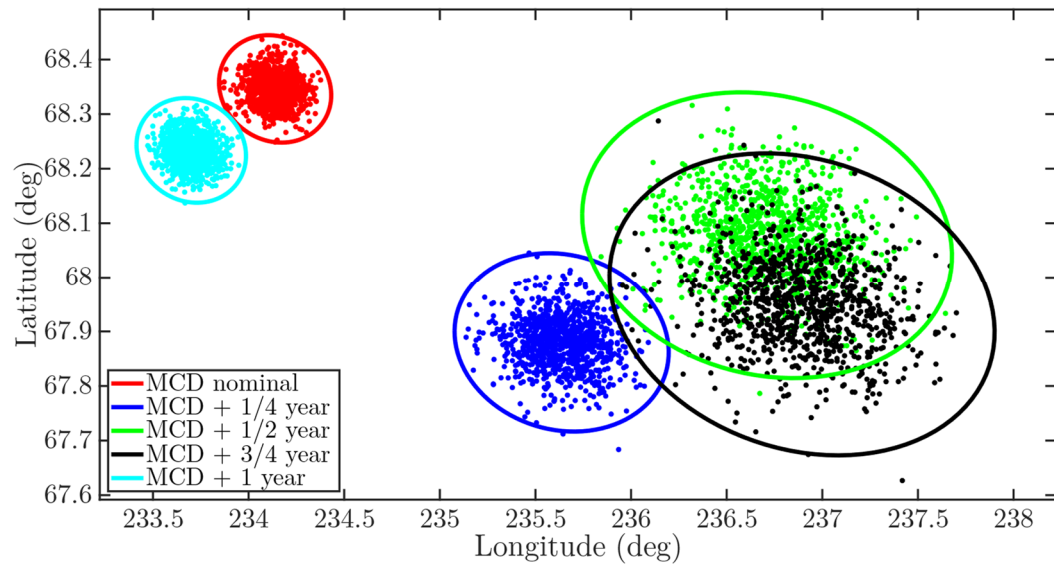


figure 8-4: Surface landing points and 3-sigma ellipses of different dates for a year on Mars with MCD.

Red: nominal date ( $L_s = 76.6^\circ$ ). Blue:  $+1/4$  year ( $L_s = 157.2^\circ$ ). Green:  $+1/2$  year ( $L_s = 258.9^\circ$ ). Black:  $+3/4$  year ( $L_s = 358.1^\circ$ ). Cyan: +1 year.

### 8.2.3 Database comparison

figure 8-5 through figure 8-9 display the direct comparisons between the MarsGRAM and MCD databases for each point in time in the seasonal analysis. Generally, the results vary significantly and there is no recognizable pattern. As an example, the ellipses for the nominal landing (see figure 8-5) overlap partly and have approximately the same magnitude in covered area while a quarter of a year later (see figure 8-6) the ellipses are completely separated from each other. Furthermore, the MarsGRAM ellipse from half a year later (see figure 8-7) is enclosed in the one created with MCD and only covers an area of about 15-20 percent of MCD's. This finding is even more pronounced in the three-quarter year comparison (see figure 8-8) where the MarsGRAM ellipse only partly overlaps with MCD and covers approximately less than five percent of the other ellipse due to its shallow shape, possibly originating from sparsely experienced cross winds.

These outcomes show that there are significant differences in the magnitudes of the atmospheric parameters (density and wind) modelled in the databases. Also, the uncertainties are of dissimilar sizes resulting in significantly diverse landing position deviations for the two simulation frames.

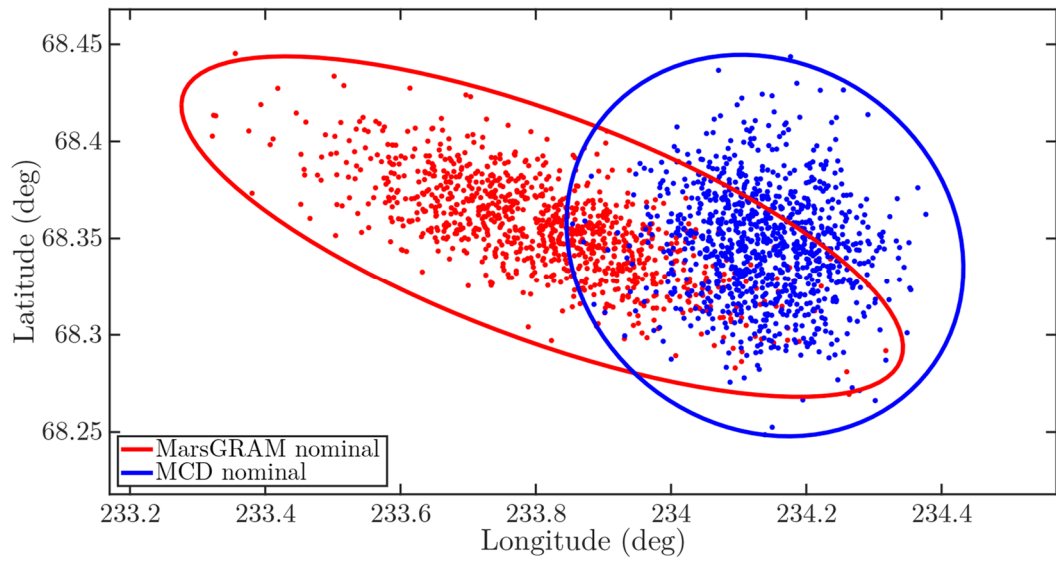


figure 8-5: Comparison of surface landing points and ellipses for nominal Phoenix landing using the MarsGRAM and MCD databases.

Red: MarsGRAM. Blue: MCD.

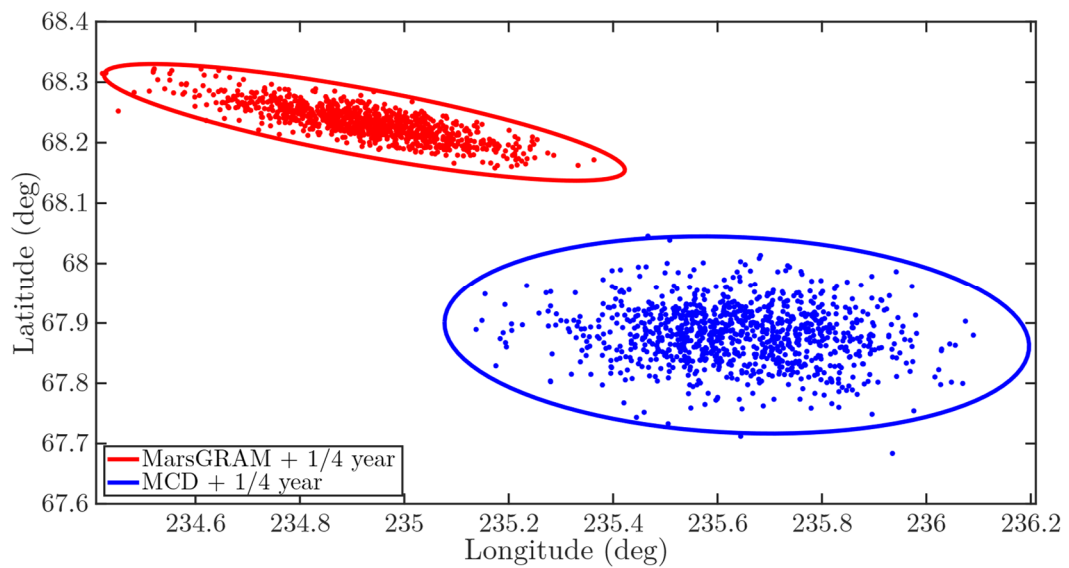


figure 8-6: Comparison of surface landing points and ellipses for the Phoenix landing + 1/4 year using the MarsGRAM and MCD databases.

Red: MarsGRAM. Blue: MCD.

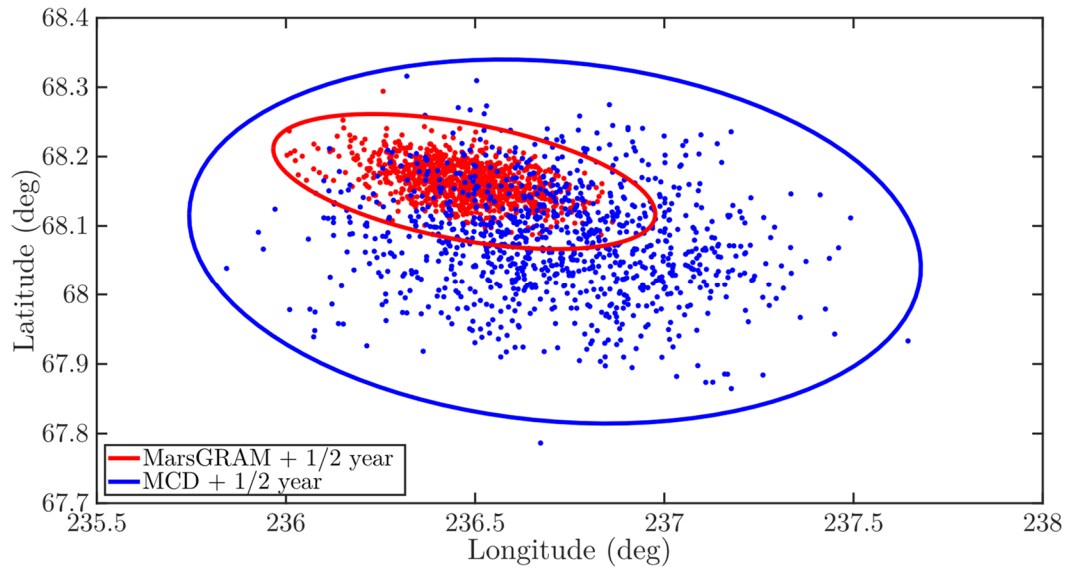


figure 8-7: Comparison of surface landing points and ellipses for the Phoenix landing +  $\frac{1}{2}$  year using the MarsGRAM and MCD databases.  
Red: MarsGRAM. Blue: MCD.

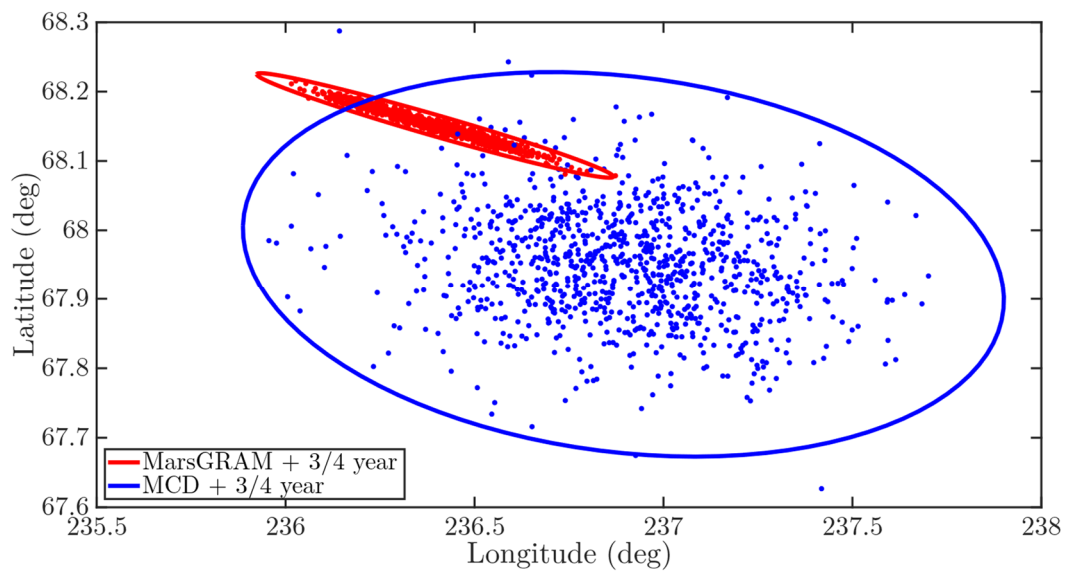


figure 8-8: Comparison of surface landing points and ellipses for the Phoenix landing +  $\frac{3}{4}$  year using the MarsGRAM and MCD databases.  
Red: MarsGRAM. Blue: MCD.

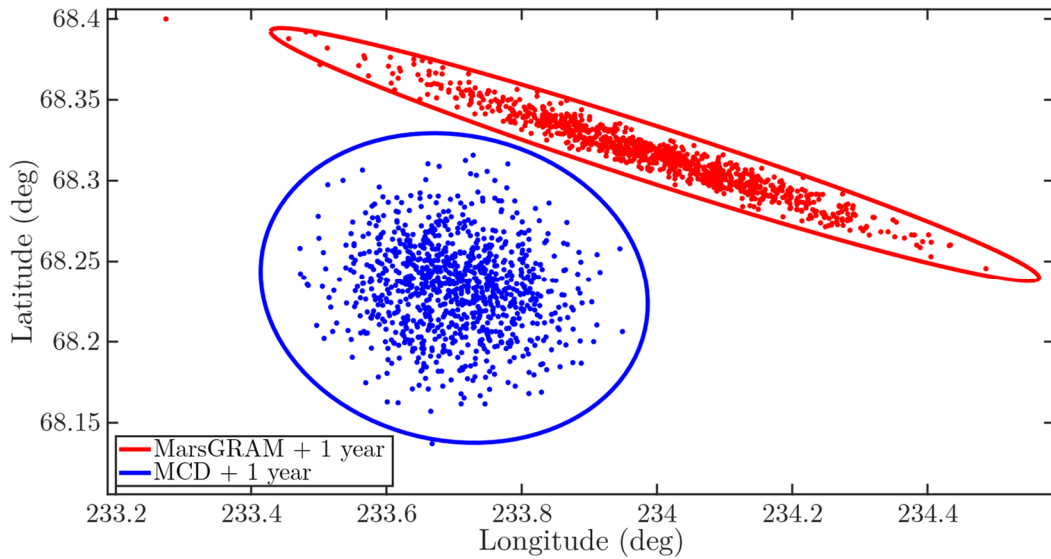


figure 8-9: Comparison of surface landing points and ellipses for the Phoenix landing + 1 year using the MarsGRAM and MCD databases.  
Red: MarsGRAM. Blue: MCD.

### 8.3 Landing on the southern hemisphere

The orbit-planet synergy formulated in section 2.1 leads to different climates in the northern and southern hemisphere. Additionally, the surface altitude relative to the MOLA geoid is significantly higher on the southern half of the planet. In order to analyze the effects of these differences, an entry analysis of the Phoenix landing with the latitude and VAA mirrored along the equator is performed. Because of the expectable similarity of the result, this analysis is performed with the MarsGRAM database. The altered initial conditions are (see table 4-1 for the rest):

$$\begin{aligned}\phi &= -69.363798394042846^\circ \\ \psi &= 90^\circ + (90^\circ - 77.701926824525046^\circ) \\ &= 102.2980731754750^\circ\end{aligned}$$

At first, the difference in surface altitude can be seen in figure 8-10. While the spacecraft on the northern hemisphere has a comfortable altitude of 12-13 kilometers at parachute deployment, this value decreases to approximately four kilometers for the southern hemisphere. After parachute deployment, the spacecraft still needs to decelerate substantially, release the backshell, turn on the thrusters and land on the surface. If the parachute is opened this close to the surface, the schedule for these actions is tight and the probability of a mishap, which could lead to a mission failure, increases considerably. This is the reason why the majority of

Mars missions are planned for lower elevations. The highest successful landing to date is the Opportunity rover at a MOLA altitude of -1.44 kilometers [30].

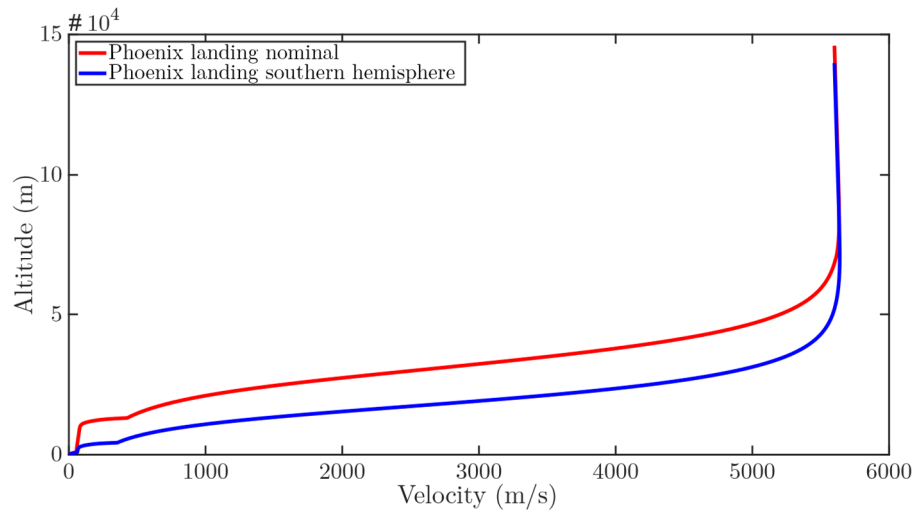


figure 8-10: Velocity-altitude comparison of nominal Phoenix landing and mirrored on the southern hemisphere.

Red: Phoenix landing nominal. Blue: Phoenix landing southern hemisphere.

Apart from the trajectory change in relation to the surface, the impact of the atmosphere is also of interest. The data in figure 8-11 shows the results of a quarterly Monte Carlo analysis. There is a clear seasonal pattern which is reversed in comparison with the northern hemisphere (see figure 8-3). In this case, the ‘nominal’-timeslot is in winter which results in a landing site further to the north-east due to lower density values and the present westerly winds. Half a year later, it is summer on the southern hemisphere which is why its landing ellipse is further west.

Because of the elliptic orbit of Mars, winter in the southern hemisphere is longer than in the North. Consequently, the center of the landing ellipse a quarter of a year later is not much different than in the nominal case. The position of the landing ellipse does not change until the beginning of a short, but intensive, summer half a year later. After three-quarters of the year, the landing ellipse is already close to the winter position.

The high seasonal differences in the south lead to higher spatial distances between winter and summer. The landing ellipse centers have a maximum longitudinal difference of about 3.75 degrees, while it is 2.75 degrees in the northern hemisphere.

Furthermore, the latitudinal difference is approximately 0.5 degrees in comparison to 0.2 degrees.

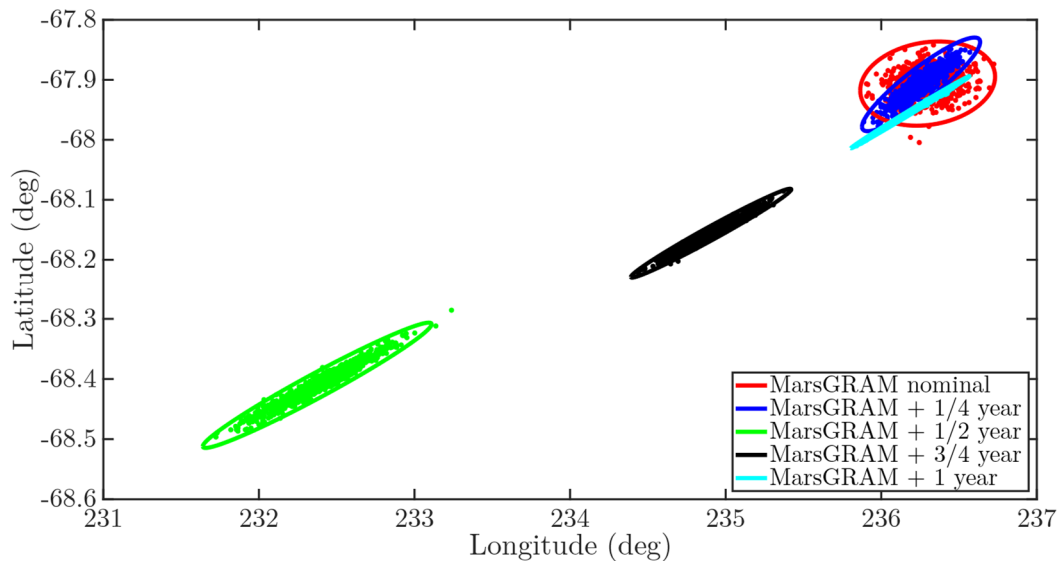


figure 8-11: Surface landing points and 3-sigma ellipses of different dates for a year on Mars with MarsGRAM on the southern hemisphere.

Red: nominal date ( $L_s = 76.6^\circ$ ). Blue:  $+1/4$  year ( $L_s = 157.2^\circ$ ). Green:  $+1/2$  year ( $L_s = 258.9^\circ$ ). Black:  $+3/4$  year ( $L_s = 358.1^\circ$ ). Cyan: +1 year.

## 8.4 Case study: Mars Science Laboratory

After analyzing the trajectories of the Phoenix spacecraft encountering various atmospheric conditions, a final case study will be performed. The question arises how much the mass and geometry of the spacecraft impacts the entry trajectory. Therefore, the simulation is adapted to the Mars Science Laboratory (MSL). It is the spacecraft which delivered the Curiosity rover to the surface of Mars.

The MSL spacecraft's properties are shown in table 8-1 in which they are compared to the values of the Phoenix lander. In general, the spacecraft's geometry is similar with a 70-degree sphere-cone aeroshell. However, MSL possesses six balance masses which are discarded shortly before parachute deployment. These are used to trim the spacecraft to a high angle of attack during entry which is changed to neutral for the descent phase. However, the control of the AoA will not be modelled to be able to achieve comparability with the Phoenix system. If the AoA was modelled, the results would not necessarily show the atmospheric impact by changing the mass and geometry but instead the influence of the lifted trajectory. [31]



Furthermore, the landing phase is performed differently. While the propulsion system of the Phoenix lander is integrated into the system, MSL utilizes the so-called sky crane. The sky crane performs all maneuvers regarding propulsion and attitude control. Once the system is close to the ground, the Curiosity rover is rappelled 7.5 meters below the sky crane and gently placed on the surface. Once the rover is stable, the cords are cut and the sky crane uses its remaining fuel to fly away to avoid crashing into the rover. This system requires a significantly higher mass which is why the entry mass is also higher. [31]

table 8-1: Adjusted MSL properties in comparison to Phoenix

Property	MSL	Phoenix
<b>Entry mass</b>	3300 kg [31]	582 kg
<b>Heat shield mass</b>	382 kg [32]	62 kg
<b>Backshell mass</b>	349 kg [32]	110 kg
<b>Balance masses</b>	6 x 25 kg [31]	N/A
<b>Parachute diameter</b>	15.545 m [31]	11.73 m
<b>Spacecraft reference area</b>	15.90 m <sup>2</sup> [31]	5.5155 m <sup>2</sup>
<b>Aerodynamic coefficients</b>	70° sphere-cone shell - similar	
<b>Parachute drag coefficient</b>	Disk-gap-band parachute - similar	
<b>Backshell separation altitude</b>	1600 m [31]	940 m
<b>Thruster specific impulse</b>	222 s [33]	230 s
<b>Thruster force</b>	8 x 3300 N [31]	12 x 293 N
<b>Thruster PI-controls</b>	P: 420 I: 3.2	P: 70 I: 3.2

The results of a Monte Carlo simulation with the MSL spacecraft in comparison to the nominal Phoenix landing is displayed in figure 8-12. Due to the flight path towards the south-east in the latter part of the trajectory, the MSL is found to land further downwind. The high mass results in a delayed deceleration curve as it requires a higher density to achieve notable acceleration values. Subsequently, the

spacecraft remains at higher velocities for a longer time while it dives into the lower parts of the atmosphere. This is supported by the diagrams shown in figure 8-13.

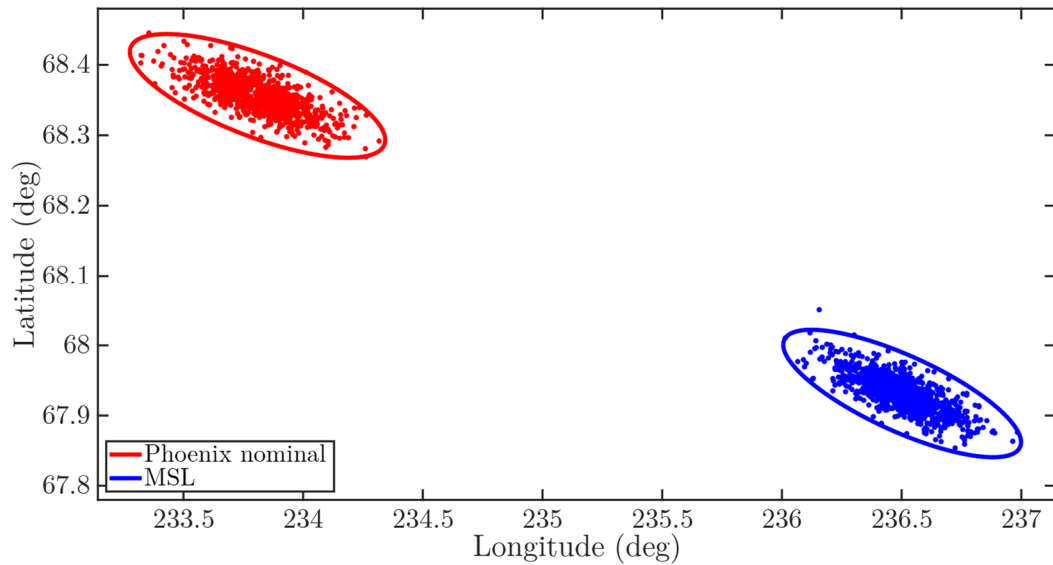


figure 8-12: Comparison of Monte Carlo surface landing points and ellipses for the Phoenix and the MSL landing.

Red: Phoenix landing. Blue: MSL landing.

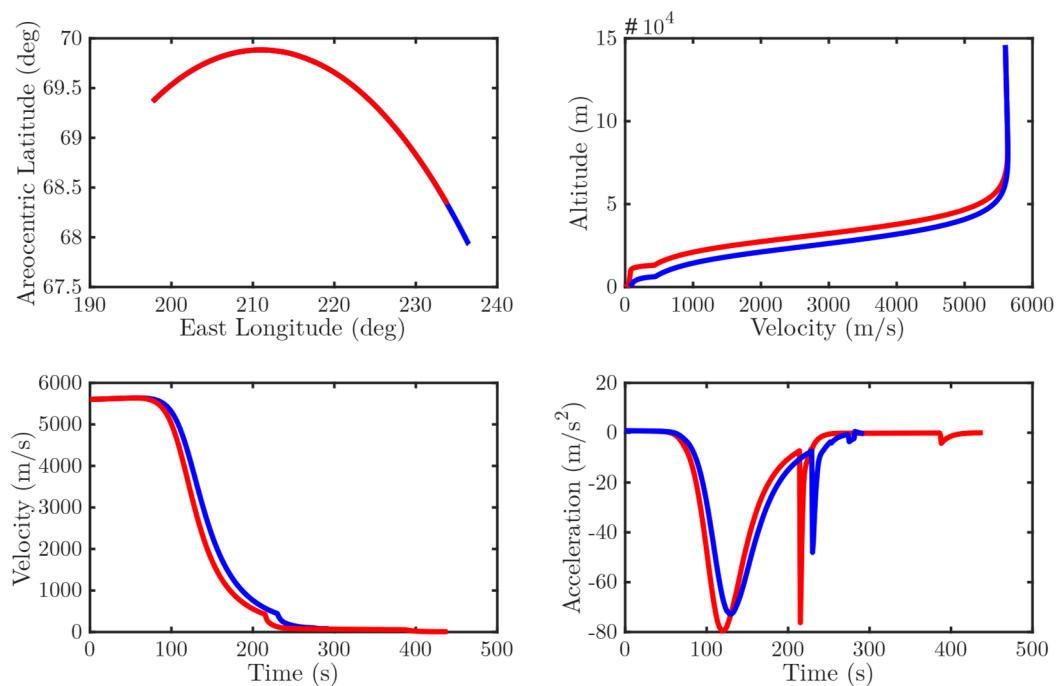


figure 8-13: Various diagrams comparing Phoenix landing to MSL landing.

Red: Phoenix landing. Blue: MSL landing.

## 9 Evaluation

The statistical analysis of the atmospheric models of Mars is the prime objective of this work. In order to pursue this objective, Monte Carlo and linear covariance analysis techniques are performed on a re-entry simulation frame. This chapter evaluates the results originating from these analyses.

The foundation of the overall analysis is the simulation program computing the re-entry trajectory from the initial conditions until touchdown on the surface. During the flight, major milestones like parachute deployment and lander separation are performed. Comparing the data with the Phoenix flight indicates good agreement between real-world data and the simulation. Subsequently, the simulation is validated and able to execute further statistical analyses.

Monte Carlo analysis is used as the basic starting point for the statistical analysis. Its simple implementation and robust results provide the required foundation for the more complex linear covariance analysis. Monte Carlo identifies the deviations from the nominal trajectory imposed by the uncertainties. When comparing the two atmospheric models, it becomes clear that they show discrepancies. Generally, the MCD dispersions for radius, longitude, velocity, flight-path angle and velocity azimuth angle are about half of MarsGRAM's, while the latitudinal deviations are roughly equal.

Because Monte Carlo analysis is very computing resources intensive, linear covariance analysis is brought up as an alternative approach as it merely requires a fraction of the resources. The comparison with Monte Carlo shows that LCA is indeed able to approximate the MC results to a useful degree. While certain aspects like the exact path following of the radius dispersions are difficult, the overall results and especially the landing point accordance are good. In fact, the landing point results are excellent until parachute deployment. From then on, the LCA overestimates the wind deviations.

Analyzing influences on the LCA results, it is found that the choice of integration method does matter. The ODE15 solver provides the best match with the Monte Carlo results. Furthermore, the single aspects of the LCA results are studied. If vertical wind perturbations are switched off, the density is the primary influence

for radius, velocity, flight-path angle and velocity azimuth angle deviations. Including vertical wind perturbations, they have an impact on the radius deviation results. In contrast, latitude and longitude deviations are influenced both by density and wind. While the wind is a continuous influence throughout the trajectory, the impact of the density is only noticeable in the high deceleration phase.

The study of the atmospheric models delivered interesting results as well. While the internal modelling frameworks provide similar results, the seasonal influence on the trajectories is more pronounced. Both MarsGRAM and MCD clearly follow a seasonal pattern based on summer and winter times but also the eccentric orbit of Mars. Because of the higher density and predominant easterly winds in summer, the three-sigma landing ellipse is placed further north-west. In contrast, it is placed further south-east in winter. Comparing the two databases, the size of the landing ellipses is a primary difference. While it is approximately equal in size for some dates, the difference in area can amount to a factor of more than 20.

If the entry point of the trajectory is mirrored to the southern hemisphere, the results are reversed as the seasons. Furthermore, the spatial differences are greater due to the more intense winter and summer seasons in the southern hemisphere. Because of the higher surface elevation in the southern hemisphere, the surface clearance at parachute deployment and during descent is significantly lower. This is the reason why with current technology landing missions are rarely planned for the southern hemisphere.

The last examination is performed by changing the spacecraft from Phoenix to Mars Science Laboratory which is accompanied by a change in geometry and mass. MSL is significantly bigger in size and mass. Due to its mass and inertia, MSL is found to fly further along the trajectory and consequently land downwind. It requires a deeper dive into the atmosphere to build up considerable drag to decelerate the spacecraft. Subsequently, the parachute is also deployed at a lower altitude when compared to Phoenix.

## 10 Conclusion

Because of the low level of knowledge on Mars' atmosphere, re-entry trajectories are subject to uncertainties which are solely based on the atmospheric composition. This work investigated the magnitude of the uncertainties with Monte Carlo and linear covariance analyzed and additionally analyzes the atmosphere and the respective models themselves.

In the beginning, the properties of the atmosphere were outlined, and the two models used within this thesis – MarsGRAM and MCD – were described. A low surface pressure of approximately 0.6 mbar and the atmosphere's primary constituent, carbon dioxide, distinguish Mars' atmosphere from Earth's. Additionally, due to the orbit properties of the planet, seasonal variations are more pronounced. Mars has complex wind systems at all latitudes which can lead to dust storms on a global scale under specific circumstances.

To investigate the atmospheric re-entry, a simulation program was created. It initializes the flight of the Phoenix spacecraft at a pre-defined entry point. The spacecraft dives into the atmosphere and decelerates significantly by creating drag. While still flying supersonic, the parachute is deployed based on an accelerometer measurement. It decelerates the spacecraft even further. At about one kilometer above ground, the program simulates backshell separation and guides the lander to a gentle touchdown with the use of hydrazine thrusters. In order to guarantee its function for later analyses, a thorough validation was performed.

The statistical analysis was based on stochastic fundamentals. Therefore, an introduction to the relevant terms was given. Furthermore, the primary frameworks for Monte Carlo and linear covariance analysis were described. Monte Carlo performed the simulation 1000 times with randomly assigned uncertainty parameters. This process was very resource intensive in terms of computing. In contrast, linear covariance analysis merely required a single simulation and was challenged to approximate the results of Monte Carlo.

Comparing both methods, it became clear that LCA was able to approximate the Monte Carlo results to a satisfactory degree. In fact, the results were excellent until

parachute deployment, after which they deviated. Thus, it was found that LCA can best be used for first assessments where a quick output is required.

The comparison of the atmospheric models on the landing points resulted in various promising outcomes. While there were only small differences in the internal framework of the models themselves, there were distinct differences between them. Given the same input for date and time, the landing points and therefore the confidence ellipses differed to varying degrees – from small location differences to substantial differences in the ellipse size of factor 20 and above. It was found that the differences between the models make a confident re-entry prediction much more difficult as it is not possible to know which one is more accurate.

Furthermore, seasonal influences on the landing location were analyzed. Because of the orbit parameters, the summer months lead to a shorter re-entry trajectory and vice versa. The results were observed to be mirrored on the southern hemisphere because of opposite seasons. In addition, the differences between the landing locations are greater on the southern hemisphere. This can be traced back to the more intense seasons based on the eccentric orbit.

The change from Phoenix to Mars Science Laboratory showed how more mass leads to a further downwind landing. Its inertia lets the spacecraft dive deeper into the atmosphere until sufficient drag is built up to decelerate the spacecraft substantially. Consequently, parachute deployment is performed at lower altitudes as well.

Looking for possible applications in the future, this work could be continued in multiple directions. At first, the Phoenix entry is performed ballistically, meaning without any guidance systems. As the LCA groundwork by Geller is laid out with guidance in mind, a guided entry could be analyzed with a realistic simulation of the Mars Science Laboratory spacecraft. Another direction in which this thesis could be continued, is to adapt it to another extraterrestrial body – for example Venus or Saturn’s moon Titan.

All in all, this work shows that uncertainties in atmospheric models are a major influence on the size and position of the landing ellipse. Because of differences between the model results, precise predictions for real-world re-entries are found to be difficult. Additionally, linear covariance analysis is seen as a good alternative to Monte Carlo methods if time constraints prohibit the use of the latter.

## 11 Bibliography

- [1] W. Herschel, "On the remarkable Appearances at the Polar Regions of the Planet Mars, the Inclination of its Axis, the Position of its Poles, and its spheroidal Figure; with a few hints relating to its real diameter and atmosphere," *Philosophical Transactions of the Royal Society*, 1784.
- [2] P. N. Desai, J. L. Prince, E. M. Queen and et.al., "Entry, Descent, and Landing Performance of the Mars Phoenix Lander," American Institute of Aeronautics and Astronautics, NASA Langley Research Center, Hampton VA and Jet Propulsion Laboratory, Pasadena CA.
- [3] R. M. Haberle, "Planetary Atmospheres: Mars," Elsevier Ltd., NASA Ames Research Center, Mountain View, CA, 2015.
- [4] The Planetary Society, "Mars' Calendar," [Online]. Available: <https://www.planetary.org/explore/space-topics/mars/mars-calendar.html>. [Accessed 26 February 2020].
- [5] NASA, "Mars Climate Modelling Center - General Circulation," 17 April 2020. [Online]. Available: <https://www.nasa.gov/content/general-circulation>. [Accessed 07 June 2020].
- [6] NASA, "Dust Haze Hiding the Martian Surface in 2001," 05 October 2016. [Online]. Available: <https://mars.nasa.gov/resources/8086/dust-haze-hiding-the-martian-surface-in-2001/>. [Accessed 28 April 2020].
- [7] S. R. Lewis, "Modelling the martian atmosphere," *Astronomy and Geophysics*, Volume 44, 2003.
- [8] NASA, "MOLA Precision Experiment Data Record (PDS)," [Online]. Available: <https://nssdc.gsfc.nasa.gov/nmc/dataset/display.action?id=PSPG-00856>. [Accessed 26 February 2020].

- [9] NASA, "Interactive Mars Data Maps," [Online]. Available: <https://marsoweb.nas.nasa.gov/globalData/>. [Accessed 13 March 2020].
- [10] H. L. Justh, "Mars Global Reference Atmospheric Model 2010 Version: User Guide," NASA STI Information Desk, Marshall Space Flight Center, Huntsville AL, 2014.
- [11] E. Millour, F. Forget and S. R. Lewis, "Mars Climate Database v5.3 User Manual," 2017.
- [12] LMD, "Mars Climate Database v5.3: The Web Interface," [Online]. Available: [http://www-mars.lmd.jussieu.fr/mcd\\_python/](http://www-mars.lmd.jussieu.fr/mcd_python/). [Accessed 15 April 2020].
- [13] N. X. Vinh, A. Buseman and R. D. Culp, "Hypersonic and Planetary Entry Flight Mechanics," The University of Michigan Press, 1980.
- [14] R. D. Braun and R. M. Manning, "Mars Exploration Entry, Descent, and Landing Challenges," American Institute of Aeronautics and Astronautics, Georgia Institute of Technology, Atlanta GA and Jet Propulsion Laboratory, Pasadena CA, 2007.
- [15] A. A. Dyakonov, C. E. Glass, P. N. Desai and J. W. Van Norman, "Analysis of Effectiveness of Phoenix Entry Reaction Control System," American Institute of Aeronautics and Astronautics, 2008.
- [16] K. T. Edquist, P. N. Desai and M. Schoenenberger, "Aerodynamics for the Mars Phoenix Entry Capsule," American Institute of Aeronautics and Astronautics, NASA Langley Research Center, Hampton, Virginia 23681.
- [17] K. Jin, J. Luo and D. Geller, "Development and Validation of Linear Covariance Analysis Tool for Atmospheric Entry," Journal of Spacecraft and Rockets, 2018.
- [18] D. I. Clark and D. C. Tanner, "A Historical Summary of the Design, Development and Analysis of the Disk-Gap-Band Parachute," IEEE, Jet Propulsion Laboratory, CA, 2017.



- [19] M. R. Grover III, B. D. Cichy and P. N. Desai, "Overview of the Phoenix Entry, Descent and Landing System Architecture," American Institute of Aeronautics and Astronautics, NASA Langley Research Center, Hampton VA and Jet Propulsion Laboratory, Pasadena CA.
- [20] J. L. Prince, P. N. Desai, E. M. Queen and M. R. Grover, "Mars Phoenix Entry, Descent, and Landing Simulation Design and Modeling Analysis," American Institute of Aeronautics and Astronautics, NASA Langley Research Center, Hampton VA and Jet Propulsion Laboratory, Pasadena CA, 2008.
- [21] National Aeronautics and Space Administration, "Press Kit - Phoenix Landing - Mission to the Martian Polar North," 2008.
- [22] Aerojet Rocketdyne, "Astronautix," 02 April 2003. [Online]. Available: <http://www.astronautix.com/graphics/m/mr107n.jpg>. [Accessed 10 March 2019].
- [23] National Institute of Standards and Technology - U.S. Department of Commerce, "The International System of Units (SI)," 2019.
- [24] C. G. Justus and R. D. Braun, "Atmospheric Environments for Entry, Descent and Landing (EDL)," NASA Marshall Space Flight Center and Georgia Institute of Technology, 2007.
- [25] NIST, "Fundamental Physics Constants - molar gas constant," [Online]. Available: <https://physics.nist.gov/cgi-bin/cuu/Value?r>. [Accessed 14 March 2020].
- [26] R. C. Blanchard and P. N. Desai, "Mars Phoenix Entry, Descent, and Landing Trajectory and Atmosphere Reconstruction," *Journal of Spacecraft and Rockets*, Vol. 48, 2011.
- [27] E. Behrends, *Elementare Stochastik*, Berlin: Springer Spektrum, 2013.
- [28] Vision Dummy, "How to draw a covariance error ellipse," 03 April 2014. [Online]. Available: <https://www.visiondummy.com/2014/04/draw-error-ellipse-representing-covariance-matrix/>. [Accessed 20 April 2020].

- [29] Technische Universität Bergakademie Freiberg, "Numerik gewöhnlicher Differentialgleichungen - Runge-Kutta-Verfahren," Freiberg.
- [30] NASA, "Sol 1809: "Thread of Life Ledge" at Elevation -4202 Meters", " 06 September 2017. [Online]. Available: <https://mars.nasa.gov/news/2939/sol-1809-thread-of-life-ledge-at-elevation-4202-meters/>. [Accessed 04 April 2020].
- [31] NASA, "Press Kit - Mars Science Laboratory Landing," 2012.
- [32] B. Leitenberger, "Das Mars Science Laboratory (MSL) Curiosity," [Online]. Available: <https://www.bernd-leitenberger.de/msl-curiosity.shtml>. [Accessed 27 April 2020].
- [33] Aerojet Rocketdyne, "In-Space Propulsion Data Sheets," 2020.

---

## 12 Appendices

### 12.1 Generation of atmospheric model point/grid data

To ease the future use of the atmospheric models, the following sections contain step-by-step tutorials on how to use the databases for the utilization within an atmospheric re-entry.

#### 12.1.1 MarsGRAM

The creation of MarsGRAM point and grid data is relatively straight forward and will be explained below. In general, the program is based on executables and text input-files. The main execution file is called '**marsgram\_M10.exe**'. The input is defined in a text file which is formatted as described in the user manual. Pre-formatted examples like '**inputstd0.txt**' can be found in the 'IOfiles'-folder.

Within the text file, the user can choose a variety of parameters which are explained in the user manual and at the bottom of the example files. The primary parameter handles when making no major changes to the standard atmosphere composition are displayed in table 12-1 (if multiple handles are in one table cell, each handle has to be changed separately). The explanations are partly adopted from the user manual [10]. Additionally, the respective data directory has to be determined with the following handles – which only work as an example:

```
DATADIR = 'D:\Mars\Mars2010\Release1.0_Nov10\binFiles\'
```

```
GCMDIR  = 'D:\Mars\Mars2010\Release1.0_Nov10\binFiles\'
```

table 12-1: MarsGRAM parameter handles

Parameter handle	Example value	Explanation
<b>TRAJFL</b>	'null' 'TRAJDATA.txt'	Optional trajectory input file name for grid creation 'null' if not used
<b>IERT</b>	= 1 Earth-Receive time = 0 Mars-event time	Time input definition
<b>IUTC</b>	= 1 UTC time = 0 Terrestrial time	Time input definition
<b>MONTH, MDAY, MYEAR, IHR, IMIN, SEC</b>	Integer values, except seconds 05, 28, 2008, 23, 38, 23.0	Month, Day, Year, Hour of Day, Minute, Second for initial position
<b>NPOS</b>	= 135 = 0 if read from trajectory file	Number of positions evaluated. Not applicable if trajectory grid is input (TRAJFL)
<b>LonEW</b>	= 0 West longitudes positive = 1 East longitudes positive	Define which longitude values are seen as positive (input and output)
<b>NVARX, NVARY</b>	= 1 Planetocentric height above local MOLA areoid (km)	Possibility to plot one (2D) or two (3D) additional parameters. For full list, see user manual page 34
<b>FLAT, FLON, FHGT</b>	25, 0, -5	Initial latitude, longitude and MOLA height. Not applicable if trajectory grid is input (TRAJFL)

<b>DELHGT,</b> <b>DELLAT,</b> <b>DELLON,</b> <b>DELTIME</b>	1, 0, 0, 0	Increment between steps: Height (km), latitude & longitude (deg), time (sec)
--	------------	--

When the program is executed, the name of the input file has to be inserted (e.g.: inputstd0.txt). After successful completion of the program, the following text files will be created:

DayData.txt	Daily averages for heights below 1.26 mbar level
Density.txt	Density average and perturbations
LIST.txt	Non-tabular total data
MarsRad.txt	Radiation parameters
OUTPUT.txt	Most important data
Perturb.txt	Perturbations
ThrmData.txt	Thermospheric parameters for heights above 80 km
TPresHgt.txt	Temperature, pressure and heights
Winds.txt	Winds average and perturbations

The desired data of these tabulated text files is imported into MATLAB and processed within the simulation.

### Point data

For a point data evaluation, no trajectory grid is fed to the simulation and thus all parameters have to be defined in the input file. Below a small example for a vertical profile of the Phoenix landing site (234.248°E, 68.219°N, 28<sup>th</sup> May 2008 23:38:23 MET UTC, altitude -5 to +5 km with 1 km spacing)

TRAJFL	= 'null'	No trajectory input
IERT	= 1	Mars Event Time
IUTC	= 1	UTC time
MONTH	= 5	Month
MDAY	= 25	Day
MYEAR	= 2008	Year
IHR	= 23	Hour
IMIN	= 28	Minute

SEC	= 23.0	Second
NPOS	= 11	11 evaluated positions
LonEW	= 1	East longitudes positive
NVARX	= 1	Additional parameter: MOLA height
NVARY	= 0	Only 2D
FLAT	= 68.219	Initial latitude 68.219° N
FLONG	= 234.248	Initial longitude 234.248° E
FHGT	= -5	Initial altitude -5 km MOLA
DELHGT	= 1	Altitude increment 1 km
DELLAT	= 0	Latitude increment 0 degrees
DELLON	= 0	Longitude increment 0 degrees
DELTIME	= 0	Time increment 0 seconds

### Grid data

For a comprehensive study of the EDL trajectory, it is necessary to create a 3D-grid of the encountered area to be able to provide the simulation with the exact atmospheric conditions. MarsGRAM allows to build such a grid with the program '**bldtraj.exe**' and the required inputs work as follows:

Enter trajectory file name	Phoenix_landing.txt
Enter z1,z2,dz (Real km)	-5, 143, 0.5
Enter lat1,lat2,dlat (Real deg.)	63, 77, 2
Enter lon1,lon2,dlon (Real deg.)	200, 240, 2
Enter time increment (Real sec.)	0

The exemplary data on the right side will create a grid from -5 km to 143 km MOLA altitude with 0.5 km spacing, for latitudes 63° to 77° N with 2° spacing and for longitudes 200° to 240° E with 2° spacing. The time is hold constant at a zero second time increment. Going through all the possible variations, the resulting text file will have 49,896 lines (297x8x21).

#### 12.1.2 MCD

As the MCD database could not be successfully installed on a Windows environment, the web interface is used instead. Unfortunately, it does not offer access to all data which are available in the original database.

The web interface outputs the data in a 35x64 matrix with one parameter being hold constant ( $\rightarrow$  a plane of values). The following shows a Phoenix landing site example:

Latitude '63' degree North

Longitude '200 240' degree East

Altitude '-5000 12000' m below/above MOLA

These inputs will result in a matrix of 35 altitude steps and 64 longitude steps. The finer longitude mesh for MCD is accepted here. The altitude increment of 17,000 meter is chosen to define the delta-altitude between each step to 500 meters. Consequently, to gather the data for e.g. the Phoenix landing site, the following steps have to be followed:

1. First input: '63', '200 240', '-5000 12000'
2. Repeat step 1 with latitudes increments: '65', '67', '69', '71', '73', '75' and '77'
3. Repeat steps 1 and 2 with the altitude increments: '12500 29500', '30000 47000', '47500 64500', '65000 82000', '82500 99500', '100000 117000', '117500 134500' and '135000 152000'

In the end, 72 files should have been created. Once submitting the coordinates, a new tab is opened and a text file of the data can be downloaded with the '**Click here to download an ASCII file containing data**'-button.

With the web version of MCD, four variables can be displayed at once. For the simulation, the following parameters were chosen:

**Download 1:** Density, Density day to day variability, Temperature, Vertical wind

**Download 2:** W-E wind component, S-N wind component, zonal wind day to day variability, meridional wind day to day variability

In the end, this example results in a total of 144 downloaded files. To simplify the import process to MATLAB, it is recommended to name the text files in a way that MATLAB can recognize and loop through all files automatically. For the example at hand, the following naming convention is chosen:

**Download 1:** 'D\_Dv\_T\_vw\_63\_-5.0to12.0.txt'

'D\_Dv\_T\_vw\_65\_-5.0to12.0.txt'

```

. . .
'D_Dv_T_vw_63_12.5to29.5.txt'
. . .
'D_Dv_T_vw_77_135.0to152.0.txt'
Download 2: 'WE_SN_Zov_Mev_63_-5.0to12.0.txt'
               'WE_SN_Zov_Mev_65_-5.0to12.0.txt'
. . .
               'WE_SN_Zov_Mev_63_12.5to29.5.txt'
. . .
               'WE_SN_Zov_Mev_77_135.0to152.0.txt'

```

## 12.2 Detailed interpolation calculation

As the interpolation calculation is an integral part of the whole simulation, it is described in the following with an example (right side) from the MarsGRAM temperature parameters. In the example, the grid has a density of  $2^\circ \times 2^\circ \times 250\text{m}$ , the latitude values range from  $63^\circ \text{ N}$  to  $77^\circ \text{ N}$  (8 values), the longitude values range from  $200^\circ \text{ E}$  to  $240^\circ \text{ E}$  (21 values) and the altitude values range from  $-5 \text{ km}$  to  $143 \text{ km}$  MOLA (593 values):

The input is separated into simulation and MATLAB:

### Simulation input

Longitude $\theta$ (deg)	237.05°
Latitude $\phi$ (deg)	67.29°
MOLA altitude $h$ (km)	-3.358 km

### MATLAB input

$\text{grid} = [\theta \times \phi \times h]$ double	$[21 \times 8 \times 593]$ double
$\text{grid\_size} = [\theta, \phi, h]$	$[21, 8, 593]$
$\text{alt\_input} = [h_{\text{start}}, h_{\text{end}}, h_{\text{gap-loop}}]$	$[-5, 143, 148]$
with $h_{\text{gap-loop}} = h_{\text{end}} - h_{\text{start}}$	$143 - (-5) = 148$
$\text{lon\_input} = [\text{lon}_{\text{start}}, \text{lon}_{\text{end}}, \text{lon}_{\text{gap-loop}}]$	$[200, 240, 40]$
with $\text{lon}_{\text{gap-loop}} = \text{lon}_{\text{end}} - \text{lon}_{\text{start}}$	$240 - 200 = 40$
$\text{lat\_input} = [\text{lat}_{\text{start}}, \text{lat}_{\text{end}}, \text{lat}_{\text{gap-loop}}]$	$[63, 77, 14]$



$$\text{with } \text{lat}_{\text{gap-loop}} = \text{lat}_{\text{end}} - \text{lat}_{\text{start}} \qquad 77 - 63 = 14$$

### Altitude grid calculation

$$\text{grid}_{h,\text{high}} = h_{\text{high}} = \text{ceil}\left(\frac{h - h_{\text{start}}}{h_{\text{gap-loop}}} \cdot (\text{grid}_{\text{size}}(h) - 1) + 1\right)$$

$$\text{grid}_{h,\text{high}} = \text{ceil}\left(\frac{-3.358 \text{ km} - (-5) \text{ km}}{148 \text{ km}} \cdot (593 - 1) + 1\right) = \text{ceil}(7.568) = 8$$

$$\text{grid}_{h,\text{low}} = h_{\text{low}} = \text{floor}\left(\frac{h - h_{\text{start}}}{h_{\text{gap-loop}}} \cdot (\text{grid}_{\text{size}}(h) - 1) + 1\right) = \text{floor}(7.568) = 7$$

$$h_{\text{exact}} = \frac{h - h_{\text{start}}}{h_{\text{gap-loop}}} \cdot (\text{grid}_{\text{size}}(h) - 1) + 1 = 7.568$$

Comparison: altitude grid point 7 is -3.5 km and grid point 8 is -3.25 km.

### Longitude grid calculation

$$\text{grid}_{\theta,\text{high}} = \theta_{\text{high}} = \text{ceil}\left(\frac{\theta - \text{lon}_{\text{start}}}{\text{lon}_{\text{gap-loop}}} \cdot (\text{grid}_{\text{size}}(\theta) - 1) + 1\right)$$

$$\text{grid}_{\theta,\text{high}} = \theta_{\text{high}} = \text{ceil}\left(\frac{237.05^\circ - 200^\circ}{40^\circ} \cdot (21 - 1) + 1\right) = \text{ceil}(19.525) = 20$$

$$\text{grid}_{\theta,\text{low}} = \theta_{\text{low}} = \text{floor}\left(\frac{\theta - \text{lon}_{\text{start}}}{\text{lon}_{\text{gap-loop}}} \cdot (\text{grid}_{\text{size}}(\theta) - 1) + 1\right) = \text{floor}(19.525) = 19$$

$$\theta_{\text{exact}} = \frac{\theta - \text{lon}_{\text{start}}}{\text{lon}_{\text{gap-loop}}} \cdot (\text{grid}_{\text{size}}(\theta) - 1) + 1 = 19.525$$

Comparison: longitude grid point 19 is 236° and grid point 20 is 238°.

### Latitude grid calculation

$$\text{grid}_{\phi,\text{high}} = \phi_{\text{high}} = \text{ceil}\left(\frac{\phi - \text{lat}_{\text{start}}}{\text{lat}_{\text{gap-loop}}} \cdot (\text{grid}_{\text{size}}(\phi) - 1) + 1\right)$$

$$\text{grid}_{\phi,\text{high}} = \text{ceil}\left(\frac{67.29^\circ - 63^\circ}{14^\circ} \cdot (8 - 1) + 1\right) = \text{ceil}(3.145) = 4$$

$$\text{grid}_{\phi,\text{low}} = \phi_{\text{low}} = \text{floor}\left(\frac{\phi - \text{lat}_{\text{start}}}{\text{lat}_{\text{gap-loop}}} \cdot (\text{grid}_{\text{size}}(\phi) - 1) + 1\right) = \text{floor}(3.145) = 3$$

$$\phi_{\text{exact}} = \frac{\phi - \text{lat}_{\text{start}}}{\text{lat}_{\text{gap-loop}}} \cdot (\text{grid}_{\text{size}}(\phi) - 1) + 1 = 3.145$$

Comparison: latitude grid point 3 is 67° and grid point 4 is 69°.

As the grid points are known, the interpolation box can be filled and interpolated (see figure 12-1 & figure 12-2). The interpolation is a standard linear interpolation based on these equations (x known, y unknown):

$$\frac{y - y_1}{x - x_1} = \frac{y_2 - y_1}{x_2 - x_1}$$

$$y = y_1 + \frac{y_2 - y_1}{x_2 - x_1} \cdot (x - x_1)$$

### Temperature grid points

$$a = \text{grid}(\theta_{\text{low}}, \phi_{\text{low}}, h_{\text{low}}) = 230.5 \text{ K}$$

$$b = \text{grid}(\theta_{\text{high}}, \phi_{\text{low}}, h_{\text{low}}) = 230.6 \text{ K}$$

$$c = \text{grid}(\theta_{\text{low}}, \phi_{\text{low}}, h_{\text{high}}) = 229.8 \text{ K}$$

$$d = \text{grid}(\theta_{\text{high}}, \phi_{\text{low}}, h_{\text{high}}) = 230.0 \text{ K}$$

$$e = \text{grid}(\theta_{\text{low}}, \phi_{\text{high}}, h_{\text{low}}) = 223.9 \text{ K}$$

$$f = \text{grid}(\theta_{\text{high}}, \phi_{\text{high}}, h_{\text{low}}) = 224.1 \text{ K}$$

$$g = \text{grid}(\theta_{\text{low}}, \phi_{\text{high}}, h_{\text{high}}) = 223.7 \text{ K}$$

$$h = \text{grid}(\theta_{\text{high}}, \phi_{\text{high}}, h_{\text{high}}) = 223.8 \text{ K}$$

### First interpolation direction – lower altitude

$$\rho_{\text{I}} = a + \frac{b - a}{\theta_{\text{high}} - \theta_{\text{low}}} \cdot (\theta_{\text{exact}} - \theta_{\text{low}})$$

$$\rho_{\text{I}} = 230.5 \text{ K} + \frac{230.6 \text{ K} - 230.5 \text{ K}}{20 - 19} \cdot (19.525 - 19) = 230.553 \text{ K}$$

$$\rho_{\text{II}} = e + \frac{f - e}{\theta_{\text{high}} - \theta_{\text{low}}} \cdot (\theta_{\text{exact}} - \theta_{\text{low}})$$

$$\rho_{\text{II}} = 223.9 \text{ K} + \frac{224.1 \text{ K} - 223.9 \text{ K}}{20 - 19} \cdot (19.525 - 19) = 224.005 \text{ K}$$

### First interpolation direction – higher altitude

$$\rho_{\text{IV}} = c + \frac{d - c}{\theta_{\text{high}} - \theta_{\text{low}}} \cdot (\theta_{\text{exact}} - \theta_{\text{low}})$$

$$\rho_{\text{IV}} = 229.8 \text{ K} + \frac{230.0 \text{ K} - 229.8 \text{ K}}{20 - 19} \cdot (19.525 - 19) = 229.905 \text{ K}$$

$$\rho_{\text{V}} = g + \frac{h - g}{\theta_{\text{high}} - \theta_{\text{low}}} \cdot (\theta_{\text{exact}} - \theta_{\text{low}})$$

$$\rho_V = 223.7 \text{ K} + \frac{223.8 \text{ K} - 223.7 \text{ K}}{20 - 19} \cdot (19.525 - 19) = 223.753 \text{ K}$$

**Second interpolation direction**

$$\rho_{III} = \rho_I + \frac{\rho_{II} - \rho_I}{\phi_{\text{high}} - \phi_{\text{low}}} \cdot (\phi_{\text{exact}} - \phi_{\text{low}})$$

$$\rho_{III} = 230.553 \text{ K} + \frac{224.005 \text{ K} - 230.553 \text{ K}}{4 - 3} \cdot (3.145 - 3) = 229.604 \text{ K}$$

$$\rho_{VI} = \rho_{IV} + \frac{\rho_V - \rho_{IV}}{\phi_{\text{high}} - \phi_{\text{low}}} \cdot (\phi_{\text{exact}} - \phi_{\text{low}})$$

$$\rho_{VI} = 229.905 \text{ K} + \frac{223.753 \text{ K} - 229.905 \text{ K}}{4 - 3} \cdot (3.145 - 3) = 229.013 \text{ K}$$

**Third interpolation direction**

$$\rho_{VII} = \rho_{III} + \frac{\rho_{VI} - \rho_{III}}{h_{\text{high}} - h_{\text{low}}} \cdot (h_{\text{exact}} - h_{\text{low}})$$

$$\rho_{VII} = 229.604 \text{ K} + \frac{229.013 \text{ K} - 229.604 \text{ K}}{8 - 7} \cdot (7.569 - 7) = 229.268 \text{ K}$$

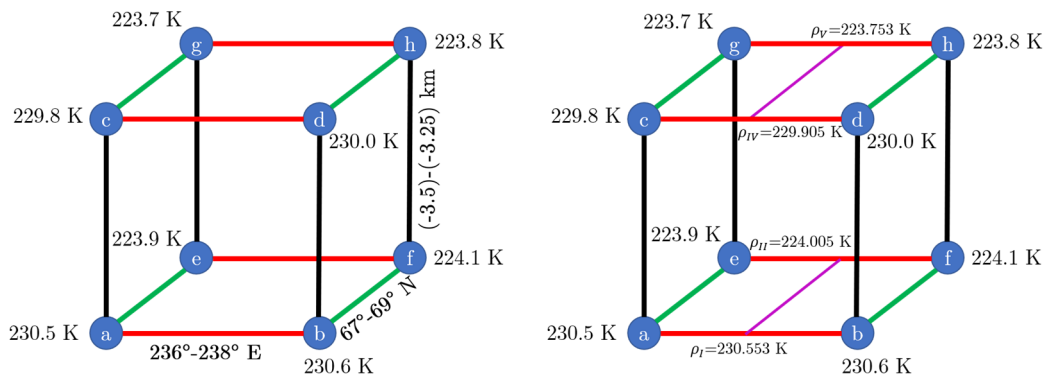


figure 12-1: Interpolation box example 1.

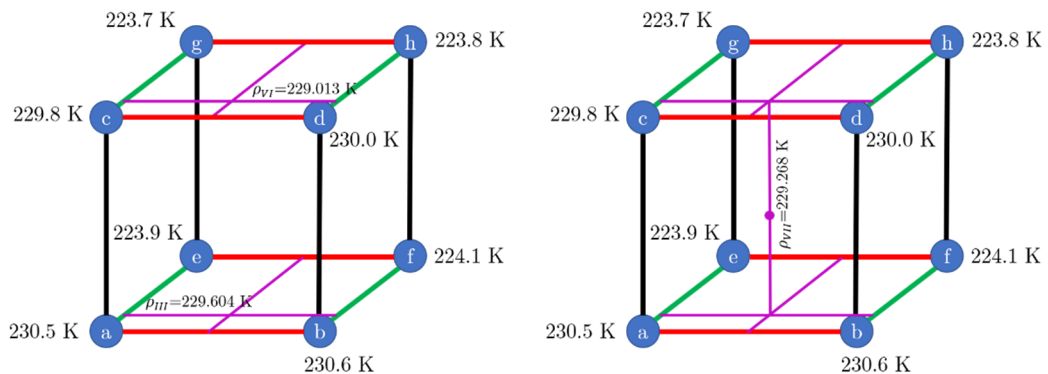


figure 12-2: Interpolation box example 2.

### 12.3 LCA Partial derivative matrix $F_x$

The following describes the full partial derivative matrix including vertical wind perturbations. The last four rows are all zeros because the derivatives of the static coefficients are zero.

If the vertical wind perturbations are not included, the last column and last row must be deleted.

$$F_x = \frac{\delta f}{\delta x} \Big|_x$$

$$= \begin{bmatrix} \frac{\partial \dot{r}}{\partial r} & \frac{\partial \dot{r}}{\partial \theta} & \frac{\partial \dot{r}}{\partial \phi} & \frac{\partial \dot{r}}{\partial v} & \frac{\partial \dot{r}}{\partial \gamma} & \frac{\partial \dot{r}}{\partial \psi} & \frac{\partial \dot{r}}{\partial \rho_{SD}} & \frac{\partial \dot{r}}{\partial v_{w,east,SD}} & \frac{\partial \dot{r}}{\partial v_{w,north,SD}} & \frac{\partial \dot{r}}{\partial v_{w,vert,SD}} \\ \frac{\partial \dot{\theta}}{\partial r} & \frac{\partial \dot{\theta}}{\partial \theta} & \frac{\partial \dot{\theta}}{\partial \phi} & \frac{\partial \dot{\theta}}{\partial v} & \frac{\partial \dot{\theta}}{\partial \gamma} & \frac{\partial \dot{\theta}}{\partial \psi} & \frac{\partial \dot{\theta}}{\partial \rho_{SD}} & \frac{\partial \dot{\theta}}{\partial v_{w,east,SD}} & \frac{\partial \dot{\theta}}{\partial v_{w,north,SD}} & \frac{\partial \dot{\theta}}{\partial v_{w,vert,SD}} \\ \frac{\partial \dot{\phi}}{\partial r} & \frac{\partial \dot{\phi}}{\partial \theta} & \frac{\partial \dot{\phi}}{\partial \phi} & \frac{\partial \dot{\phi}}{\partial v} & \frac{\partial \dot{\phi}}{\partial \gamma} & \frac{\partial \dot{\phi}}{\partial \psi} & \frac{\partial \dot{\phi}}{\partial \rho_{SD}} & \frac{\partial \dot{\phi}}{\partial v_{w,east,SD}} & \frac{\partial \dot{\phi}}{\partial v_{w,north,SD}} & \frac{\partial \dot{\phi}}{\partial v_{w,vert,SD}} \\ \frac{\partial \dot{v}}{\partial r} & \frac{\partial \dot{v}}{\partial \theta} & \frac{\partial \dot{v}}{\partial \phi} & \frac{\partial \dot{v}}{\partial v} & \frac{\partial \dot{v}}{\partial \gamma} & \frac{\partial \dot{v}}{\partial \psi} & \frac{\partial \dot{v}}{\partial \rho_{SD}} & \frac{\partial \dot{v}}{\partial v_{w,east,SD}} & \frac{\partial \dot{v}}{\partial v_{w,north,SD}} & \frac{\partial \dot{v}}{\partial v_{w,vert,SD}} \\ \frac{\partial \dot{\gamma}}{\partial r} & \frac{\partial \dot{\gamma}}{\partial \theta} & \frac{\partial \dot{\gamma}}{\partial \phi} & \frac{\partial \dot{\gamma}}{\partial v} & \frac{\partial \dot{\gamma}}{\partial \gamma} & \frac{\partial \dot{\gamma}}{\partial \psi} & \frac{\partial \dot{\gamma}}{\partial \rho_{SD}} & \frac{\partial \dot{\gamma}}{\partial v_{w,east,SD}} & \frac{\partial \dot{\gamma}}{\partial v_{w,north,SD}} & \frac{\partial \dot{\gamma}}{\partial v_{w,vert,SD}} \\ \frac{\partial \dot{\psi}}{\partial r} & \frac{\partial \dot{\psi}}{\partial \theta} & \frac{\partial \dot{\psi}}{\partial \phi} & \frac{\partial \dot{\psi}}{\partial v} & \frac{\partial \dot{\psi}}{\partial \gamma} & \frac{\partial \dot{\psi}}{\partial \psi} & \frac{\partial \dot{\psi}}{\partial \rho_{SD}} & \frac{\partial \dot{\psi}}{\partial v_{w,east,SD}} & \frac{\partial \dot{\psi}}{\partial v_{w,north,SD}} & \frac{\partial \dot{\psi}}{\partial v_{w,vert,SD}} \\ \frac{\partial C_p}{\partial r} = 0 & 0 & 0 & 0 & 0 & 0 & 0 & 0 & 0 & 0 \\ 0 & 0 & 0 & 0 & 0 & 0 & 0 & 0 & 0 & 0 \\ 0 & 0 & 0 & 0 & 0 & 0 & 0 & 0 & 0 & 0 \\ 0 & 0 & 0 & 0 & 0 & 0 & 0 & 0 & 0 & 0 \end{bmatrix}$$

With:

$$\frac{\partial \dot{r}}{\partial r} = \frac{\partial \dot{r}}{\partial \theta} = \frac{\partial \dot{r}}{\partial \phi} = \frac{\partial \dot{r}}{\partial v} = \frac{\partial \dot{r}}{\partial \gamma} = \frac{\partial \dot{r}}{\partial \psi} = \frac{\partial \dot{r}}{\partial \rho_{SD}} = \frac{\partial \dot{r}}{\partial v_{w,east,SD}} = \frac{\partial \dot{r}}{\partial v_{w,north,SD}} = 0$$

$$\frac{\partial \dot{r}}{\partial v} = \sin(\gamma)$$

$$\frac{\partial \dot{r}}{\partial \gamma} = v \cdot \cos(\gamma)$$

$$\frac{\partial \dot{r}}{\partial v_{w,vert,SD}} = 1$$

$$\frac{\partial \dot{\theta}}{\partial r} = - \frac{v_{w,east,N} + v_{w,east,SD} + v \cdot \cos(\gamma) \cdot \sin(\psi)}{r^2 \cdot \cos(\phi)}$$

$$\frac{\partial \dot{\theta}}{\partial \theta} = \frac{\partial \dot{\theta}}{\partial \rho_{SD}} = \frac{\partial \dot{\theta}}{\partial v_{w,north,SD}} = \frac{\partial \dot{\theta}}{\partial v_{w,vert,SD}} = 0$$

$$\frac{\partial \dot{\theta}}{\partial \phi} = \frac{\sin(\phi) * (v_{w,east,N} + v_{w,east,SD} + v * \cos(\gamma) * \sin(\psi))}{r * \cos(\phi)^2}$$

$$\frac{\partial \dot{\theta}}{\partial v} = \frac{\cos(\gamma) * \sin(\psi)}{r * \cos(\phi)}$$

$$\frac{\partial \dot{\theta}}{\partial \gamma} = -\frac{v * \sin(\gamma) * \sin(\psi)}{r * \cos(\phi)}$$

$$\frac{\partial \dot{\theta}}{\partial \psi} = \frac{v * \cos(\gamma) * \cos(\psi)}{r * \cos(\phi)}$$

$$\frac{\partial \dot{\theta}}{\partial v_{w,east,SD}} = \frac{1}{r * \cos(\phi)}$$

$$\frac{\partial \dot{\phi}}{\partial r} = -\frac{v_{w,north,N} + v_{w,north,SD} + v * \cos(\gamma) * \cos(\psi)}{r^2}$$

$$\frac{\partial \dot{\phi}}{\partial \theta} = \frac{\partial \dot{\phi}}{\partial \phi} = \frac{\partial \dot{\phi}}{\partial \rho_{SD}} = \frac{\partial \dot{\phi}}{\partial v_{w,east,SD}} = \frac{\partial \dot{\phi}}{\partial v_{w,vert,SD}} = 0$$

$$\frac{\partial \dot{\phi}}{\partial v} = \frac{\cos(\gamma) * \cos(\psi)}{r}$$

$$\frac{\partial \dot{\phi}}{\partial \gamma} = -\frac{v * \cos(\psi) * \sin(\gamma)}{r}$$

$$\frac{\partial \dot{\phi}}{\partial \psi} = -\frac{v * \cos(\gamma) * \sin(\psi)}{r}$$

$$\frac{\partial \dot{\phi}}{\partial v_{w,north,SD}} = \frac{1}{r}$$

$$\frac{\partial \dot{v}}{\partial r} = \frac{\partial \dot{v}}{\partial \theta} = \frac{\partial \dot{v}}{\partial \phi} = \frac{\partial \dot{v}}{\partial \psi} = \frac{\partial \dot{v}}{\partial v_{w,east,SD}} = \frac{\partial \dot{v}}{\partial v_{w,north,SD}} = \frac{\partial \dot{v}}{\partial v_{w,vert,SD}} = 0$$

$$\frac{\partial \dot{v}}{\partial v} = -\frac{v * (A_P * C_{D_P} + A_{SC} * C_{D_{SC}}) * (\rho_{N} + \rho_{SD})}{m}$$

$$\frac{\partial \dot{v}}{\partial \gamma} = -g * \cos(\gamma)$$

$$\frac{\partial \dot{v}}{\partial \rho_{SD}} = -\frac{v^2 * (A_P * C_{D_P} + A_{SC} * C_{D_{SC}})}{2 * m}$$

$$\frac{\partial \dot{\gamma}}{\partial r} = -\frac{v * \cos(\gamma)}{r^2}$$

$$\frac{\partial \dot{\gamma}}{\partial \theta} = \frac{\partial \dot{\gamma}}{\partial \phi} = \frac{\partial \dot{\gamma}}{\partial \psi} = \frac{\partial \dot{\gamma}}{\partial v_{w,east,SD}} = \frac{\partial \dot{\gamma}}{\partial v_{w,north,SD}} = \frac{\partial \dot{\gamma}}{\partial v_{w,vert,SD}} = 0$$

$$\frac{\partial \dot{\gamma}}{\partial v} = \cos(\gamma) * \left( \frac{g}{v^2} + \frac{1}{r} \right) - \frac{T * \sin(\beta)}{m * v^2} + \frac{A_{SC} * C_L * \cos(\sigma) * (\rho_{oN} + \rho_{oSD})}{2 * m}$$

$$\frac{\partial \dot{\gamma}}{\partial \gamma} = \sin(\gamma) * \left( \frac{g}{v} - \frac{v}{r} \right)$$

$$\frac{\partial \dot{\gamma}}{\partial \rho_{SD}} = \frac{A_{SC} * C_L * v * \cos(\sigma)}{2 * m}$$

$$\frac{\partial \dot{\psi}}{\partial r} = - \frac{v * \cos(\gamma) * \sin(\psi) * \tan(\phi)}{r^2}$$

$$\frac{\partial \dot{\psi}}{\partial \theta} = \frac{\partial \dot{\psi}}{\partial v_{w,east,SD}} = \frac{\partial \dot{\psi}}{\partial v_{w,north,SD}} = \frac{\partial \dot{\psi}}{\partial v_{w,vert,SD}} = 0$$

$$\frac{\partial \dot{\psi}}{\partial \phi} = \frac{v * \cos(\gamma) * \sin(\psi) * (\tan(\phi)^2 + 1)}{r}$$

$$\frac{\partial \dot{\psi}}{\partial v} = \frac{\cos(\gamma) * \sin(\psi) * \tan(\phi)}{r} + \frac{A_{SC} * C_L * \sin(\sigma) * (\rho_{oN} + \rho_{oSD})}{2 * m * \cos(\gamma)}$$

$$\frac{\partial \dot{\psi}}{\partial \gamma} = \frac{A_{SC} * C_L * v * \sin(\gamma) * \sin(\sigma) * (\rho_{oN} + \rho_{oSD})}{2 * m * \cos(\gamma)^2} - \frac{v * \sin(\gamma) * \sin(\psi) * \tan(\phi)}{r}$$

$$\frac{\partial \dot{\psi}}{\partial \psi} = \frac{v * \cos(\gamma) * \cos(\psi) * \tan(\phi)}{r}$$

$$\frac{\partial \dot{\psi}}{\partial \rho_{SD}} = \frac{A_{SC} * C_L * v * \sin(\sigma)}{2 * m * \cos(\gamma)}$$